HAL
open science

Optimization and Improvement of a Novel HVOF Process Fueled with Ethanol

Shaowu Liu

To cite this version:

Shaowu Liu. Optimization and Improvement of a Novel HVOF Process Fueled with Ethanol. Materials. Université Bourgogne Franche-Comté, 2022. English. NNT : 2022UBFCA003 . tel-03703992

HAL Id: tel-03703992

https://theses.hal.science/tel-03703992v1

Submitted on 24 Jun 2022

HAL is a multi-disciplinary open access archive for the deposit and dissemination of scientific research documents, whether they are published or not. The documents may come from teaching and research institutions in France or abroad, or from public or private research centers.

L'archive ouverte pluridisciplinaire **HAL**, est destinée au dépôt et à la diffusion de documents scientifiques de niveau recherche, publiés ou non, émanant des établissements d'enseignement et de recherche français ou étrangers, des laboratoires publics ou privés.

SPIM

Thèse de Doctorat

utbm université de technologie Belfort-Montbéliard

école doctorale sciences pour l'ingénieur et microtechniques

UNIVERSITÉ DE TECHNOLOGIE BELFORT-MONTBÉLIARD

Optimization and Improvement of a Novel HVOF Process Fueled with Ethanol

Shaowu LIU

THESE DE DOCTORAT DE L'ETABLISSEMENT UNIVERSITE BOURGOGNE FRANCHE-COMTE

PREPAREE A L'UNIVERSITE DE TECHNOLOGIE DE BELFORT MONTBELIARD

Ecole doctorale n°

Sciences physiques pour l'ingénieur et microtechniques - SPIM

Doctorat de Sciences pour lIngénieur

Par

Mr. Shaowu LIU

Optimization and Improvement of a Novel HVOF Process Fueled with Ethanol

Thèse présentée et soutenue à UTBM Site de Sévenans, le 22 March 2022

Composition du Jury:

Mr. Andreas KILLINGER	Professeur, Université de Stuttgart	Rapporteur
Mr. Philippe BERTRAND	Professeur, École Nationale d'Ingénieurs de Saint-Étienne	Rapporteur
Mr. Thierry GROSDIDIER	Professeur, Université de Lorraine	Examinateur
Mr. Daniel RIVOLET	Ingénieur, Flame Spray Technologies B.V.	Examinateur
Mr. Hanlin LIAO	Professeur, University of Technology of Belfort-Montbeliard	Directeur de thèse
Mr. Michel MOLIERE	Ingénieur (HDR), University of Technology of Belfort-Montbeliard	Codirecteur de thèse
Mr. Shuo YIN	Assistant Professor, Trinity College Dublin	Invité

General introduction

After decades of development and use, the thermal spray processes have become much diversified. Among them, the high velocity oxy-fuel (HVOF) spray has become one of the most advanced processes for producing high performance cermet or alloy coatings due to its moderate particle temperature, and high particle velocity. Common HVOF thermal spray systems classically use the combustion of gases, such as hydrogen, propane or a liquid fuel such as kerosene. However, there is currently a limited amount of literature on the use of ethanol as a fuel for HVOF process to prepare coatings and investigate their performances. Ethanol benefits from environmentally friendly features, being less polluting (less emission of soot particles) than conventional fossil liquid fuels (i.e. kerosene). In addition, it is critical to avoid or significantly reduce the harmful oxidation and decarburization processes that degrade many metallic or ceramic coatings (primarily containing carbides). Even though the HVOF process results in relatively low particle oxidation, one would like always to decrease the flame temperature and increase the velocity to obtain coatings of higher quality. Therefore, the work of this thesis aims to investigate such an ethanol-fueled HVOF device (called "eGun HVOF"), with the objective to define the merits and limitations of that technology. In view of the limited literature available, it appeared to be of great interest to study the optimization of the spraying parameters of that new spraying process, as well as thoroughly evaluate the performances of the corresponding coatings. In addition, we endeavored to improve the eGun HVOF equipment to create a HVOAF device, which improves coating quality by injecting compressed air into the combustion chamber to increase particle velocity. The details are as follows.

Chapter 1 offers an overview of the evolution of the HVOF technology starting from its creation to the latest status. This review will allow to better introduce the ethanol-fueled HVOF device and highlight its specificities as well as its potential interest and advantages, compared to the existing ones.

Chapter 2 introduces the experimental setups of HVOF and HVOAF as used in this thesis,

the tested materials (powder and substrate), the characterisation methods of the coating and the test methods of the coating properties.

Chapter 3 investigates the effect of different oxygen/fuel ratios on the evolution of the velocity and temperature of in-flight particles in correlation with the properties of the resulting WC-CoCr coatings prepared by eGun HVOF process. A detailed relationship between particle parameters and coating properties is elaborated to infer the optimal parameters for the process.

Chapter 4 investigates Cr_3C_2–25NiCr coatings deposited by eGun HVOF process. The Taguchi method was employed to adjust the spray parameters to achieve better erosion resistance at 90° impact angle. Moreover, investigations are also performed to determine the influence of different stoichiometry conditions, defined as the oxygen/ethanol ratio, on the evolution of the coating microstructure and in relation with the properties of the resulting Cr_3C_2–25NiCr coatings. Microhardness, porosity, fracture toughness, erosion resistance and sliding wear resistance of the Cr_3C_2–25NiCr coatings are compared.

Chapter 5 introduces the creation of HVOAF device based on the original eGun HVOF device. NiCoCrAlYTa coatings are prepared using the HVOAF device. Investigations are conducted to determine the influence of different compressed air flow rates on the evolution of the microstructure and properties of the resulting NiCoCrAlYTa coatings. Microhardness, porosity, bonding strength, sliding wear resistance and corrosive resistance of the NiCoCrAlYTa coatings are investigated.

In summary, this thesis is devoted to the research on the performances of ethanol-fueled HVOF process, as well as the development and performance study of the HVOAF device. This work is hoped to provide theoretical and technical foundations for the further development of this technology.

Content

General introduction I

Chapter 1 Introduction 1

1.1 High velocity oxy-fuel spraying (HVOF) 2

1.1.1 Deposition mechanism and characteristics of HVOF process 2

1.1.2 Evolution of HVOF processes 4

1.1.3 Typical coatings sprayed with HVOF process 8

1.1.4 Main applications of HVOF process 11

1.2 HVAF process and modified HVOF process 12

1.2.1 Description of the HVAF process 12

1.2.2 HVOF process modified with a gas shroud 13

1.2.3 HVOF process modified with an intermediate mixing chamber 15

1.3 The eGun HVOF device fueled with ethanol 17

1.3.1 Structure and working principle of the eGun HVOF torch 17

1.3.2 Advantages of choosing ethanol as a liquid fuel 18

1.3.3 Significance of research on the eGun HVOF process 19

1.4 Objectives of this thesis 19

Reference 20

Chapter 2 Experimental Materials and Methods 27

2.1 Spraying equipment 28

2.2 Materials 30

2.2.1 Powders 30

2.2.2 Substrates 33

2.3 Coatings preparation 33

2.4 Characterization methods 34

2.4.1 Microstructure of the powders and coatings 34

2.4.2 Online diagnosis of in-flight particles 34

2.4.3 Porosity and surface roughness of the coatings 35
2.4.4 Phase composition of the powders and the coatings 35
2.4.5 Mechanical properties of the coatings 35
2.4.6 Erosion wear tests 36
2.4.7 Sliding wear tests 38
2.4.8 Electrochemical measurements 38
References 40
Chapter 3 Relationships between in-flight particle characteristics and properties of the WC-10Co-4Cr coatings prepared with the Ethanol-Fueled e-Gun HVOF device 41
3.1 Introduction 42
3.2 Preparation conditions of the coatings 43
3.3 Characteristics of in-flight particles 44
3.4 Phase composition and microstructure of coatings 47
3.5 Evaluation of the porosity and microhardness 50
3.6 Fracture toughness of the coatings 53
3.7 Conclusions 55
References 57
Chapter 4 Optimization of the erosion and sliding wear resistance of Cr_3C_2-NiCr Coatings via the novel HVOF device 59
4.1 Introduction 60
4.2 Optimization and Erosion Behavior of Cr_3C_2-NiCr Coatings 61
4.2.1 Testing methodology and primary results 61
4.2.2 Analysis of the signal-to-noise (S/N) ratio 62
4.2.3 Analysis of variance (ANOVA) 65
4.2.4 Characterization of the “optimized” coatings 66
4.2.5 Erosion mechanism of the optimized coatings 70
4.3 Effect of oxygen/fuel ratio on the erosion and sliding wear behavior of Cr_3C_2-NiCr Coatings 74

4.3.1 Preparation conditions of Cr_3C_2-NiCr Coatings with different oxygen/fuel ratio 74
4.3.2 Phase composition and microstructure of the coatings 76
4.3.3 Porosity and microhardness 78
4.3.4 Fracture toughness 81
4.3.5 Erosion tests 83
4.3.6 Coefficient of friction and wear rate 87
4.3.7 Wear mechanism of the coatings 89
4.4 Conclusions 93
References 95
Chapter 5 Evolution of the torch: Switching from HVOF to HVOAF 99
5.1 Introduction 100
5.2 Calculation of the combustion temperature of ethanol in the combustion chamber 101
5.3 Design of torch to Convert HVOF to HVOAF 104
5.4 Effect of adding compressed air into the torches on the microstructure and properties of HVOAF-sprayed NiCoCrAlYTa coatings 105
5.4.1 Preparation conditions of NiCoCrAlYTa coatings 105
5.4.2 Optimization of the standoff distance and compressed air flow rate 106
5.4.3 Phase composition and microstructure of the NiCoCrAlYTa coatings 108
5.4.4 Microstructures 109
5.4.5 Roughness and porosity 115
5.4.6 Bonding strength 116
5.4.7 Microhardness and nano-microhardness 117
5.4.8 Sliding wear tests of NiCoCrAlYTa coatings 118
5.4.9 Electrochemical testing 123
5.5 Conclusions 124
References 126
Chapter 6 Conclusions and Perspectives 129

6.1 Conclusions 130
6.2 Perspectives 132
Abstract 135
Résumé 137

List of figures

Fig. 1.1 Schematic cross-section of HVOF gun [5] 3

Fig. 1.2 Typical design evolutions of HVOF. (a) Principle of the Jet Kote. (b) Axial injection and combustion chamber. (c) Axial chamber with radial powder injection [17] 5

Fig. 1.3 Particle temperatures and velocities obtained in different thermal spray processes, as measured for high-density materials. The arrow indicates the trend of recent developments (AS: Powder flame spraying, FS Wire flame spraying, PS Air plasma spraying, VPS Vacuum plasma spraying, CS Cold Spray) [19]. 6

Fig. 1.4 Schematic of the DJ2700 torch [20] 7

Fig. 1.5 Schematic of the JP5000 torch [21] 7

Fig. 1.6 (a) Cross section of detonation-sprayed TBC using hollow sphere YSZ powder with the HVOF bond coat. (b) Microstructure of the HVOF NiCrAlY coating in the as-sprayed state [28] 9

Fig. 1.7 SEM photographs of WC−10Co−4Cr and Cr_3C_2−25NiCr coated on H13 steel: (a) WC−10Co−4Cr (plan view); (b) WC−10Co−4Cr (cross-section); (c) Cr_3C_2−25NiCr (plan view); (d) Cr_3C_2−25NiCr (cross-section) [41] 10

Fig. 1.8 Microstructure of a pure polyimide coating (B) that was HVOF-sprayed onto a carbon-fiber reinforced PMC substrate (A) [50] 11

Fig. 1.9 Schematic of a commercial AC-HVAF gun [56] 13

Fig. 1.10 Schematic of (a) commercial high-pressure HVOF (JP5000) device, (b) same device modified with a gas shroud, (c) same device modified with an intermediate mixing chamber [65] 14

Fig. 1.11 Velocity and temperature of in-flight particles under each condition [66] 15

Fig. 1.12 Oxygen content in titanium coatings spayed by the modified HVOF spraying with the mixing chamber [65] 16

Fig. 1.13 Porosity of Ti coatings fabricated by the modified HVOF process as function of spray

distance [72] 17
Fig. 1.14 Cross sections of Ti coatings fabricated by the modified HVOF process with the mixing chamber at three nitrogen flow rates [72] 17
Fig. 1.15 Schematic of eGun HVOF torch [73] 18
Fig. 2.1 Schematic geometry of the eGun HVOF torch 29
Fig. 2.2 Photograph of the eGun HVOF torch 29
Fig. 2.3 Photograph of the novel eGun HVOAF torch 30
Fig. 2.4 WC-10Co4Cr feedstock particles used in this work: (a) and (b) overview and magnified SEM images; (c) cross section showing its microstructures; (d) particle size distribution 31
Fig. 2.5 Cr_3C_2–NiCr feedstock powder: (a) SEM image of the overview, (b) BSE image of the cross section of the powder, (c) particle size distribution 32
Fig. 2.6 NiCoCrAlYTa powders used in this work: (a) overview and magnified SEM images; (b) EDS analysis of the surface; (c) particle size distribution; (d) XRD patterns 33
Fig. 2.7 Schematic of the air jet erosion tester 37
Fig. 2.8 Morphology of the alumina erodent 37
Fig. 3.1 Evolution of particle temperatures and velocities for ethanol-oxygen mixtures 45
Fig. 3.2 Evolution of particle temperatures and velocities: (a) vs. different O_2 flow rates; (b) vs. different C_2H_6O flow rates. 47
Fig. 3.3 XRD patterns of the WC–10Co–4Cr feedstock powder and the coatings with different spraying parameters. 48
Fig. 3.4 Cross-sectional SEM micrographs of coated samples: (a) overview image; (b) magnification image 49
Fig. 3.5 Higher magnification BSE image showing the details of the microstructure of the coating: (a) BSE image; (b) EDS analysis results of point 1 and 2 in the coating. 50
Fig. 3.6 Evolution of the porosity of coatings: (a) vs. different O_2 flow rates; (b) vs. different C_2H_6O flow rates 51
Fig. 3.7 Evolution of the porosity of coatings: (a) vs. particle temperature; (b) vs. particle

velocity.....51
Fig. 3.8 Evolution of the microhardness of coatings: (a) vs. different O_2 flow rates; (b) vs. different C_2H_6O flow rates.....52
Fig. 3.9 Evolution of the microhardness of coatings: (a) vs. particle temperature; (b) vs. particle velocity.....52
Fig. 3.10 Typical indent micrographs on the cross-sections of the coating layers sprayed with different parameters. (a) E1: Ethanol:22l/h-O_2:430l/min; (b) E2: Ethanol:22l/h-O_2:460l/min; (c) E3: Ethanol:22l/h-O_2:490l/min; (d) E4: Ethanol:22l/h-O_2:520l/min; (e) E5: Ethanol:24l/h-O_2:520l/min; (f) E6: Ethanol:26l/h-O_2:520l/min; (g) E7: Ethanol:28l/h-O_2:520l/min.....54
Fig. 3.11 Evolution of the fracture toughness with the porosity of the coatings: (a) vs. different O_2 flow rates; (b) vs. different C_2H_6O flow rates. 55
Fig. 4.1 The mean S/N ratio for erosion wear loss. 65
Fig. 4.2 XRD patterns of the Cr_3C_2–NiCr feedstock powder and of the sprayed coating.....67
Fig. 4.3 Cross-sectional SEM micrographs of coated samples: (a) overview image; (b) higher magnification image.....68
Fig. 4.4 Element mappings of a cross-section of as-sprayed Cr_3C_2-NiCr coating. 68
Fig. 4.5 EDS results of points 1, 2 and 3 in Fig. 8.....69
Fig. 4.6 Erosion wear rate of Cr_3C_2-NiCr coatings at different impact angles.....71
Fig. 4.7 SEM micrographs showing the morphology of the eroded surfaces of Cr_3C_2–NiCr coatings at different impact angles. (a) and (b): 30◦ impact angle; (c) and (d): 60◦ impact angle; (e) and (f): 90◦ impact angle. 73
Fig. 4.8 SEM micrographs of the cross-section of the eroded region of Cr_3C_2–NiCr coatings at different impact angles. (a): 30◦ impact angle; (b): 60◦ impact angle; (c) and (d): 90◦ impact angle.....74
Fig. 4.9 XRD patterns of the Cr_3C_2–NiCr feedstock powder and the obtained coatings. 77
Fig. 4.10 Cross-sectional SEM micrographs and BSE images of coated samples: (a) and (b): coating E1; (c) and (d): coating E5.....78
Fig. 4.11 Evolution of the porosity of Cr_3C_2-NiCr coatings: (a) vs. different O_2 flow rates; (b)

vs. different C_2H_6O flow rates. 80

Fig. 4.12 Evolution of the microhardness of Cr_3C_2-NiCr coatings: (a) vs. different O_2 flow rates; (b) vs. different C_2H_6O flow rates..... 81

Fig. 4.13 Evolution of the fracture toughness of coatings: (a) vs. different O_2 flow rates; (b) vs. different C_2H_6O flow rates. 82

Fig. 4.14 Cross-sectional morphologies and enlarged views of the eroded region of Cr_3C_2–NiCr coatings. (a) and (b): coating E1; (c) and (d): coating E5..... 83

Fig. 4.15. Erosion results in terms of coating mass loss as a function of cumulative mass of erodent..... 84

Fig. 4.16. Evolution of the erosion wear rates of the as-sprayed Cr3C2–NiCr coatings: (a) vs. porosity; (a) vs. microhardness; (b) vs. fracture toughness. 84

Fig. 4.17. General morphologies and enlarged views of the eroded surfaces of the Cr_3C_2–NiCr coatings. (a) and (b): coating E1; (c) and (d): coating E5..... 85

Fig. 4.18. Cross-sectional morphologies and enlarged views of the eroded region of Cr_3C_2–NiCr coatings. (a) and (b): coating E1; (c) and (d): coating E5..... 86

Fig. 4.19. Evolution of the friction coefficient of E1 and E5 coatings. 88

Fig. 4.20. The wear rates and coefficients of friction of the as-sprayed Cr_3C_2–NiCr coatings88

Fig. 4.21. Evolution of the wear rates of the as-sprayed Cr_3C_2–NiCr coatings: (a) vs. microhardness; (b) vs. fracture toughness. 89

Fig. 4.22. SEM micrographs of the wear scar surfaces of Cr_3C_2−NiCr coatings. (a), (b) and (c): coating E1; (d), (e) and (f): coating E5. 91

Fig. 4.23. SEM micrographs of the cross sections of the wear scars of Cr_3C_2−NiCr coatings. (a) and (b): coating E1; (c) and (d): coating E5. The red arrows represent the carbides cracking. The yellow arrows indicate that the cracks propagate along the matrix/carbide interface. 92

Fig. 4.24. SEM micrographs and element mappings of the wear scars produced on the alumina counter-bodies against Cr_3C_2−NiCr coatings. (a) and (b): vs coating E1; (c) and (d): vs coating E5. 93

Fig. 5.1 The effect of adding air and water on temperature..... 103

Fig. 5.2 The design schematic of the torch 105
Fig. 5.3 The schematic of the modified eGun HVOAF torch 105
Fig. 5.4 Porosity of coatings vs standoff distance and air flow rate 107
Fig. 5.5 Microhardness of the coatings vs standoff distance and air flow rate 108
Fig. 5.6 XRD patterns of the as-sprayed NiCoCrAlYTa coatings 109
Fig. 5.7 SEM images of the top surface of the as-sprayed NiCoCrAlYTa coatings. (a) and (b): coating-no air; (c) and (d): coating-air 200; (e) and (f): coating-air 400; (g) and (h): coating-air 600 111
Fig. 5.8 SEM images of cross-section of the as-sprayed NiCoCrAlYTa coatings. (a) and (b): coating-no air; (c) and (d): coating-air 200; (e) and (f): coating-air 400; (g) and (h): coating-air 600 113
Fig. 5.9 SEM micrographs (a), and element mappings (b) of cross-section of the coating-no air; and EDS results of point 1 (c), point 2 (d), and point 3 (e) in the areas of Fig. 5.9 (a). 115
Fig. 5.10 SEM micrographs (a), and element mappings (b) of cross-section of the coating-air 400; and EDS results of point 1 (c), point 2 (d), and point 3 (e) in the areas of Fig. 2.10 (a). 115
Fig. 5.11 The roughness (a) and porosity (b) of as-sprayed NiCoCrAlYTa coatings 116
Fig. 5.12 The bonding strength of the four as-sprayed NiCoCrAlYTa coatings 117
Fig. 5.13 The microhardness (a) and porosity (b) of the as-sprayed NiCoCrAlYTa coatings 118
Fig. 5.14 Friction coefficient-distance curves of the as-sprayed NiCoCrAlYTa coatings 119
Fig. 5.15 The wear rates and average coefficients of friction of the as-sprayed NiCoCrAlYTa coatings 120
Fig. 5.16 The SEM images and 2D topographies of wear traces of (a-1), (a-2), and (a-3): coating-no air; (b-1), (b-2), and (b-3): coating-air 200; (c-1), (c-2), and (c-3): coating-air 400; (d-1), (d-2), and (d-3): coating-air 600 121
Fig. 5.17 SEM morphologies of some worn surfaces of the Al_2O_3 balls corresponding to (a) coating-no air; (b) coating-air 200; (c) coating-air 400; (d) coating-air 600 123

Fig. 5.18 Tafel curves of NiCoCrAlYTa coating in 0.1 M HCl solution.....124

List of tables

Table 1.1 Comparison of NiCrBSi coating properties obtained with the different spraying.....4

Table 1.2 Spraying conditions [66].....15

Table 1.3 Typical operating conditions [72].....16

Table 3.1 The experimental spray parameters and corresponding properties of the WC-10Co4Cr coatings.....44

Table 4.1 Spray parameters and levels used in this experiment. 61

Table 4.2 Experimental results for erosion wear and corresponding S/N ratio. 61

Table 4.3 Erosion test conditions of the Cr_3C_2–NiCr coatings. 62

Table 4.4 S/N response for erosion wear 63

Table 4.5 Result of ANOVA analysis for S/N ratios of erosion wear loss. 66

Table 4.6 Compared performances of the Cr_3C_2-25wt.%NiCr coatings prepared via different HVOF processes. 70

Table 4.7 The spraying conditions of HVOF. 75

Table 4.8 The spraying parameters and corresponding properties of the Cr_3C_2–NiCr coatings. 75

Table 4.9 Erosion test conditions. 76

Table 4.10. EDX analysis of the points in Fig. 4.22 92

Table 5.1 The variation range of some coefficients in the equation 103

Table 5.2 Spraying parameters and corresponding properties of NiCoCrAlYTa coatings....106

Table 5.3 Elemental compositions of the top surface of the as-received powder and NiCoCrAlYTa coatings.....112

Table 5.4 EDS analysis of the points in Fig. 5.16.....122

Table 5.5 Results from Tafel polarization of NiCoCrAlYTa coating in 0.1 M HCl solution 124

Chapter 1 Introduction

1.1 High velocity oxy-fuel spraying (HVOF)

Since the creation of the high velocity oxy-fuel spray (HVOF) technology in 1958 and its first uses in the industry in the early 1980s, it has been continuously developed to improve the quality of the corresponding coatings. Therefore, the market share of this spraying technology has steadily increased [1].

1.1.1 Deposition mechanism and characteristics of HVOF process

HVOF thermal spraying is a technique in which powder material is melted and propelled at high velocity towards a target surface, using oxygen and fuel gas mixtures. A number of combustible molecules, including propylene, propane, hydrogen, acetylene, methane, ethylene, crylene, kerosene, MAPP (methyleacetylene-propadiene stabilised gas), LPG etc. are used as combustion fuels. A HVOF system consists of a spray gun, a powder feed unit, a flow meter unit, and an air and gas supply unit. A carrier gas feeds the desired powder from the powder feed unit to the gun, where combustion occurs. In the combustion zone, the powder material enters the flame, where it becomes molten or semi-molten, depending on its melting temperature, its feed rate and the temperature of the flame. The HVOF process can generate flame jets from moderate to high temperatures up to 3000ºC, but with extremely high velocities up to 2000 m/s, compared to about 100 m/s for conventional flame spraying and 1000 m/s for plasma spraying. As a result, a stream of spray particles with velocities of 300 m/s–800 m/s and typical temperatures in the range of 1700 °C–2200 °C is formed during the spraying process [2-4]. The molten or semi-molten particles are then propelled out of the gun nozzle at supersonic velocities towards the target/substrate, where the powder material gets deposited. Fig. 1.1 depicts the basic scheme of the HVOF spray system using the Diamond Jet gun as an example [5].

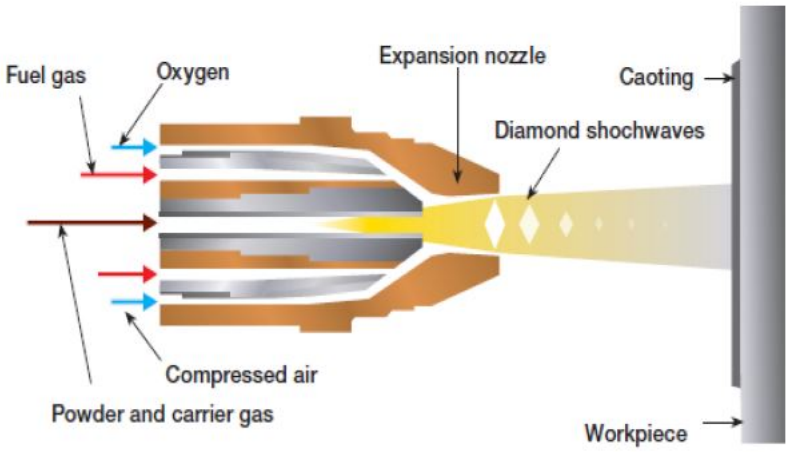

Fig. 1.1 Schematic cross-section of HVOF gun [5]

Due to the high impact velocity of the sprayed powder particles, the coatings produced by the HVOF spraying process are less porous and have higher bond strength and cohesive strength than those produced by other processes such as plasma spraying, flame spraying, and electric arc spraying [6-8]. Coating porosity, bond strength and oxide content are typical properties influenced by the coating procedure. Table 1.1 summarizes the typical characteristics of NiCrBSi coatings sprayed by different spraying techniques, indicating that the HVOF process has advantages in porosity, oxidation degree, hardness, adhesion and young modulus compared to flame or plasma spraying [9]. In the production of hard metal coatings, the HVOF process allows deposition of particles slightly below the melting temperature, thus reducing the oxidation and decomposition of materials such as WC and resulting in excellent wear resistance [10-12]. In addition, coating formation by the impact of high velocity, solid particles on the substrate also results in compressive residual stresses which increases the life time of coated components under dynamic load [13-15]. To summarize, the key advantages of HVOF sprayed coatings are:

- high density
- strong adhesion to substrates
- high cohesive strength
- strongly limited reactions and phase transformations, e.g. the oxidation or dissolution of WC in cobalt matrix materials

- high compressive residual stresses possible

Table 1.1 Comparison of NiCrBSi coating properties obtained with the different spraying Processes [9]

	Flame process	Plasma process	HVOF process
Porosity (%)	5.0±0.20	2.5±0.10	0.5±0.02
Oxides level (%)	3.0±0.09	2.0±0.06	0.2±0.06
Hardness ($HV_{0.3}$)	610±92	750±75	890±63
Adhesion (MPa)	33±3	45±5	65±6
Young modulus (GPa)	49±5	55±6	81±8

1.1.2 Evolution of HVOF processes

The HVOF technique was first established in 1958 by Union Carbide (now Praxair Surface Technology), but it was not truly commercialized until the early 1980s, when J.A. Browning introduced the Jet Kote (Deloro Stellite) system [16]. The principle of Jet Kote is shown in Fig. 1.2(a), which involves feeding a large amount of combustible gas into a water-cooled pressurized combustion chamber. The outlet of the chamber is perpendicular to the exit of the nozzle. The powder is injected into the throat region by a water-cooled injector on the axis of the gas stream [17]. The gas velocity is increased through the convergent–divergent nozzle (of the “de Laval” type). When a hot gas exits in the ambient air, as in all spray processes, the hot jet cools down quickly due to its expansion and the entrainment of the surrounding air. To prevent this phenomenon, it has been proposed to extend the nozzle by a water-cooled barrel (up to 30 cm long), where some energy of the jet is lost but much less than by mixing with the air. Of course, to avoid deposition on the barrel wall, particles should not be over-melted or remain below the melting temperature. Typical working pressures are in the range 0.3–0.6 MPa.

The axial flow device shown in Fig. 1.2(b) is the evolution of the initial water-cooled HVOF design. The powder is still injected axially into the chamber, coaxially with the nozzle. This design provides axial injection while improving thermal efficiency [18]. Axial injection of the powder, like the Jet Kote type gun, necessitates the use of a pressurized powder feeder.

Fig. 1.2(c) depicts the next evolution of HVOF design. The powder is injected radially beyond the throat at the beginning of the barrel or at the divergent region of the nozzle, but the

chamber remains coaxial with the nozzle. The pressure downstream of the throat is substantially lower than that in the combustion chamber upstream of the nozzle throat. Injecting powders at this point simplifies injection and particle entrainment and allows for multiple-port powder injection if necessary, resulting in a more uniform loading of the exit stream and more efficient use of the available heat. In general, the operating data shows that radial injection can at least double the spray rate per unit of energy as axial injection. Furthermore, this design has enabled the combustion gas pressure to be increased up to 0.8–0.9 MPa.

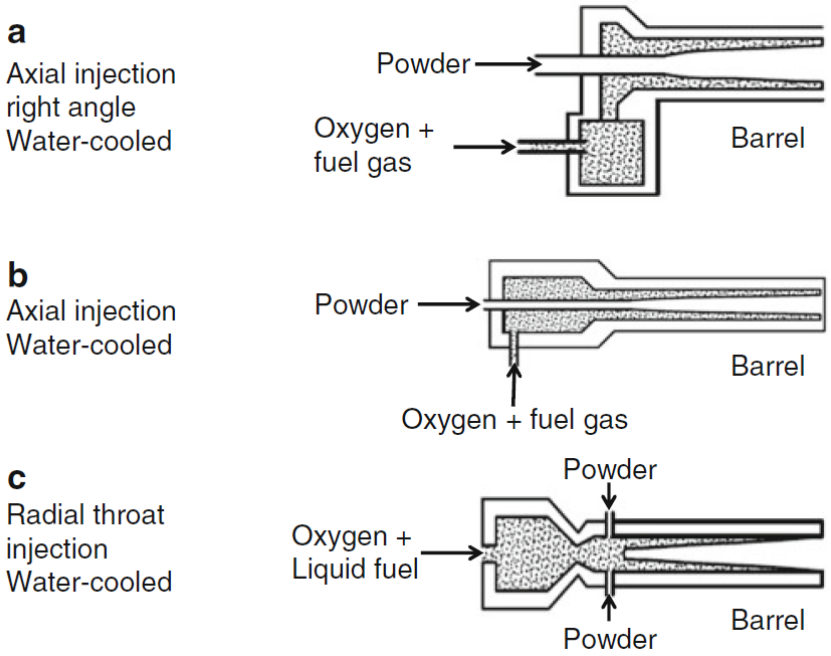

Fig. 1.2 Typical design evolutions of HVOF. (a) Principle of the Jet Kote. (b) Axial injection and combustion chamber. (c) Axial chamber with radial powder injection [17]

According to Gartner et al. [19], the development of HVOF systems over the last two decades has been aimed at lowering particle temperature and increasing particle velocity. Particle temperatures and velocities obtained in different thermal spray processes, as measured for high-density materials are shown in Fig. 1.3. Using converging–diverging de Laval-type nozzle designs and higher gas pressures, higher particle velocities were obtained. HVOF spray systems of the third generation (DJ2700, DJ2800, JP5000, JP8000, GTV K2 etc.) accelerate spray particles to velocities of about 650 m/s with chamber pressures of up to 1 MPa.

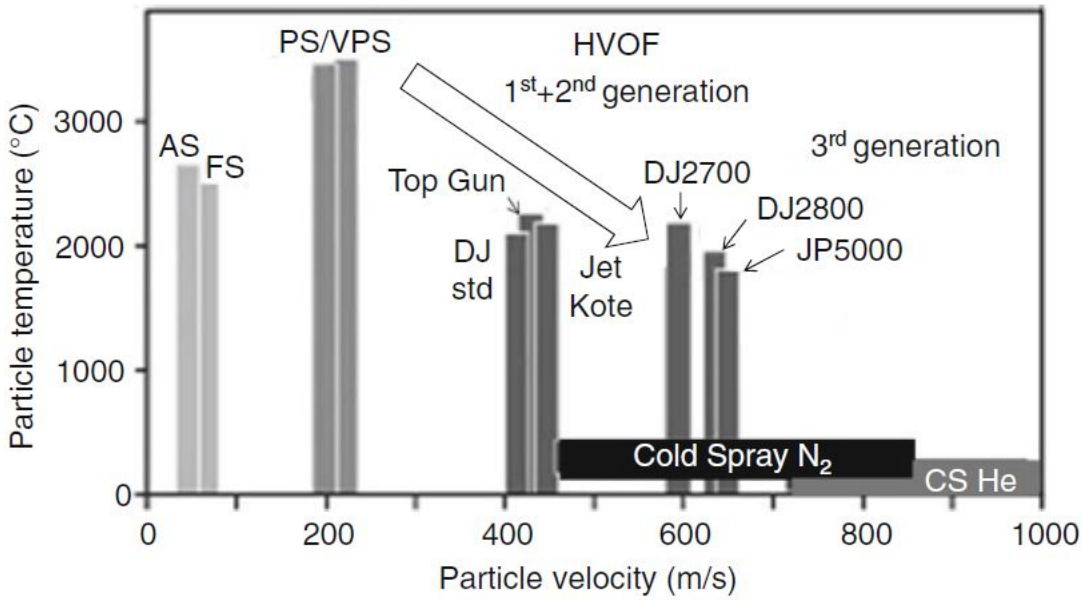

Fig. 1.3 Particle temperatures and velocities obtained in different thermal spray processes, as measured for high-density materials. The arrow indicates the trend of recent developments (AS: Arc spraying, FS: flame spraying, PS: Plasma spraying, VPS: Vacuum plasma spraying, CS: Cold Spray) [19].

The schematic diagram of the Diamond Jet 2700 (DJ2700) (Oerlikon Metco) torch is shown in Fig. 1.4 [20]. The DJ2700 gun uses a combination of oxygen, fuel and air to produce a high-pressure annular flame, which is characterized by a uniform temperature distribution. In this process, the fuel gas (typically methane, propylene or hydrogen) premixed with oxygen is fed from the annular gap to the air cap, where they react to produce high-temperature combustion gases. The exhaust mixture can reach a temperature of 3000 K, very close to the adiabatic flame temperature of the oxygen-methane combustion. The flame is accelerated by a converging/diverging nozzle to become supersonic. Particles are injected axially through the center port with nitrogen as carrier gas. The combustion chamber is cooled with water and air.

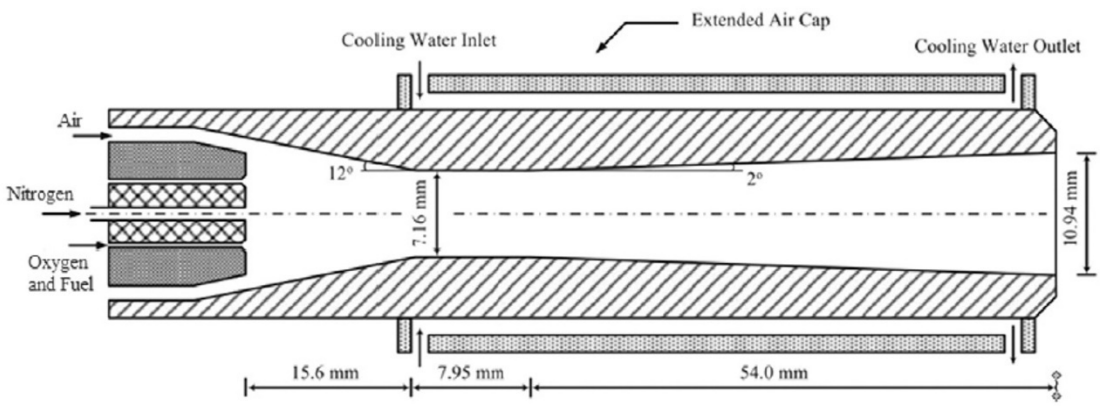

Fig. 1.4 Schematic of the DJ2700 torch [20]

Fig. 1.5 shows the schematic of commercial JP5000 HVOF spray equipment (Praxair-Tafa, Concord, NH, USA) [21]. A mixture of kerosene and oxygen is combusted continuously to generate a supersonic flow of hot gas, into which the powder feedstock is fed radially at a point behind the throat of the nozzle. Nitrogen is used as the carrier gas. The entire spray gun is cooled with water.

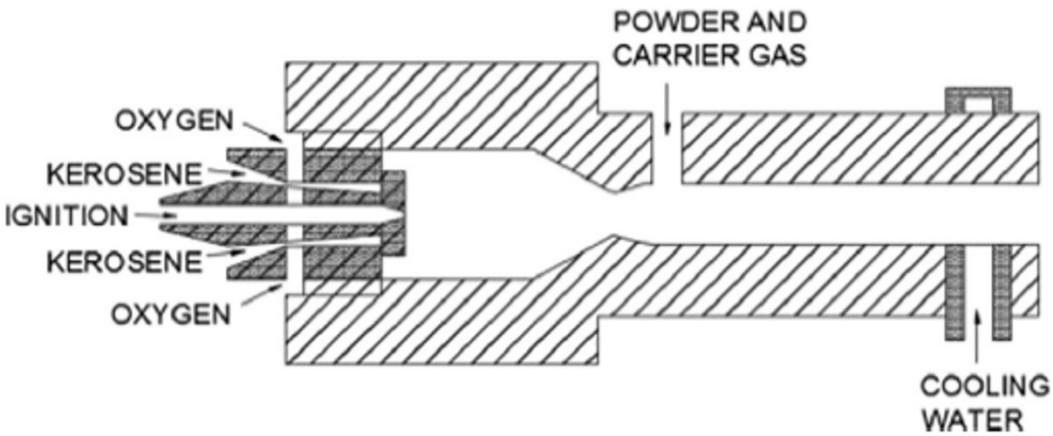

Fig. 1.5 Schematic of the JP5000 torch [21]

The K2 HVOF spray gun (GTV Impex GmbH, Germany) is derived from the famous JP 5000 spray gun. The shape of the combustion chamber and nozzle is the same as that of the latter. Its large combustion chamber and kerosene atomization assembly are combined to produce a finer atomization effect, so as to achieve complete combustion. The GTV K2 spray gun enable preparing not only MCrAlY but also Cr_2C_3-NiCr coatings boasting high-

performances.

1.1.3 Typical coatings sprayed with HVOF process

(1) Metals

Pure aluminum coatings with low porosity were obtained with a low range of oxygen/ fuel ratio using HVOF [22]. Iron-aluminide was sprayed using HVOF with 7–15 wt.% oxide inclusion [23]. Among deposited alloys, the most popular are based on Ni–Cr for which the adherence on stainless steel substrates is very high (more than 100 MPa) and which is not affected by thermal fatigue [24]. Such NiCr or NiCrSiB coatings are used against the severe corrosive environment in waste-to-energy boilers [25, 26]. NiCrMoNb is also used against corrosion [27].

In thermal barrier coatings (TBC), a thin oxide scale, called the thermally grown oxide (TGO), forms upon exposure to high-temperature gases at the bond coat/top coat interface and continues to grow in thickness during thermal cycling. The uneven and rapid growth of the TGO potentially results in localized stress concentrations where cracks can nucleate and initiate a failure process. HVOF coatings of super alloys have been used to achieve dense and uniform α-Al_2O_3 TGO scales with slow growth rates [28-31]. HVOF-sprayed bond coat coatings have been compared to those obtained by plasma spraying (APS and VPS), cold spraying, and D-gun. They have higher aluminum content, and the thermally grown oxide (TGO) developed during cyclic oxidation contains less mixed oxide clusters and a stable Al_2O_3 layer. Thus, the TGO has a low growth rate and low tendency for crack propagation that leads to an improved TBC durability. Fig. 1.6(a) shows the cross section of detonation-sprayed TBC using hollow sphere YSZ powder with the HVOF bond coat. The microstructure of the typical HVOF bond coat of NiCrAlY with a narrow size distribution (47–57 μm) sprayed with JP-5000 HP/HVOF (kerosene–oxygen) is presented in Fig. 1.6(b). It has a lamellar structure and contains dispersed inclusions of aluminum oxide, as well as pores of varying sizes for a total porosity of 3.2 %. Its average roughness Ra is 5.38 μm. The bond coat presents broader and lower diffraction peaks of the γ-Ni_3Al phase than the starting NiCrAlY powder.

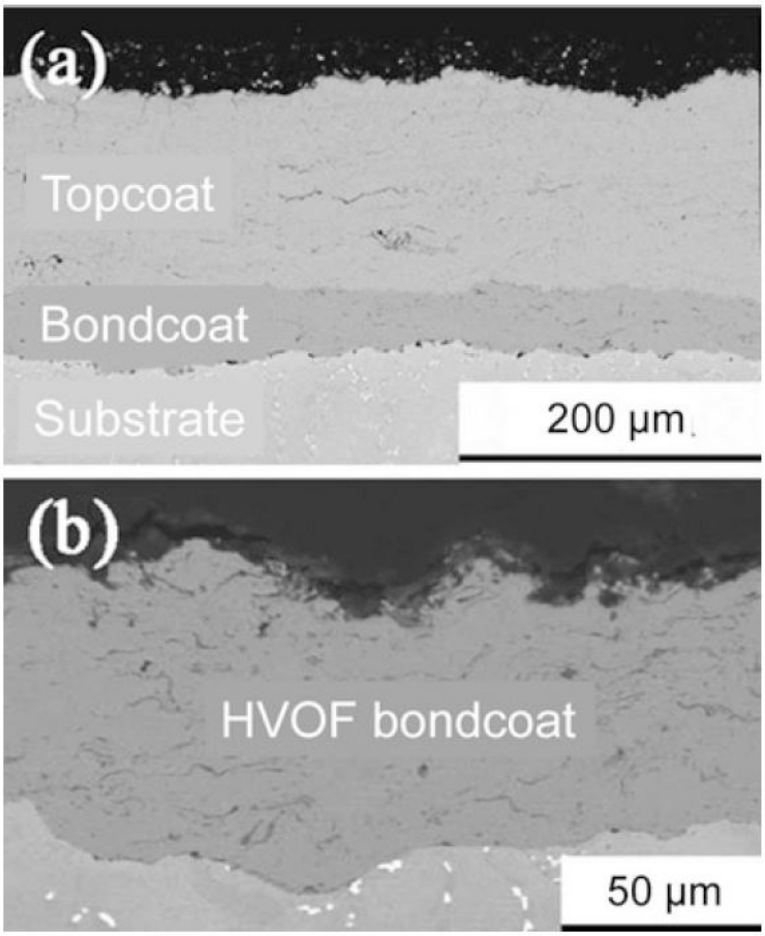

Fig. 1.6 (a) Cross section of a detonation-sprayed TBC using hollow sphere YSZ powder along with the HVOF bond coat. (b) Microstructure of the HVOF NiCrAlY coating in the as-sprayed state [28]

HVOF-sprayed metal coatings (Stellite®6) have excellent resistances to cavitation erosion [32]. Bulk amorphous coatings (NiTiZrSiSn) have also been successfully sprayed with reduced the in-flight oxidation by reducing the oxygen to fuel gas ratio [33].

(2) Cermets

These coatings have been intensively studied from the beginning, and the success of HVOF or HVAF processes substantially relies on them [34-38]. The cermets, which are mostly sprayed, are WC–Co and Cr_3C_2–NiCr. One of the key issues for coating quality is to avoid carbide decomposition or at least to reduce it as much as possible. Spraying with fuel rich mixtures [39] and using HVAF preferably to HVOF [36, 40] allows reducing drastically or even avoiding carbide decomposition. These coatings are used for their wear resistance

(friction and erosion) and corrosion resistance, especially for those containing NiCr. Typical microstructures of WC−10Co−4Cr and Cr_3C_2−25NiCr coatings are shown in Fig. 1.7 [41]. Other sprayed composite materials are also used, such as MoB-CoCr coatings [42] against erosion by molten Al–Zn alloys. In that respect, Ni-TiC coatings [43], silicon nitride-based coatings [44] confer satisfactory corrosion and thermal shock resistance.

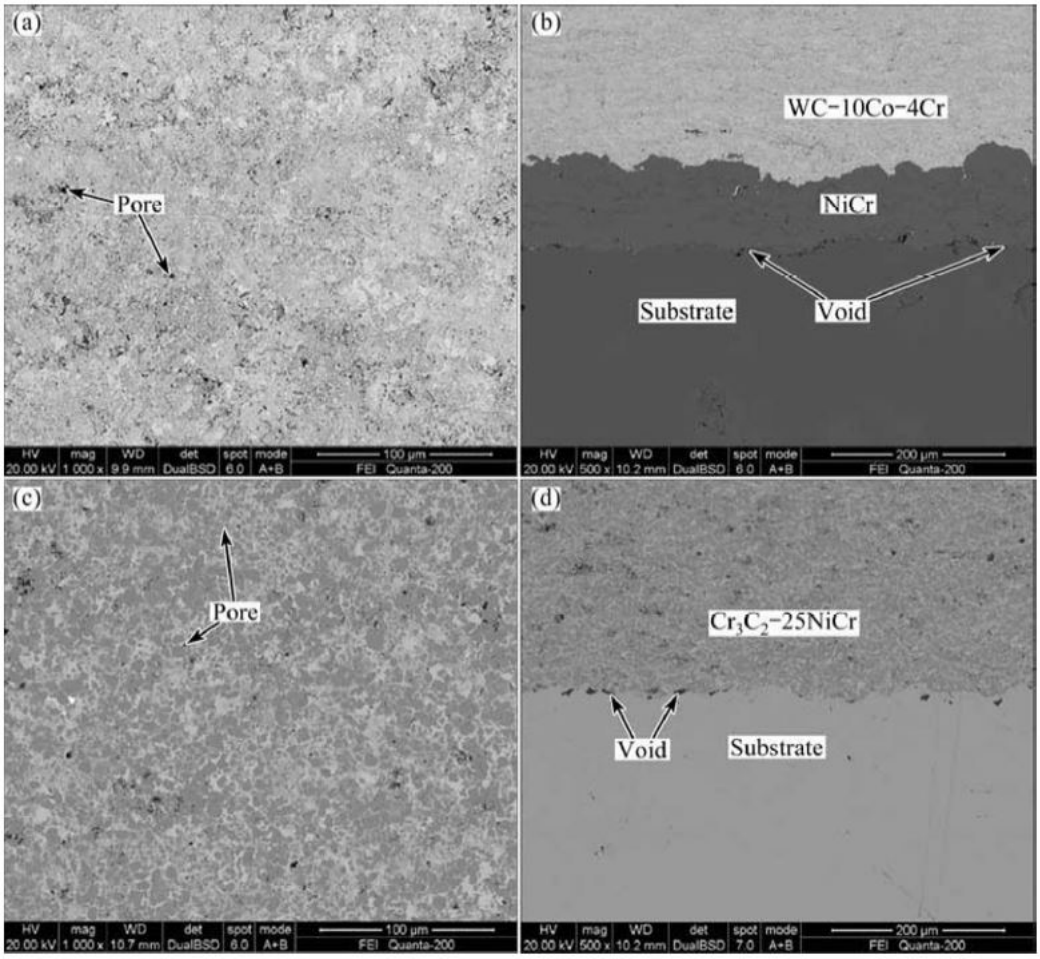

Fig. 1.7 SEM photographs of WC−10Co−4Cr and Cr_3C_2−25NiCr coated on H13 steel: (a) WC−10Co−4Cr (plan view); (b) WC−10Co−4Cr (cross-section); (c) Cr_3C_2−25NiCr (planar view); (d) Cr_3C_2−25NiCr (cross-section) [41]

(3) Ceramics

Ceramic coatings are not the strongest asset of HVOF or HVAF processes because the process is more prone to achieve high velocities than high temperatures. Titania is rather well melted when working with propylene as fuel [45, 46]. High Weibull modulus values are

obtained compared to other spray techniques and coatings are very dense and uniform, rutile being the major phase. Alumina is mostly sprayed with chromia, which allows stabilizing the α phase [47]. At last, yttria- stabilized zirconia with particles below 10 μm can be sprayed, and it is suggested that sintering can play a role, leading to well adhesive and cohesive coatings [48].

(4) Polymers

Among the sprayed polymers Nylon 11 is the one most frequently used, with or without ceramic doping [49-51]. The residence time in the HVOF is generally short enough (~1 ms) to limit its degradation and a change of its color. Such coatings, when used for their dry sliding wear performance, are more wear resistant without doping powders because such additions may lead to abrasive and fatigue wear. Fig. 1.8 shows the microstructure of a pure polyimide coating deposited by HVOF process onto a carbon-fiber reinforced PMC substrate.

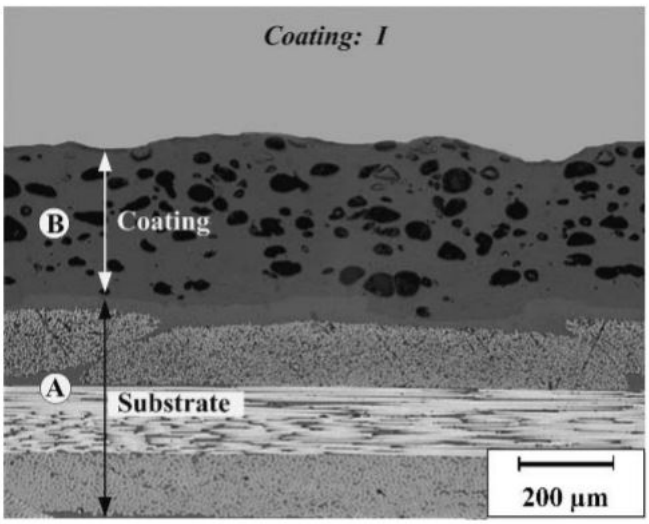

Fig. 1.8 Microstructure of a pure polyimide coating (B) that was HVOF-sprayed onto a carbon-fiber reinforced PMC substrate (A) [50]

1.1.4 Main applications of HVOF processes

The HVOF technology enable producing cermets, metals and a few ceramic protective coatings, which are typically 100–300 μm thick, onto surfaces of engineering components to allow them functioning under extreme conditions. Initially, the focus was on wear resistant

coatings, but now the coatings are rather extensively studied for their corrosion and oxidation resistance which can surpass those produced by other spraying technologies. These coatings have found wide applications in marine, aircraft, automotive, power generation, paper and pulp, petrochemical and other industries.

1.2 HVAF process and modified HVOF process

It is important to avoid or strongly reduce the detrimental oxidation and decarburization processes which undermine many metallic or ceramic coatings (primarily containing carbides). This can be accomplished by lowering the temperature of the gas while increasing its velocity.

1.2.1 Description of the HVAF process

HVAF stands for high velocity air-fuel and was initially developed by J. A. Browning. He used liquid petroleum instead of combustible gas and air instead of oxygen [52]. It requires a flow rate at least 5 times higher than pure oxygen. The combustion chamber pressure typically exceeds 0.8 MPa for a gas flow in the range of 8-10 m^3/min, resulting in very high gas velocities (up to 2,000 m/s) [53]. Evdokimenko et al. have calculated the values of the temperature generated in the chamber of an HVAF gun operating at 1 MPa with three different gases fed in stoichiometric composition [54]. They found 2,383 K for hydrogen, 2,267 K for methane, and 2,321 K for kerosene.

To further improve HVAF systems and obtain good performance coatings, Verstak et al. [55] pioneered the technology of “activated combustion high-velocity air-fuel” (AC-HVAF). Activated combustion implies that fuel molecules are activated by a catalytic medium made by a ceramic plate, allowing combustion to proceed stably at a relatively low temperature and under a wide range of atmospheric pressures. Fig. 1.9 shows a schematic diagram of an AC-HVAF gun (Kermetico AK07) [56]. The AcuKote 07 (AK07) spray gun (Kermetico) uses compressed air as the coolant of the spray gun and the combustion-supporting gas, which greatly reduces not only the spraying cost but also the risk of particles being oxidized. HVAF is used for spraying not only low-melting metals such as aluminum [54], but also nickel-

chromium [57], Fe-base [58-60] or even WC-based [61, 62] and Cr_3C_2-based [63, 64] composite powders due to the faster particle speed and appropriate particle temperature.

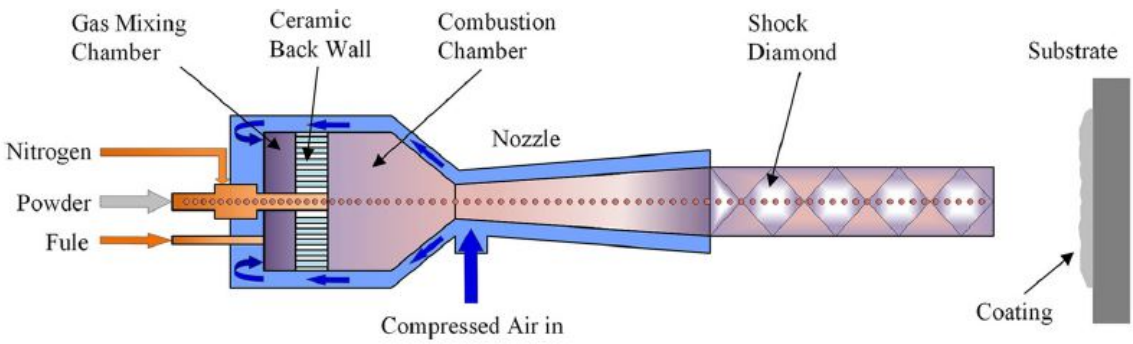

Fig. 1.9 Schematic of a commercial AC-HVAF gun [56]

1.2.2 HVOF process modified with a gas shroud

The modified HVOF device with a gas shroud shown in Fig. 1.10(b) can introduce inert gas under certain flame conditions. It is an improvement of the JP5000 gun (Fig. 1.10 (a)). This equipment provides three benefits: (1) it reduces the temperature of the in-flight particles, (2) it substantially suppresses the oxidation of the sprayed particles, and (3) it increases the velocity of the in-flight particles.

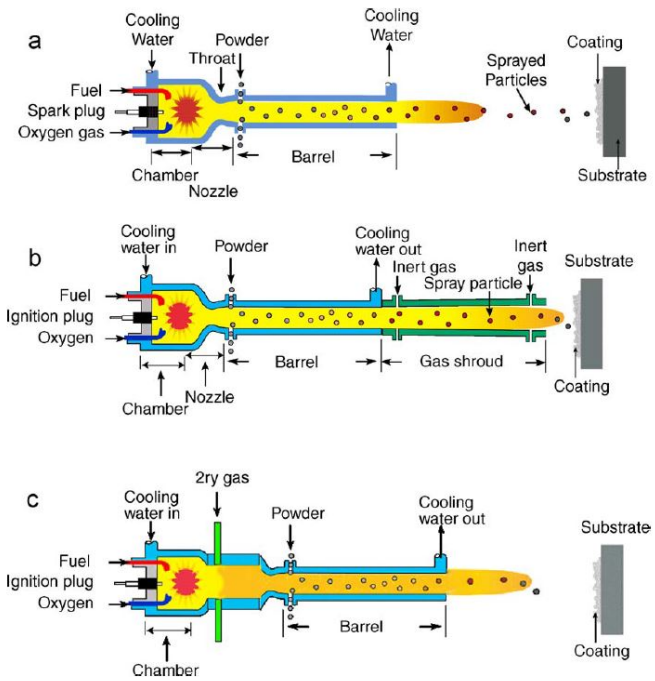

Fig. 1.10 Schematic of (a) commercial high-pressure HVOF (JP5000) device, (b) same device modified with a gas shroud, (c) same device modified with an intermediate mixing chamber [65]

Fig. 1.11 shows the flight velocity and temperature of the WC-20% Cr_3C_2-7% Ni particles that prevail under the three configurations. Without the gas shroud (A-E), the velocity of in-flight particles increases from 680 to 780 m/s as the value of the combustion pressure Pc (shown in Table 1.2) increases from 0.63 to 0.72 MPa. The temperature of in-flight particles almost remains constant around 1950 °C. When the gas shroud is mounted (F-H), the velocity of in-flight particles is 800-850 m/s, and the temperature is about 1800 °C. This result shows that, by using the shroud equipment, the particle temperature drops by 150°, whereas the particle velocity increases [66]. Kawakita et al. [67] also reported that this improved HVOF process achieved the smaller porosity and lower oxide content of HastelloyC coatings, thus significantly improving the resistance to seawater corrosion.

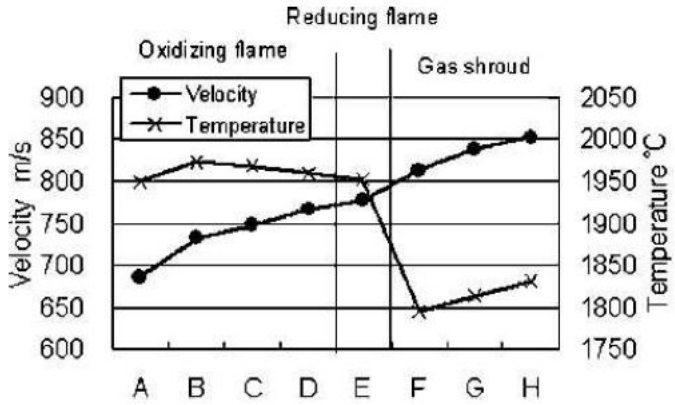

Fig. 1.11 Velocity and temperature of in-flight particles under each condition [66]

Table 1.2 Spraying conditions [66]

Condition	Fuel (l/min)	Oxygen (l/min)	F/O	Pc (MPa)
A	0.32	897	0.73	0.63
B	0.38	991	0.78	0.72
C	0.41	944	0.88	0.72
D	0.44	920	0.98	0.72
E	0.44	826	1.09	0.67
F	0.44	826	1.09	0.67
G	0.47	885	1.09	0.72
H	0.50	944	1.09	0.77

1.2.3 HVOF process modified with an intermediate mixing chamber

Fig. 1.10(c) shows a modification of a HVOF torch starting from a JP5000 gun, in which one has introduced a mixing chamber between the combustion chamber and the powder feed port. Nitrogen is fed into the mixing chamber in order to adjust the temperature and velocity of the combustion gas produced in the combustion chamber. Various coatings with varying oxidation degrees and porosities can be prepared by controlling the nitrogen flow rate. Typical working conditions for this modified HVOF system are listed in Table 1.3. Fig. 1.12 shows the evolution of the oxygen content of titanium coatings when using different nitrogen flow rates. The oxidation level decreases from 5.4 wt.% at 500 slpm N_2 to 0.22 wt.% at 2,000 slpm N_2 due to the cooling of the gas and consequently lower particle temperatures (spray distance 280 mm). However, as shown in Fig. 1.13, the porosity increases with larger average pore size as the

nitrogen flow rate exceeds 1000 slpm. This is clearly demonstrated by the cross-section of the coating shown in Fig. 1.14. Because the particles temperature drops too low, they lose their plasticity and deformability upon impact. As a result, a compromise must be found consisting in determining the suitable nitrogen flow rate. Several examples of depositing heat sensitive materials such as titanium, metallic glass, WC–Co cermet and polymers have been described along with potential industrial applications. The modification of the HVOF process involving such a mixing chamber also offers advantages for depositing materials such as metallic glasses [68], WC-Co cermets [69], oxides [70, 71] and polymers, with potential industrial applications.

Table 1.3 Typical operating conditions [72]

Kerosene (slpm)	Oxygen (slpm)	Nitrogen (slpm)
0.35	732	500
0.33	643	1000
0.30	623	1500
0.29	548	2000

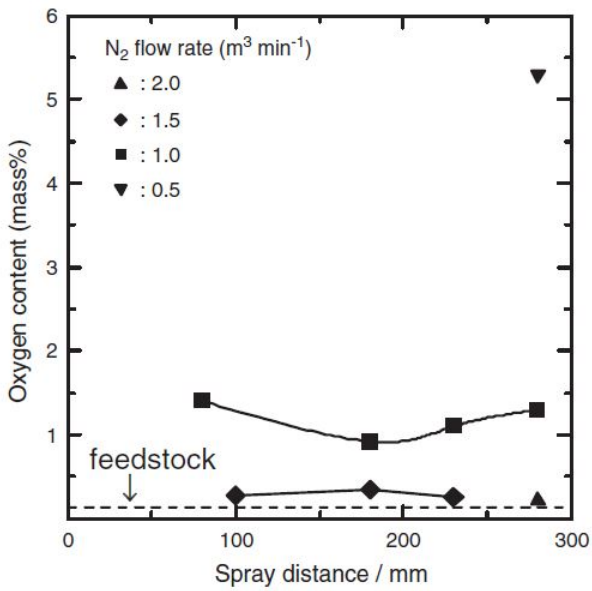

Fig. 1.12 Oxygen content in titanium coatings spayed by the HVOF spraying modified with the addition of a mixing chamber [65]

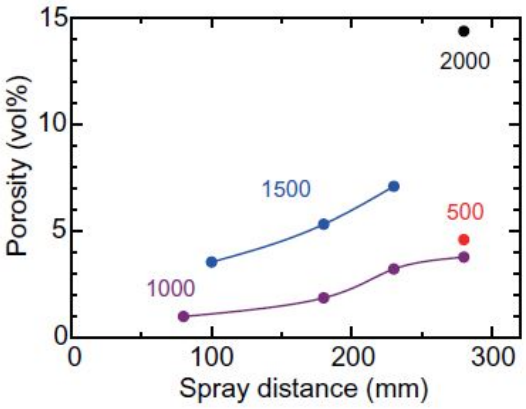

Fig. 1.13 Porosity of Ti coatings fabricated using the modified HVOF process, as function of spray distance [72]

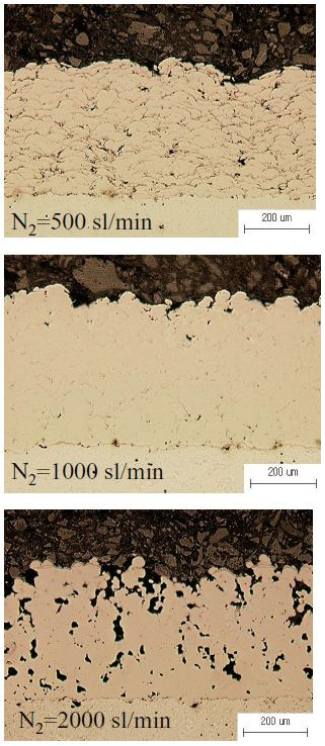

Fig. 1.14 Cross sections of Ti coatings fabricated using the HVOF process modified with the mixing chamber, at three nitrogen flow rates [72]

1.3 The eGun HVOF device fueled with ethanol

1.3.1 Structure and working principle of the eGun HVOF torch

A new type of liquid fuel HVOF process (called “eGun HVOF”), which uses ethanol as

fuel, is - to the author's knowledge - the most recently developed liquid fuel based HVOF technology. It was developed by the Flame Spray Technologies Company in the Netherlands. The schematic of Fig. 1.15 shows the basic design of this spray gun [73]. Ethanol and oxygen are injected, mixed and atomized in the pre-chamber and then ignited. This mixture enters the combustion chamber where high-pressure combustion occurs, which creates a supersonic flame. At the end of the combustion chamber, the powder is radially introduced into the interconnector. After injection into the barrel, the powder is uniformly heated and accelerated to very high speeds and then impacts to the substrates. The length of the barrel is 4 inches (about 100 mm).

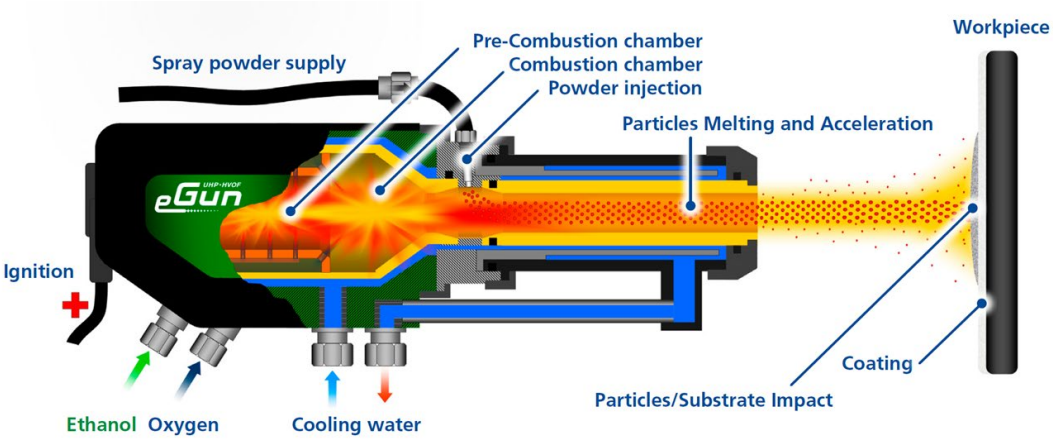

Fig. 1.15 Schematic of eGun HVOF torch [73]

1.3.2 Advantages of choosing ethanol as a liquid fuel

Choosing ethanol as a liquid fuel has several advantages, especially when compared to kerosene. These advantages are in terms of:

(1) Environmentally friendliness:

Burning ethanol results in less toxic emissions and less greenhouse gas emissions.

(2) Sustainability (in case of bioethanol, having thus a non-fossil origin):

Ethanol is renewable and its production is increasing worldwide.

(3) Economy:

Less oxygen consumption and less cooling power are required.

(4) Less oxidation of the resulting coatings:

Ethanol has indeed a lower combustion enthalpy and lower flame temperature, thereby reducing the oxidation of spray materials.

(5) Operational flexibility:

Water or other liquids can be added to ethanol fuel to reduce flame temperature and get still higher particle velocity.

1.3.3 Interest of research on the eGun HVOF process

This ethanol-fueled HVOF process represents a very recent progress in liquid fuel HVOF technology. In order to make better use of the spraying process for the development of coating applications, it is meaningful to understand and study the characteristics of this new spraying process. As mentioned above, ethanol benefits from environmentally friendly features and creates thus less emissions compared to conventional fossil liquid fuels (i.e. kerosene). Therefore, it seems of interest to shift towards such alternative HVOF fuel able to reduce combustion emissions, especially those of carbon dioxide and, in so doing, make thermal spray "greener".

1.4 Objectives of this thesis

In this thesis, an ethanol-fueled HVOF device (called "eGun HVOF") was employed, with the aim to define the merits and limitations of that technology. In view of the limited literature available, it appeared to be of great interest to study the optimization of the spraying parameters of that new spraying process and thoroughly evaluate the performances of the corresponding coatings. In addition, it was foreseen to modify the initial eGun HVOF torch to create an "eGun HVOAF" torch and possibly obtain higher quality coatings. Investigations will be conducted to identify the original features of this technology and investigate the properties of some HVOAF-sprayed coatings. A main objective of this thesis is thus to provide a theoretical and technical foundation for the further development of this technique as well as to explore its potential applications.

Reference

[1] B. Wielage, A. Wank, H. Pokhmurska, T. Grund, C. Rupprecht, G. Reisel, E. Friesen, Development and trends in HVOF spraying technology, Surface and Coatings Technology 201(5) (2006) 2032-2037.

[2] X. Guo, M.-P. Planche, J. Chen, H. Liao, Relationships between in-flight particle characteristics and properties of HVOF sprayed WC-CoCr coatings, Journal of Materials Processing Technology 214(2) (2014) 456-461.

[3] L. Zhao, M. Maurer, F. Fischer, E. Lugscheider, Study of HVOF spraying of WC–CoCr using on-line particle monitoring, Surface and Coatings Technology 185(2-3) (2004) 160-165.

[4] J.A. Picas, M. Punset, M.T. Baile, E. Martín, A. Forn, Effect of oxygen/fuel ratio on the in-flight particle parameters and properties of HVOF WC-CoCr coatings, Surface and Coatings Technology 205 (2011) S364-S368.

[5] Oerlikon Metco, an Introduction to Thermal Spray, Issue 4 • c 2013 Oerlikon Metco.

[6] T. Sidhu, S. Prakash, R. Agrawal, Studies on the properties of high-velocity oxy-fuel thermal spray coatings for higher temperature applications, Materials Science 41(6) (2005) 805-823.

[7] A. Boudi, M. Hashmi, B. Yilbas, HVOF coating of Inconel 625 onto stainless and carbon steel surfaces: corrosion and bond testing, Journal of materials processing technology 155 (2004) 2051-2055.

[8] R. Lima, K. Khor, H. Li, P. Cheang, B. Marple, HVOF spraying of nanostructured hydroxyapatite for biomedical applications, Materials Science and Engineering: A 396(1-2) (2005) 181-187.

[9] M. Planche, H. Liao, B. Normand, C. Coddet, Relationships between NiCrBSi particle characteristics and corresponding coating properties using different thermal spraying processes, Surface and Coatings Technology 200(7) (2005) 2465-2473.

[10] A. Wank, B. Wielage, G. Reisel, T. Grund, E. Friesen, Performance of thermal spray coatings under dry abrasive wear conditions, The Coatings, Fourth Int. Conf. Proc, 2004, pp. 5-7.

[11] Y. Qiao, Y. Liu, T.E. Fischer, Sliding and abrasive wear resistance of thermal-sprayed WC-Co coatings, Journal of Thermal Spray Technology 10(1) (2001) 118-125.

[12] M. Xie, S. Zhang, M. Li, Comparative investigation on HVOF sprayed carbide-based coatings, Applied Surface Science 273 (2013) 799-805.

[13] T.C. Totemeier, R.N. Wright, W.D. Swank, FeAl and Mo–Si–B intermetallic coatings prepared by thermal spraying, Intermetallics 12(12) (2004) 1335-1344.

[14] T.C. Totemeier, R.N. Wright, W.D. Swank, Microstructure and stresses in HVOF sprayed iron aluminide coatings, Journal of thermal spray technology 11(3) (2002) 400-408.

[15] T.C. Totemeier, R.N. Wright, W.D. Swank, Residual stresses in high-velocity oxy-fuel metallic coatings, Metallurgical and materials transactions A 35(6) (2004) 1807-1814.

[16] J.A. Browning, Highly concentrated supersonic liquified material flame spray method and apparatus, Google Patents, 1983.

[17] M. Thorpe, H. Richter, A pragmatic analysis and comparison of HVOF processes, Journal of Thermal Spray Technology 1(2) (1992) 161-170.

[18] K. Ishikawa, T. Suzuki, S. Tobe, Y. Kitamura, Resistance of thermal-sprayed duplex coating composed of aluminum and 80Ni-20Cr alloy against aqueous corrosion, Journal of thermal spray technology 10(3) (2001) 520-525.

[19] F. Gärtner, T. Stoltenhoff, T. Schmidt, H. Kreye, The cold spray process and its potential for industrial applications, Journal of Thermal Spray Technology 15(2) (2006) 223-232.

[20] D. Sciti, L. Zoli, L. Silvestroni, A. Cecere, G. Di Martino, R. Savino, Design, fabrication and high velocity oxy-fuel torch tests of a Cf-ZrB2-fiber nozzle to evaluate its potential in rocket motors, Materials & Design 109 (2016) 709-717.

[21] M.S. Lamana, A.G. Pukasiewicz, S. Sampath, Influence of cobalt content and HVOF deposition process on the cavitation erosion resistance of WC-Co coatings, Wear 398 (2018) 209-219.

[22] R. Chow, T. Decker, R. Gansert, D. Gansert, D. Lee, Properties of aluminum deposited by a HVOF process, Journal of thermal spray technology 12(2) (2003) 208-213.

[23] T.C. Totemeier, R.N. Wright, W.D. Swank, Mechanical and physical properties of high-velocity oxy-fuel-sprayed iron aluminide coatings, Metallurgical and Materials Transactions A 34(10) (2003) 2223-2231.

[24] V. Higuera, F. Belzunce, A. Carriles, S. Poveda, Influence of the thermal-spray procedure on the properties of a nickel-chromium coating, Journal of materials science 37(3) (2002) 649-654.

[25] C.-J. Li, Y.-Y. Wang, Effect of particle state on the adhesive strength of HVOF sprayed metallic

coating, Journal of Thermal Spray Technology 11(4) (2002) 523-529.

[26] Y. Kawahara, Application of high temperature corrosion-resistant materials and coatings under severe corrosive environment in waste-to-energy boilers, Journal of thermal spray technology 16(2) (2007) 202-213.

[27] B. Yilbas, B. Abdul-Aleem, M. Khalid, Corrosion behavior of HVOF coated sheets, Journal of thermal spray technology 12(4) (2003) 572-575.

[28] F. Yuan, Z. Chen, Z. Huang, Z. Wang, S. Zhu, Oxidation behavior of thermal barrier coatings with HVOF and detonation-sprayed NiCrAlY bondcoats, Corrosion science 50(6) (2008) 1608-1617.

[29] A. Fossati, M. Di Ferdinando, A. Lavacchi, U. Bardi, C. Giolli, A. Scrivani, Improvement of the isothermal oxidation resistance of CoNiCrAlY coating sprayed by High Velocity Oxygen Fuel, Surface and Coatings Technology 204(21-22) (2010) 3723-3728.

[30] P. Richer, M. Yandouzi, L. Beauvais, B. Jodoin, Oxidation behaviour of CoNiCrAlY bond coats produced by plasma, HVOF and cold gas dynamic spraying, Surface and Coatings Technology 204(24) (2010) 3962-3974.

[31] B. Rajasekaran, G. Mauer, R. Vaßen, Enhanced characteristics of HVOF-sprayed MCrAlY bond coats for TBC applications, Journal of thermal spray technology 20(6) (2011) 1209-1216.

[32] A. Kumar, J. Boy, R. Zatorski, L. Stephenson, Thermal spray and weld repair alloys for the repair of cavitation damage in turbines and pumps: a technical note, Journal of thermal spray technology 14(2) (2005) 177-182.

[33] H. Choi, S. Lee, B. Kim, H. Jo, C. Lee, Effect of in-flight particle oxidation on the phase evolution of HVOF NiTiZrSiSn bulk amorphous coating, Journal of materials science 40(23) (2005) 6121-6126.

[34] A. Dent, S. DePalo, S. Sampath, Examination of the wear properties of HVOF sprayed nanostructured and conventional WC-Co cermets with different binder phase contents, Journal of thermal spray technology 11(4) (2002) 551-558.

[35] J.M. Perry, T. Hodgkiess, A. Neville, A comparison of the corrosion behavior of WC-Co-Cr and WC-Co HVOF thermally sprayed coatings by in situ atomic force microscopy (AFM), Journal of thermal spray technology 11(4) (2002) 536-541.

[36] C. Deng, M. Liu, C. Wu, K. Zhou, J. Song, Impingement resistance of HVAF WC-based coatings,

Journal of thermal spray technology 16(5-6) (2007) 604-609.

[37] J. Guilemany, N. Espallargas, J. Fernández, P. Suegama, A. Benedetti, High-velocity oxyfuel Cr 3 C 2-NiCr replacing hard chromium coatings, Journal of thermal spray technology 14(3) (2005) 335-341.

[38] G.-C. Ji, C.-J. Li, Y.-Y. Wang, W.-Y. Li, Erosion performance of HVOF-sprayed Cr 3 C 2-NiCr coatings, Journal of Thermal Spray Technology 16(4) (2007) 557-565.

[39] M. Parco, L. Zhao, J. Zwick, K. Bobzin, E. Lugscheider, Investigation of HVOF spraying on magnesium alloys, Surface and Coatings Technology 201(6) (2006) 3269-3274.

[40] L. Jacobs, M. Hyland, M. De Bonte, Study of the influence of microstructural properties on the sliding-wear behavior of HVOF and HVAF sprayed WC-cermet coatings, Journal of thermal spray technology 8(1) (1999) 125-132.

[41] W.-c. Zhang, L.-b. Liu, M.-t. Zhang, G.-x. Huang, J.-s. Liang, L. Xian, L.-g. Zhang, Comparison between WC–10Co–4Cr and Cr3C2–25NiCr coatings sprayed on H13 steel by HVOF, Transactions of nonferrous metals society of china 25(11) (2015) 3700-3707.

[42] H. Mizuno, J. Kitamura, MoB/CoCr cermet coatings by HVOF spraying against erosion by molten Al-Zn alloy, Journal of Thermal Spray Technology 16(3) (2007) 404-413.

[43] A. Horlock, Z. Sadeghian, D. McCartney, P. Shipway, High-velocity oxyfuel reactive spraying of mechanically alloyed Ni-Ti-C powders, Journal of thermal spray technology 14(1) (2005) 77-84.

[44] S. Thiele, L.-M. Berger, M. Herrmann, M. Nebelung, R. Heimann, T. Schnick, B. Wielage, P. Vuoristo, Microstructure and properties of thermally sprayed silicon nitride-based coatings, Journal of thermal spray technology 11(2) (2002) 218-225.

[45] R. Lima, B.R. Marple, High Weibull modulus HVOF titania coatings, Journal of thermal spray technology 12(2) (2003) 240-249.

[46] R. Lima, B. Marple, Optimized HVOF titania coatings, Journal of Thermal spray technology 12(3) (2003) 360-369.

[47] C.C. Stahr, S. Saaro, L.-M. Berger, J. Dubský, K. Neufuss, M. Herrmann, Dependence of the Stabilization of α-Alumina on the Spray Process, Journal of thermal spray technology 16(5-6) (2007) 822-830.

[48] T.A. Dobbins, R. Knight, M.J. Mayo, HVOF thermal spray deposited Y 2 O 3-stabilized ZrO 2 coatings for thermal barrier applications, Journal of Thermal spray technology 12(2) (2003) 214-225.

[49] E. Petrovicova, R. Knight, L. Schadler, T. Twardowski, Nylon 11/silica nanocomposite coatings applied by the HVOF process. II. Mechanical and barrier properties, Journal of Applied Polymer Science 78(13) (2000) 2272-2289.

[50] M. Ivosevic, R. Knight, S.R. Kalidindi, G.R. Palmese, J.K. Sutter, Adhesive/cohesive properties of thermally sprayed functionally graded coatings for polymer matrix composites, Journal of Thermal Spray Technology 14(1) (2005) 45-51.

[51] L. Jackson, M. Ivosevic, R. Knight, R. Cairncross, Sliding wear properties of HVOF thermally sprayed nylon-11 and nylon-11/ceramic composites on steel, Journal of thermal spray technology 16(5-6) (2007) 927-932.

[52] J. Browning, Hypervelocity impact fusion—a technical note, Journal of Thermal Spray Technology 1(4) (1992) 289-292.

[53] J. Browning, Viewing the future of high-velocity oxyfuel (HVOF) and high-velocity air fuel (HVAF) thermal spraying, Journal of Thermal Spray Technology 8(3) (1999) 351.

[54] V.K. Kadyrov, O.I. Getman, High-velocity flame spraying of powder aluminum protective coatings, Powder Metallurgy and Metal Ceramics 40(3) (2001) 121-126.

[55] A. Verstak, V. Baranovski, AC-HVAF sprayed tungsten carbide: properties and applications, Thermal Spray 2006: Building on 100 Years of Success (2006) 643-648.

[56] X. Gao, C. Li, Y. Xu, X. Chen, X. Han, Effects of Fuel Types and Process Parameters on the Performance of an Activated Combustion High Velocity Air-Fuel (AC-HVAF) Thermal Spray System, Journal of Thermal Spray Technology (2021) 1-16.

[57] W. Trompetter, A. Markwitz, M. Hyland, P. Munroe, Evidence of mechanical interlocking of NiCr particles thermally sprayed onto Al substrates, Journal of thermal spray technology 14(4) (2005) 524-529.

[58] E. Sadeghimeresht, N. Markocsan, P. Nylen, Microstructural characteristics and corrosion behavior of HVAF-and HVOF-sprayed Fe-based coatings, Surface and Coatings Technology 318 (2017) 365-373.

[59] A. Milanti, V. Matikainen, H. Koivuluoto, G. Bolelli, L. Lusvarghi, P. Vuoristo, Effect of spraying parameters on the microstructural and corrosion properties of HVAF-sprayed Fe–Cr–Ni–B–C coatings, Surface and Coatings Technology 277 (2015) 81-90.

[60] R. Guo, C. Zhang, Q.e. Chen, Y. Yang, N. Li, L. Liu, Study of structure and corrosion resistance of Fe-based amorphous coatings prepared by HVAF and HVOF, Corrosion Science 53(7) (2011) 2351-2356.

[61] Q. Wang, Z. Tang, L. Cha, Cavitation and sand slurry erosion resistances of WC-10Co-4Cr coatings, Journal of Materials Engineering and Performance 24(6) (2015) 2435-2443.

[62] Q. Wang, S. Zhang, Y. Cheng, J. Xiang, X. Zhao, G. Yang, Wear and corrosion performance of WC-10Co4Cr coatings deposited by different HVOF and HVAF spraying processes, Surface and Coatings Technology 218 (2013) 127-136.

[63] V. Matikainen, H. Koivuluoto, P. Vuoristo, A study of Cr3C2-based HVOF-and HVAF-sprayed coatings: Abrasion, dry particle erosion and cavitation erosion resistance, Wear 446 (2020) 203188.

[64] V. Matikainen, G. Bolelli, H. Koivuluoto, P. Sassatelli, L. Lusvarghi, P. Vuoristo, Sliding wear behaviour of HVOF and HVAF sprayed Cr3C2-based coatings, Wear 388 (2017) 57-71.

[65] J. Kawakita, S. Kuroda, T. Fukushima, H. Katanoda, K. Matsuo, H. Fukanuma, Dense titanium coatings by modified HVOF spraying, Surface and Coatings Technology 201(3-4) (2006) 1250-1255.

[66] Y. Ishikawa, J. Kawakita, S. Kuroda, S. Osawa, T. Itsukaichi, Y. Sakamoto, M. Takaya, Evaluation of corrosion and wear resistance of hard cermet coatings sprayed by using an improved HVOF process, Journal of thermal spray technology 14(3) (2005) 384-390.

[67] J. Kawakita, S. Kuroda, T. Fukushima, T. Kodama, Corrosion resistance of HastelloyC coatings formed by an improved HVOF thermal spraying process, Materials Transactions 44(2) (2003) 253-258.

[68] J. Kawakita, N. Maruyama, S. Kuroda, S. Hiromoto, A. Yamamoto, Fabrication and mechanical properties of composite structure by warm spraying of Zr-base metallic glass, Materials transactions (2008) 0712250284-0712250284.

[69] P. Chivavibul, M. Watanabe, S. Kuroda, K. Shinoda, Effects of carbide size and Co content on the microstructure and mechanical properties of HVOF-sprayed WC–Co coatings, Surface and Coatings Technology 202(3) (2007) 509-521.

[70] J. Kawakita, T. Shinohara, S. Kuroda, M. Suzuki, S. Sodeoka, Fabrication of nano-sized oxide composite coatings and photo-electric conversion/electron storage characteristics, Surface and Coatings Technology 202(16) (2008) 4028-4035.

[71] K. Onizawa, J. Kawakita, S. Kuroda, T. Shinohara, M. Suzuki, S. Sodeoka, Y. Sakamoto, Coating Fabrication of Nano-Sized Oxides/Metal Composite by Warm Spray and its Photo-Cathodic Protection Behaviour, Journal of Solid Mechanics and Materials Engineering 2(1) (2008) 156-165.

[72] S. Kuroda, J. Kawakita, M. Watanabe, H. Katanoda, Warm spraying—a novel coating process based on high-velocity impact of solid particles, Science and technology of advanced materials (2008).

[73] https://www.fst.nl/systems/thermal-spray-guns-and-torches/egun-hvof-spray-gun/

Chapter 2 Experimental Materials and Methods

2.1 Spraying equipment

In this thesis, the thermal spray activity has been carried out using the eGun HVOF system (Flame Spray Technologies B.V., The Netherlands), while using ethanol as the liquid fuel. The schematic of the eGun HVOF torch is visible in Fig. 2.1, and a photograph is shown in Fig. 2.2. Ethanol and oxygen are injected, mixed and atomized in the pre-chamber and then ignited. This mixture enters the combustion chamber where high-pressure combustion occurs, which creates a supersonic flame. At the end of the combustion chamber, the powder is radially injected into the interconnector. After injection into the barrel, the powder is uniformly heated and accelerated to very high speeds and then impacts to the substrates. The length of the barrel is 4 inches.

We have also worked on an eGun HVOAF device, which has been derived from the eGun HVOF one and was intended to develop higher particle velocities and lower particle temperatures. Fig. 2.3 shows a photograph of that novel HVOAF torch. To reach this goal, we have modified the spray gun of the eGun HVOF system by intercalating a second-stage combustion chamber between the combustion chamber and the powder feed port, which enables adding compressed air to the combustion gas. In other words, the mixture of ethanol and oxygen is first combusted continuously to generate a hot gas, into which compressed air is then injected through the mixing chamber inserted between the combustion chamber and the nozzle. By adjusting the flow rate of the added compressed air injected, the microstructure and various properties of the coatings can be controlled.

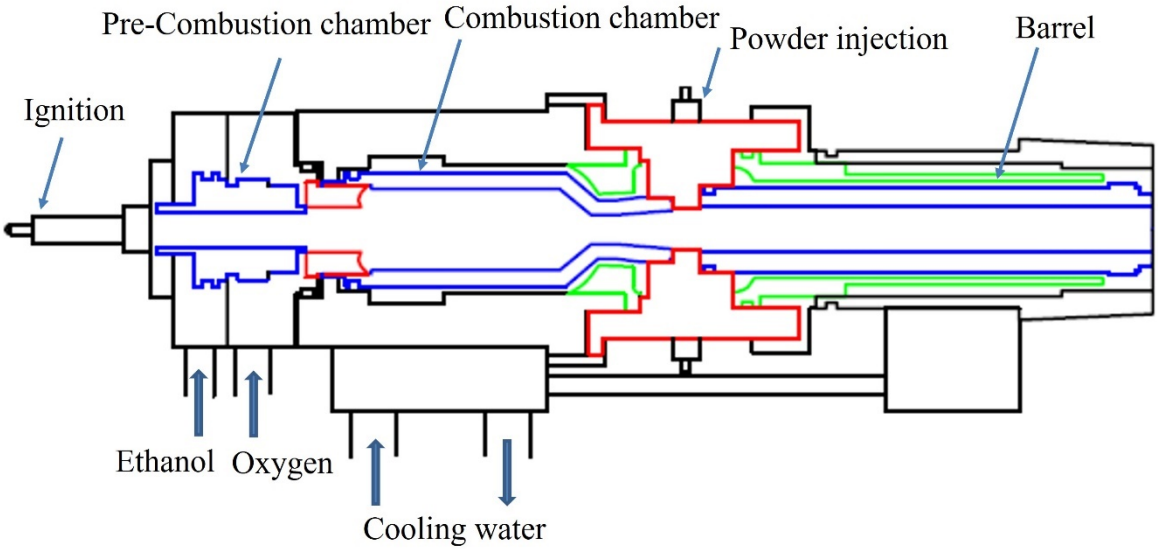

Fig. 2.1 Schematic geometry of the eGun HVOF torch

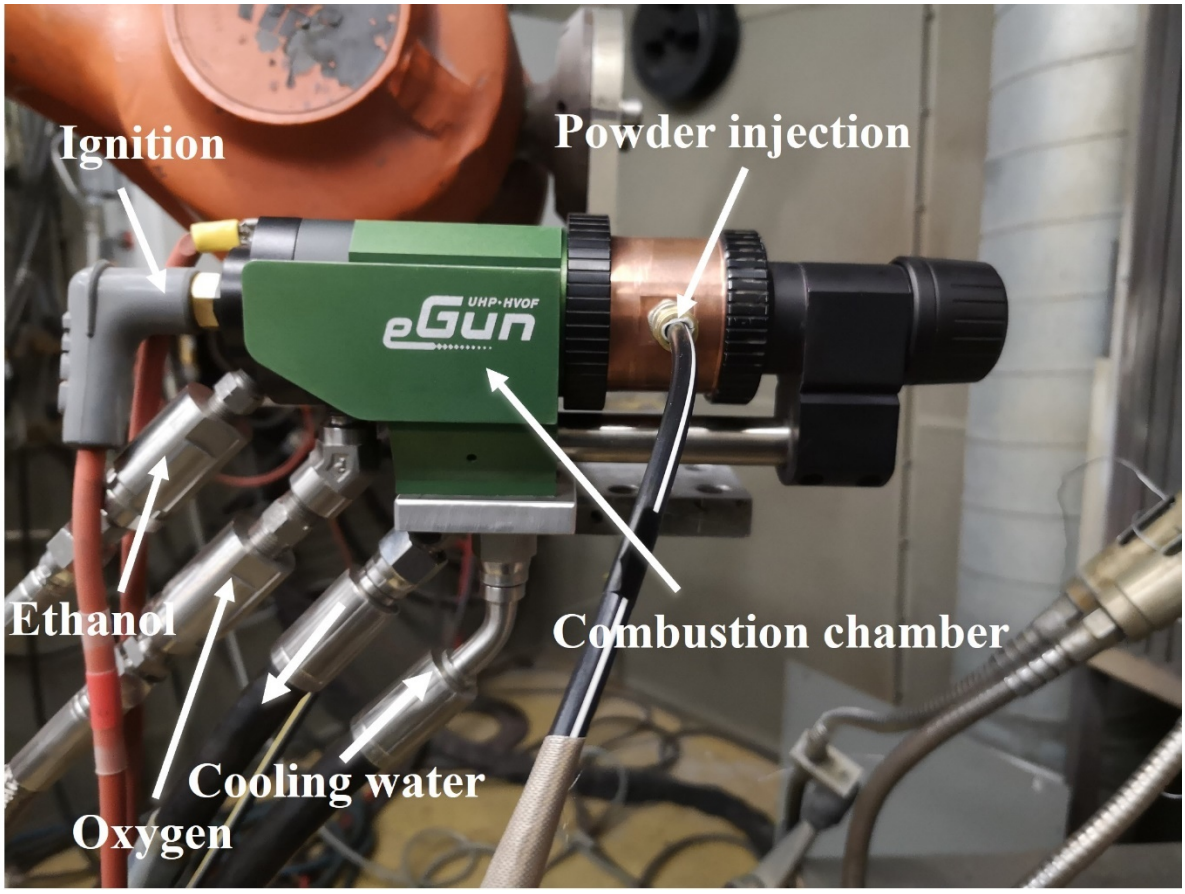

Fig. 2.2 Photograph of the eGun HVOF torch

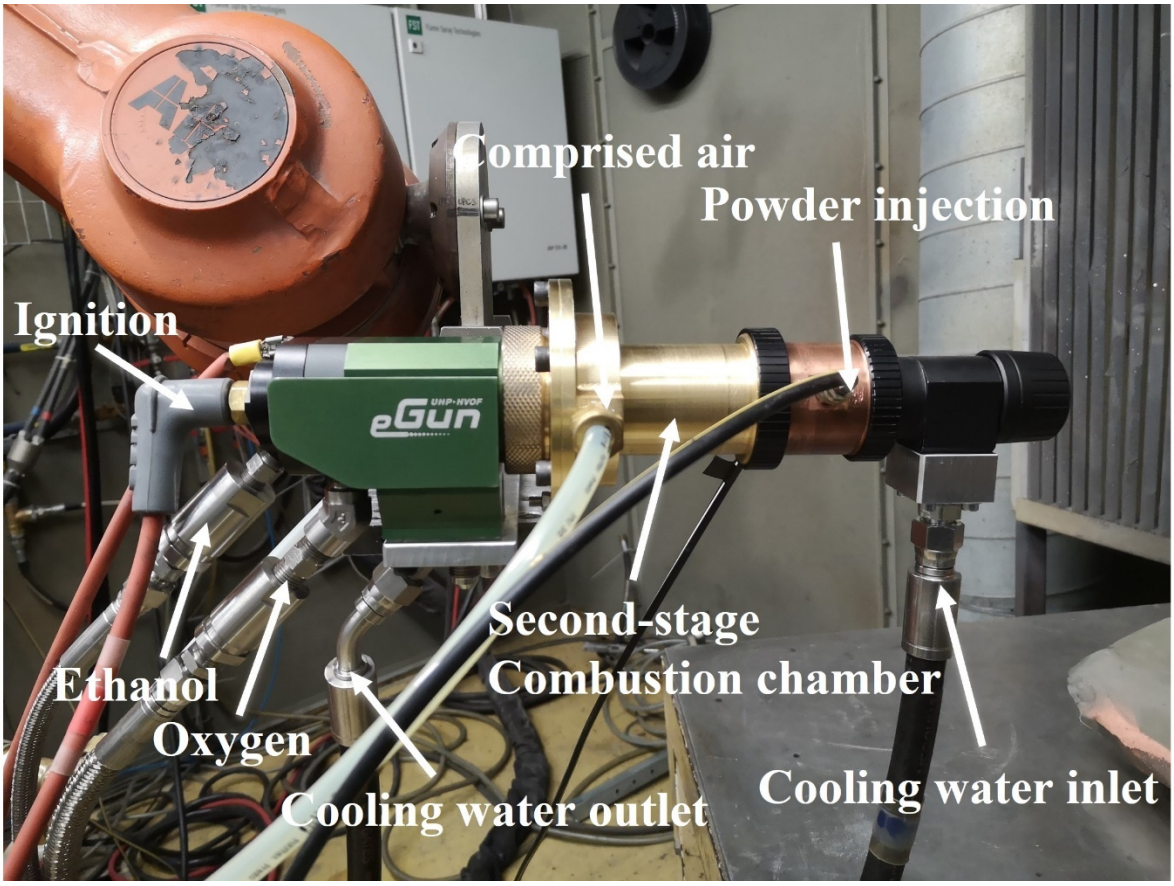

Fig. 2.3 Photograph of the novel eGun HVOAF torch

2.2 Materials

2.2.1 Powders

Three kinds of powder were used in this thesis. In chapter 3, commercially available WC-10%wtCo-4%wtCr (WOKA 3653, Oerlikon Metco, Switzerland) powder was used as the feedstock. The agglomerated powder was received with a nominal size distribution of 10 – 45 μm. Fig. 2.4(a) and (b) show an overview and magnified surface morphologies of the used WC-10Co4Cr powder observed by SEM. They show that the spray powder exhibits good spherical shape. In addition, the single particle of the powder is composed of binder phases (Co，Cr), coarse and fine WC grains and many pores are visible on the surface of the WC-10Co4Cr particles. The spherical shape of the particles contributes to powder feeding, and the micro pores on their surface are favorable for a homogenous heating of particles in the flame plume

[1]. The cross-sectional microstructure of the feedstock particle is shown in Fig. 2.4(c), which illustrates more clearly the distribution of the carbides and binder phases. Fig. 2.4(d) shows that the d50 of the WC-10Co4Cr powder particles is 31.8 μm, an average of three continuous measurements determined by a laser diffraction sizer (Mastersizer 2000, Malvern Instruments Ltd., UK).

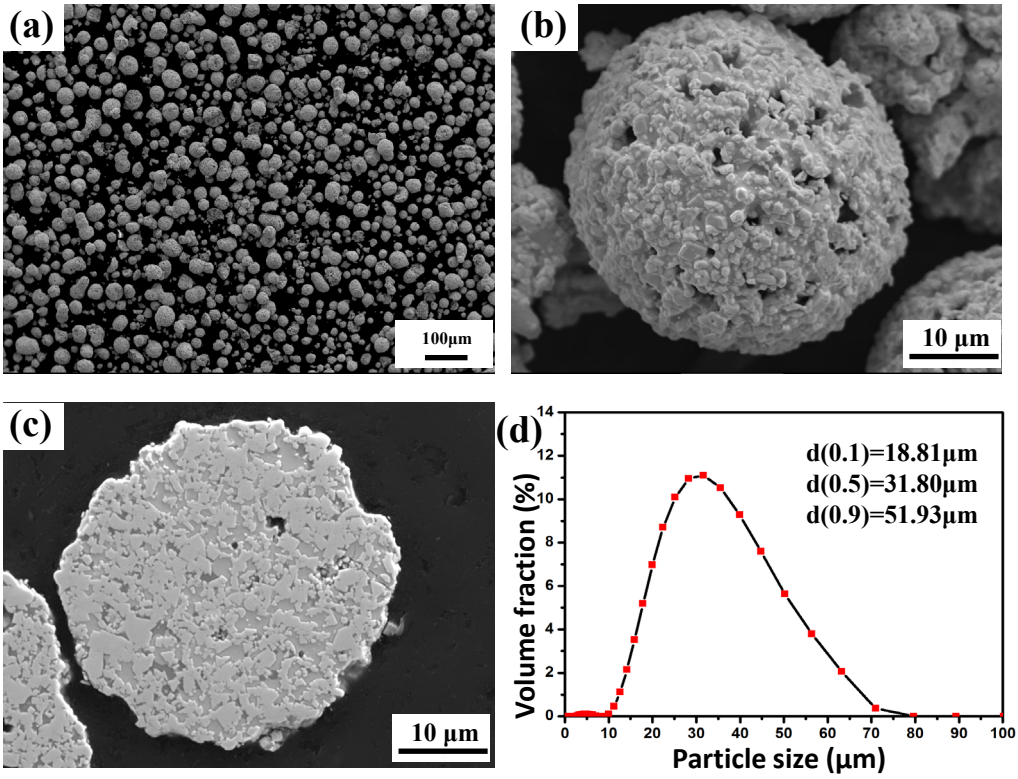

Fig. 2.4 WC-10Co4Cr feedstock particles used in this work: (a) and (b) overview and magnified SEM images; (c) cross section showing its microstructures; (d) particle size distribution

In chapter 4, commercially available 75wt%Cr_3C_2–25wt%NiCr powder (K-584.23, Flame Spray Technologies B.V., The Netherlands) with a nominal size distribution of 11 - 45 μm was used as feedstock. The received powder is nearly spherical as shown in Fig. 2.5(a), which is favorable for powder feeding. The BSE image of the cross section of the powder (Fig. 2.5(b)) shows a clear contrast between the carbide and NiCr matrix phases. The carbide grains are evenly distributed, forming an interconnected network in each powder particle. The d50 of the feedstock powder particles is about 37.7 μm (Fig. 2.5(c)), an average of three continuous

measurements determined by a laser diffraction sizer (Mastersizer 2000, Malvern Instruments Ltd., UK).

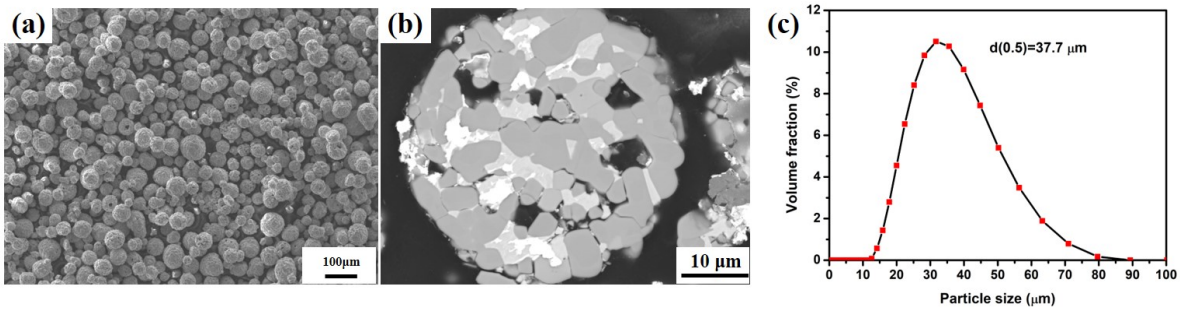

Fig. 2.5 Cr_3C_2–NiCr feedstock powder: (a) SEM image of the overview, (b) BSE image of the cross section of the powder, (c) particle size distribution

In chapter 5, the commercial Ni-23Co-20Cr-8.5Al-0.6Y-4Ta powders with a nominal size distribution of 5 - 38 μm (Amdry 997, Oerlikon Metco, Switzerland) were used. The morphology of the raw material powder is presented in Fig. 2.6(a), which shows that the powder is also spherical. An EDS analysis of the powder surface is visible in Fig. 2.6(b): the result is basically in line with the specified composition Ni-23Co-20Cr-8.5Al-4Ta-0.6Y. The powder particle size distribution is shown in Fig. 2.6(c), with a d50 of 20.3 μm. The XRD pattern shown in Fig. 2.6(d) demonstrates that the powder is composed of γ-Ni, β-NiAl and γ′-Ni_3Al phases.

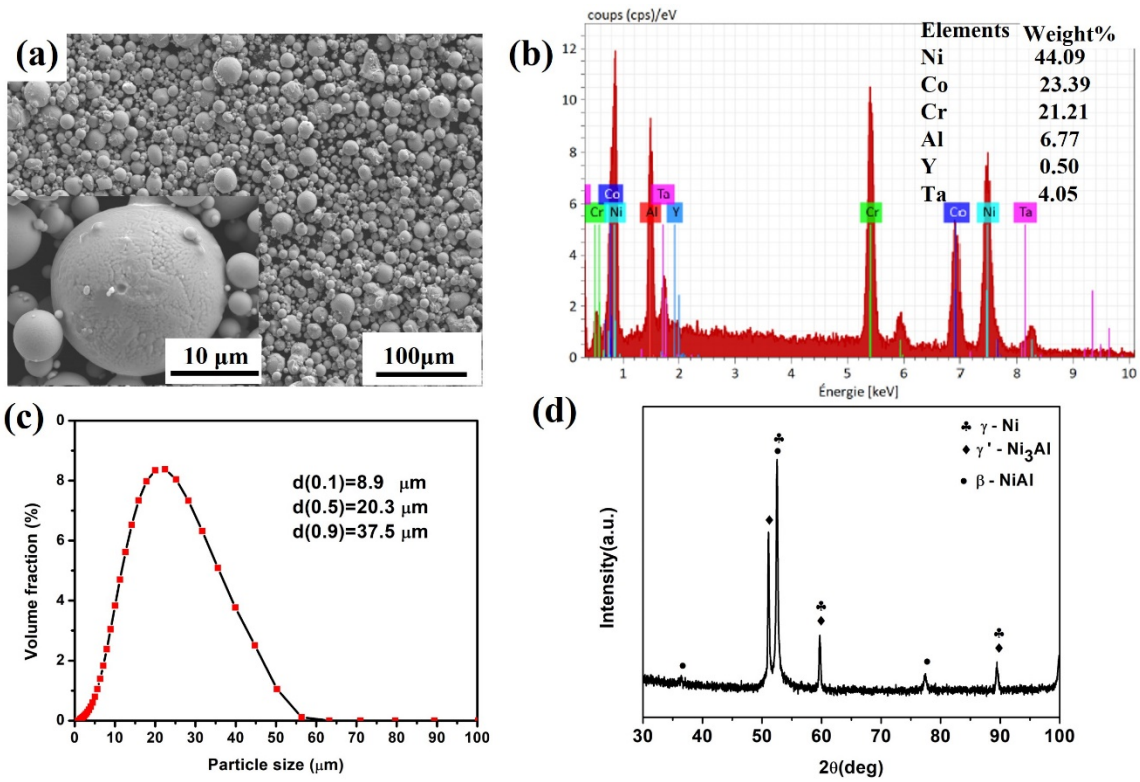

Fig. 2.6 NiCoCrAlYTa powders used in this work: (a) overview and magnified SEM images; (b) EDS analysis of the surface; (c) particle size distribution; (d) XRD patterns

2.2.2 Substrates

Some 304 stainless steels with dimensions of 50 mm × 25 mm × 2 mm were used as the substrates of the coatings for the erosion tests and the associated microstructure analyses. Some 304 stainless steels with dimensions of size of Φ 25mm × 5mm were used for the bond strength tests and the sliding wear tests. Prior to the spraying process, all substrates were degreased and grit-blasted with 30 meshes Al_2O_3 in order to improve the bonding strength between the coating and substrate.

2.3 Coatings preparation

This thesis involves two spraying processes, which are the eGun HVOF and HVOAF processes. As mentioned in section 2.1, the HVOAF process spray gun was derived from the HVOF one by adding a second stage combustion chamber, through which compressed air

system is introduced. The flow of compressed air can be changed to vary and study the performance and microstructure of the resulting coatings. The optimization of the other spraying parameters is also essential in order to obtain high-quality coatings. Therefore, various values of the oxygen flow rate, ethanol flow rate, standoff distance, powder feed rate settings have been tested, as reported in the following chapters. The spray guns of the two spraying devices were mounted on a programmable 6-axis robot (ABB IRB 1400). The substrates were fixed on the homemade holder. Specimens were cooled during and after spraying with compressed air jets. The thickness of all the coatings was kept in the range of 200-400mm.

2.4 Characterization methods

2.4.1 Microstructure of the powders and coatings

The morphologies and microstructures of the powders and the coatings were observed using an optical microscope from Nikon (Japan) and a scanning electron microscope equipped with an energy-dispersive spectroscopy (EDS) unit (SEM JEOL-5800LV, Japan). For the cross-sectional analysis of the powder particles and coatings, the samples were prepared using standard metallographic procedures with a final polishing using a 0.04 μm silica dispersion.

2.4.2 Online diagnosis of in-flight particles

In the past twenty years, important developments in process diagnostic have been performed to monitor the behavior of on-line particles [2, 3]. One of these systems is the DPV 2000 system (Tecnar, Canada) allows the on-line measurement of the velocity, surface temperature and diameter of single particles. In this work, a DPV 2000 diagnostic system was used to monitor flying particles. This device is based on the detection of the thermal emission of hot particles passing through a measurement space. The corresponding signals are analyzed in terms of diameter, velocity and temperature of the flying particles. Measurements are performed in the centerline of the plume at a point located at the standoff distance selected for the coating deposition. A statistical processing of the acquired data enables determining the

average and standard deviation of all particles detected by the diagnostic system. The number of detected particles exceeds 1000 for each measurement run. The measured particle velocity and temperature reported are the average values of the detected particles.

2.4.3 Porosity and surface roughness of the coatings

The porosity of as-deposited coatings was determined by using the ImageJ software (ImageJ, NIH, Bethesda, Md.). Cross-sectional SEM images were taken with the magnification of 150 at different points of the coatings to measure its porosity. At least 10 measurements were done on each specimen to ensure data repeatability.

The surface roughness (Ra) of the coatings was measured using a surface roughness tester (SJ-210 SERIES, Mitutoyo, Japan). Each coating was measured ten times in different regions; The average value of these results was taken as the final surface roughness of the coating.

2.4.4 Phase composition of the powders and the coatings

In order to identify the phase transformations during the HVOF and HVOAF processes, the as-sprayed coatings as well as the feedstock powders were examined by an X-ray diffractometer (Siemens D5000, Germany) with Co (λ=1.78897 Å) using a source current of 40 mA, voltage of 35 kV and a scan step of 0.02°.

2.4.5 Mechanical properties of the coatings

Microhardness measurements were performed on the transverse section of the coatings under a load of 300g for 15 s using a Vickers microhardness tester (Leitz-Wetzlar, Germany). At least 10 measurements were done on each specimen to ensure data repeatability. The nano-hardness (HIT) and the elastic modulus (EIT) of the coatings were measured by a Nano-indentation tester (CSM, Switzerland) with a load of 10 mN, a loading rate of 20 mN/min, an unloading rate of 20 mN/ min and a dwelling time of 10 s. Before the measurements, the top surface of coatings was mechanically polished for improving the planeness. Ten times of repeated measurements were made at least, and the average values were recorded.

The measurement of the bonding strength of as-sprayed coatings was carried out using the Escotest-50 pull off adhesion strength tester, which is in accordance with the ASTM Standard C-633. A commercially available glue with a nominal strength of 68 MPa was employed. The glued samples were solidified in an oven at 185 °C for two hours. To prevent the shear forces, the two samples must be kept coaxial. In order to ensure consistency, three tests were conducted on each coating under identical conditions. The average value was used to calculate the coating bonding strength.

The fracture toughness of the coatings was characterized by means of the indentation method using Vickers indenters (Amsler Otto Wolpert-Werke, Germany). The indentation was carried out on the transverse section of the coatings in the mid-plane region to minimize the edge and interface effects. A load of 5 kg was applied for a dwell time of 15 s at a fixed rate. Optical microscopy (VHX-7000, Japan) was used to inspect the indentations for studying the propagation of corner cracks as well as measuring the length of the cracks. The fracture toughness (Kc) was evaluated using the well-established formulation established by Evans and Wilshaw [4], as given below:

$$K_c = 0.079(P/a^{\frac{3}{2}})log\ (4.5a/c) \quad (1)$$

where P (N) is the load applied to the indenter, a (m) and c (m) correspond to the length of the indentation half-diagonal and the length of the crack from the centre of the indent, respectively. The recommended “c/a” ratio in this formula is in the range of 0.6–4.5. Averages of five readings along with the standard deviations are reported.

2.4.6 Erosion wear tests

The solid particle erosion tests were conducted at room temperature with a homemade device, as shown in Fig. 2.7, according to the erosion test standard ASTM G76-2013 [5]. The erodent used for this study was an alumina powder with an average particle size of 250 μm. Fig. 2.8 exhibits a flaky and angular morphology of these particles. The settings of the erosion parameters will be detailed in the following chapters. After the test, each sample was removed, cleaned in acetone, dried and weighed to determine the weight loss on an electronic weight

balance with an accuracy of 0.0001 g. Three repeats were performed to secure the repeatability of the test and the average values were reported. The erosion rate (g/g) was calculated as the ratio of the mass loss of the coating (in g) to the mass of the erodent particles (in g).

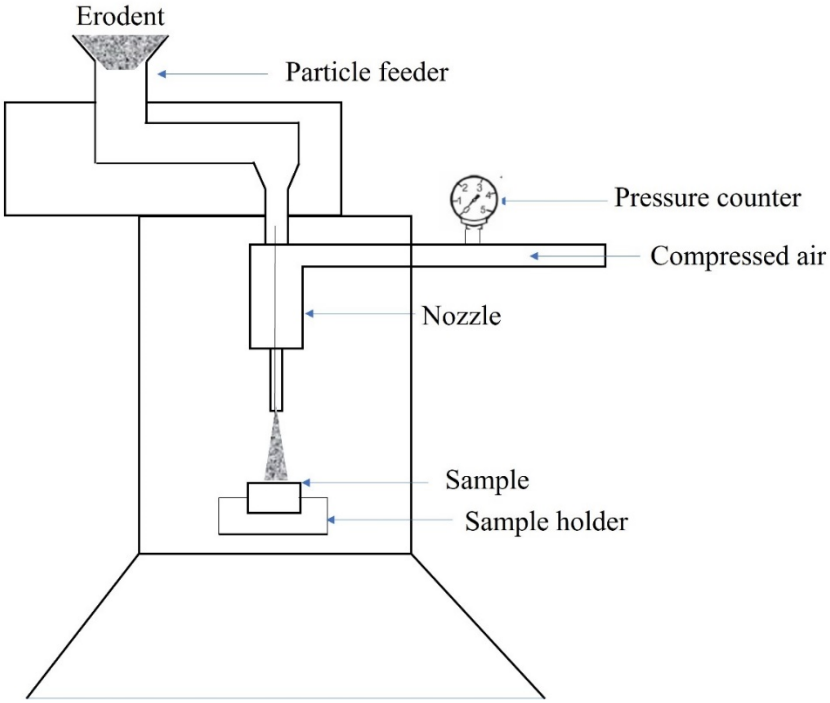

Fig. 2.7 Schematic of the air jet erosion tester

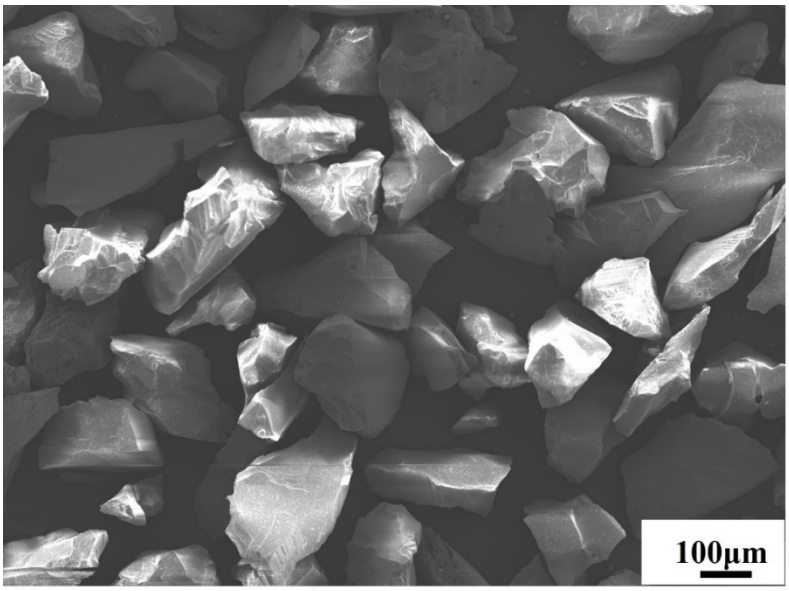

Fig. 2.8 Morphology of the alumina erodent

2.4.7 Sliding wear tests

The sliding wear experiments were carried out in an ambient setting (temperature: 20–25 °C, humidity: 40–60%) using a ball-on-disc tribometer (Switzerland). Prior to the experiments, samples were polished to a surface roughness below 0.05 μm using a normal preparation process and a further polishing with 0.04 μm silica suspension. The counterpart material was a 6 mm diameter Al_2O_3 ball that had been washed with ethanol before the experiments. For the Cr_3C_2-NiCr coatings, each test was carried out without lubrication over a sliding distance l of 5000 m and with a load p of 5 N. A linear sliding speed of 10 cm/s was achieved, with a rotation radius r of 7 mm. For the NiCoCrAlYTa coatings, each test was also carried out without lubrication over a sliding distance l of 350 m and with a load p of 5 N. A linear sliding speed of 10 cm/s was used, with a rotation radius r of 5 mm. The coefficient of friction (COF) was automatically recorded by the computer. After the friction test, the wear scars were characterized by SEM and EDS. The cross-sectional areas of the worn tracks were measured using an Altisurf 500 profilometer (France). The worn loss of the samples was determined by the product of the cross-sectional areas S (mm^2) and the circular length $2\pi r$ (mm) of the worn tracks. The wear rate W_r ($mm^3 \times N^{-1} \times m^{-1}$) was defined by Eq. (2), expressed as the wear volume loss (mm^3) divided by the normal load p (N) and the total sliding distance l (m).

$$W_r = \frac{2\pi r \times S}{p \times l} \quad (2)$$

2.4.8 Electrochemical measurements

The corrosion behavior of the as-sprayed coatings was assessed using an EC-Lab V10.12 electrochemical system (BioLogic, France). Potentiodynamic polarization measurements (LSV) were performed in 0.1 M HCl solutions using a three-electrode electrolyte cell with a saturated calomel electrode (SCE) as the reference and a platinum as the counter electrode. Prior to each corrosion experiment, specimens were mounted in epoxy resin with an effective square area of about 1 cm^2 being exposed to the corrosive medium. All the samples were mechanically polished till the use of 0.04 μm silica suspension. After the samples were maintained for 30

min in the testing cell with the HCl solution, potentiodynamic polarization curves were recorded by applying a potential voltage from -0.9 V to +0 V vs. open circuit potential (OCP) at a scan rate of 1 mV/s. Results were analyzed to obtain the corrosion potential (Ecorr) and corrosion current density (icorr).

References

[1] Q. Wang, Z. Chen, L. Li, G. Yang, The parameters optimization and abrasion wear mechanism of liquid fuel HVOF sprayed bimodal WC–12Co coating, Surface and coatings technology 206(8-9) (2012) 2233-2241.

[2] J.R. Fincke, W.D. Swank, R.L. Bewley, D.C. Haggard, M. Gevelber, D. Wroblewski, Diagnostics and control in the thermal spray process, Surface and Coatings Technology 146 (2001) 537-543.

[3] W.-C. Lih, S. Yang, C. Su, S. Huang, I. Hsu, M. Leu, Effects of process parameters on molten particle speed and surface temperature and the properties of HVOF CrC/NiCr coatings, Surface and Coatings Technology 133 (2000) 54-60.

[4] A. Evans, T.R. Wilshaw, Quasi-static solid particle damage in brittle solids—I. Observations analysis and implications, Acta Metallurgica 24(10) (1976) 939-956.

[5] X. Zhang, F. Li, Y. Li, Q. Lu, Z. Li, H. Lu, X. Ran, X. Qi, Comparison on multi-angle erosion behavior and mechanism of Cr3C2-NiCr coatings sprayed by SPS and HVOF, Surface and Coatings Technology 403 (2020) 126366.

Chapter 3 Relationships between in-flight particle characteristics and properties of the WC-10Co-4Cr coatings prepared with the Ethanol-Fueled e-Gun HVOF device

3.1 Introduction

During the HVOF coating process, the velocity and temperature of in-flight particles and the corresponding coating properties are affected not only by the properties of the fed powder but also significantly by the selected spray process and spray parameters. The properties of the original powder particles in terms of chemical composition, morphology, and size distribution on one hand and the operating parameters on another hand, such as the standoff distance, powder particle feed rate, incidence angle, gun geometry and substrate temperature are the parameters which control the microstructures of the coatings, which in turn affect their properties [1, 2]. From an optimization perspective, other factors including the fuel type, the flow rate of fuel and oxygen have significant influence on the control of coating properties. Many optimizations have been done on HVOF spraying systems, such as the DJ2700 and JK3500 devices using propene or propane as fuels [3-5], and JP-5000 / 8000 spray system using kerosene as fuel [6, 7]. Picas et al. [8] studied the effect of the oxygen/fuel ratio on the in-flight particle parameters and properties of the resulting HVOF WC-CoCr coatings, and found that the kerosene–oxygen mixtures resulted in a greater velocity and a lower temperature of the particles than the hydrogen–oxygen ones. Hong et al. [9] employed a Taguchi L9 orthogonal array method to study the effect of the oxygen and kerosene flow rates, and the spray distance on the hardness of HVOF sprayed nanostructured WC-10Co-4Cr coatings. They identified the kerosene flow rate as the most influencing parameter. Murugan et al. [10] optimized HVOF the spray process parameters to attain minimum porosity and maximum hardness in WC–10Co–4Cr coatings. They found that the oxygen flow rate has a stronger impact on coating porosity and hardness than the other HVOF spray parameters. Praveen et al. [2] investigated the optimization and erosion wear response of NiCrSiB/WC–Co HVOF coatings using the Taguchi method as well and identified the standoff distance and powder feed rate as the most determining parameters on the erosion wear loss. These authors further studied the erosion properties and mechanism of the coating deposited under the optimal set of spray parameters.

In this chapter, we have employed the new liquid fuel HVOF torch, which uses ethanol as

fuel. It was developed by the Flame Spray Technologies Company in the Netherlands. The choice of ethanol as a liquid fuel has distinctive advantages over kerosene, such as being more environmentally sustainable (in case of bioethanol having non-fossil origin) and less polluting (less emission of soot particles). By acquiring and exploiting the physical data relating to the velocity and temperature of in-flight particles during coating experiments, a deeper understanding of the process can be achieved, enabling the optimization of the spray parameters to reach the required coating characteristics. To the best of the author's knowledge, there is however no report of the effects of such spray data in the case of ethanol-fueled torches. In view of this gap in the existing literature, it seemed of great interest to tackle this task, which is: (i) to investigate the effect of the spraying parameters on the velocity and temperature of in-flight particles and (ii) to assess the resulting impacts on the microstructure and mechanical properties of the deposited coatings. Another motivation to carry out this study was the interest of shifting towards an alternative HVOF fuel able to reduce the combustion emissions, especially those of carbon dioxide and make thermal spray "greener". The aim of this work is therefore to investigate the influence of different oxygen/fuel ratios on the evolution of the velocity and temperature of in-flight particles and correlate these data with the properties of WC-CoCr coatings deposited with the eGun HVOF device. The investigated coatings properties were their phase composition, microstructure, porosity level, microhardness and fracture toughness.

3.2 Preparation conditions of the coatings

In this chapter, the eGun HVOF system was employed to prepare WC–10Co4Cr coatings. The standoff distance from the nozzle tip to the substrate surface was fixed at 270 mm. The transverse scanning speed (relative to the substrate) of the spray gun was 0.5 m/s, which was achieved through programming an ABB robot. Nitrogen (8 NL/min) was used as the powder carrier gas for all experiments. The powder feed rate was kept constant at 59g/min during the experimentation. Specimens were cooled during and after spraying with compressed air jets. The thickness of all the coatings was kept in the range of 250-300mm.

A main spray parameter that was investigated is the Oxygen/Fuel ratio which determines the stoichiometry factor. Here the stoichiometry factor ("SF") is defined based on the following equation:

$$C_2H_6O + (3 * SF)\ O_2 \rightarrow 2CO_2 + 3H_2O + 3 * (SF - 1)\ O_2 \quad (1)$$

where:

- SF < 1 corresponds to "rich" combustion conditions, i.e. with insufficient oxygen
- SF = 1 corresponds to a stoichiometric combustion
- SF > 1 corresponds to lean and clean combustion conditions with some oxygen excess

The experimental parameters and their values employed in the study were determined in the light of preliminary experiments and are given in Table 3.1. These parameters were selected in order to explore diverse gas/fuel flow rates and different stoichiometric factors with the view to evaluating their influence on the coating properties. To assess the characteristics of particles in flight, a DPV 2000 diagnostic system was used. Measurements were performed in the centerline of the plume at the standoff distance of 270 mm from the nozzle exit.

Table 3.1 The experimental spray parameters and corresponding properties of the WC-10Co4Cr coatings

Test	C_2H_6O /slph	O_2 /slpm	SF	V /[m/s]	T /℃	Porosity /%	Microhard. /HV0.3	Fracture toughness /(MPam$^{1/2}$)
E1	22	430	1.00	576±24	1641±72	1.47±0.16	1067.1±132.2	4.97±0.43
E2	22	460	1.08	588±24	1649±65	1.13±0.07	1101.7±75.3	5.63±0.9
E3	22	490	1.15	596±23	1669±67	1.22±0.11	1219.7±121.5	5.57±1.41
E4	22	520	1.22	606±25	1654±68	0.90±0.28	1220.2±162.3	8.15±0.7
E5	24	520	1.13	618±27	1670±80	1.49±0.03	1212.0±93.4	3.66±0.48
E6	26	520	1.06	637±27	1715±77	1.10±0.09	1204.0±144.8	5.56±1.21
E7	28	520	0.96	640±22	1705±75	0.94±0.09	1236.8±66.8	6.16±1.06

3.3 Characteristics of in-flight particles

During the thermal spray process, the speed and surface temperature of the in-flight particles are two key factors affecting the quality of the sprayed coating. The coating deposited by molten particles through higher kinetic energy and adequate surface temperature is expected

to be denser and harder. Using the results of the different series of sprays we have performed with the eGun system, we have been able to elaborate a correlation map between the temperature and the velocity of the in-flight particles. The results are presented in the Fig. 3.1. The flow rate of ethanol varied from 22 to 28 l/h, and that of oxygen ranged from 430 to 520 l/min, resulting in different stoichiometric ratios, which are distributed between 0.96 and 1.22. The velocity and temperature of the particles are found to lie between 550-700 m/s and 1600-1700 °C, respectively. Zhao et al. [3] studied the characteristics of flying particles of WC-CoCr (10-45µm) powder sprayed by DJ 2600 (fueled with hydrogen and oxygen) and using the DPV-2000 device; the particles velocity and temperature were distributed between 400-500 m/s and 1900-2200°C, respectively. The in-flight particle characteristics of WC-10Co-4Cr (10-38µm) powder sprayed by Wokajet-400 (fueled with kerosene and oxygen) and measured by the Accuraspray-g3 system were also reported. The particles velocity produced by these kerosene-oxygen mixtures was usually in the range of 700-800 m/s, but their temperature generally exceeded 1800 °C [8]. As far as ethanol-oxygen mixtures are concerned, they generally produce a similar particle velocity, but a lower temperature compared with kerosene-oxygen mixtures and hydrogen-oxygen mixtures.

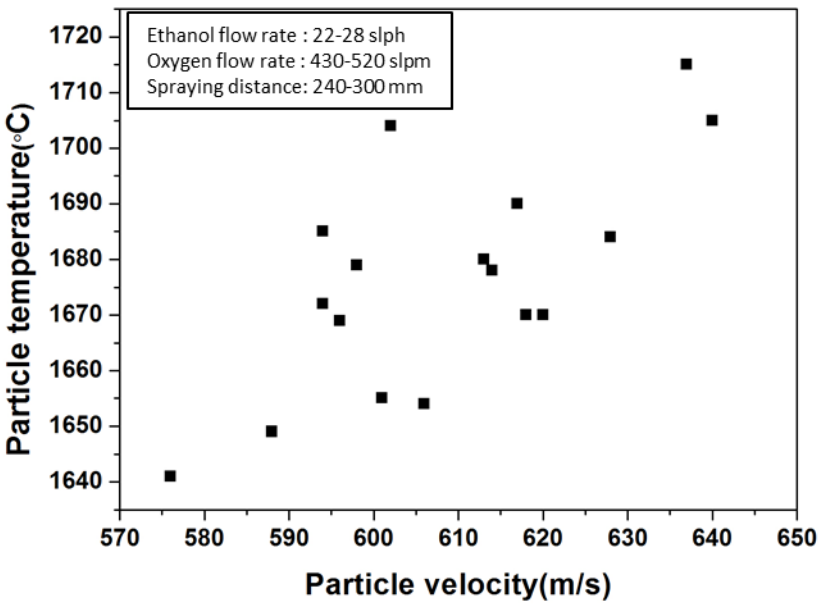

Fig. 3.1 Evolution of particle temperatures and velocities for ethanol-oxygen mixtures

Fig. 3.2 shows a more detailed parametric study relating to the variation of the oxygen/fuel ratio when using the eGun torch. Indeed, to evaluate the effect of the oxygen flow rate on the particle characteristics and coating performances, a series of experiments was conducted in which the oxygen flow rate was varied while keeping the ethanol flow rate unchanged. Fig. 3.2(a) shows the average particle velocity and temperature in function of the oxygen flow rate at a constant ethanol level of 22 l/h. One can see that both the particle velocity and temperature initially increase as the oxygen flow rates passes from 430 to 520 l/min. However, a decrease in particle temperature is observed from a certain oxygen flow rate value, while the particle velocity continues to increase. The particle velocity goes from 576 to 606 m/s, corresponding to a 5.2% increase rate. On the one hand, an increase in the total gas flow increases the combustion chamber pressure. A higher chamber pressure leads to an increased particle velocity, which is attributed to a growing momentum transfer from the gas phase to the particles and possibly to the stronger gas viscosity [1]. Consequently, the particle velocity exhibits a quasi-linear increase against the oxygen flow rate. On the other hand, taking into account the standard deviation of these measured values, it can be said that the particles temperature changes relatively little over the varied range of O_2 flow rates. However, a certain change trend can still be observed since the increase of the O_2 flow rate changes the characteristics of the combustion gas. The particles temperature generally depends mainly on that of the flame and on the residence time within the hot jet. Moreover, the oxygen/fuel ratio determines the stoichiometry of the combustion, which plays a very important role in controlling the jet temperature and consequently the underheated or overheated status of the particles with respect to their melting point. The individual C_2H_6O and O_2 flow rates and the corresponding stoichiometry data have been listed in Table 1 below. When the oxygen content is stoichiometric, i.e. sufficient to completely burn ethanol but not in excess, the flame temperature theoretically reaches a maximum. For higher oxygen flow rates, there is an excess of oxygen that then acts as a cooling gas and consequently decreases the flame temperature. Nevertheless, liquid fuel HVOF guns are typically operated with excess oxygen to prevent toxic emissions of unburned compounds

(VOCs and PAHs) and potentially unburned carbonaceous deposits in the combustion chamber. In addition, the increase in the total gas flow elevates the particles velocity, thereby reducing the residence time of particles inside the flame, thus reducing the heat transfer between the gas phase and the particles. This results in the decrease of the particle temperature. For oxygen flow rates above 490 slpm, the temperature of the in-flight particles decreases due to the shorter interaction time with the hot jet.

This interpretation also accounts for the evolution of the particle temperature and velocity in Fig. 3.2(b). At a constant O_2 flow rate (520 slpm), when the C_2H_6O flow rate was increased from 22 l/h to 28 l/h, the velocity of the particles continued to increase while their temperature initially increased, reaching a peak value, and then decreased. Although the total flow rate does increase under the conditions of Fig. 3.2(b), the particle velocity is higher, and the residence time in the hot jet is shorter, but in this case, the flame temperature (and not the residence time) plays a dominant role. The oxygen/fuel ratio determines the stoichiometric ratio of combustion and therefore controls the temperature of the jet, thereby affecting the temperature of the flying particles.

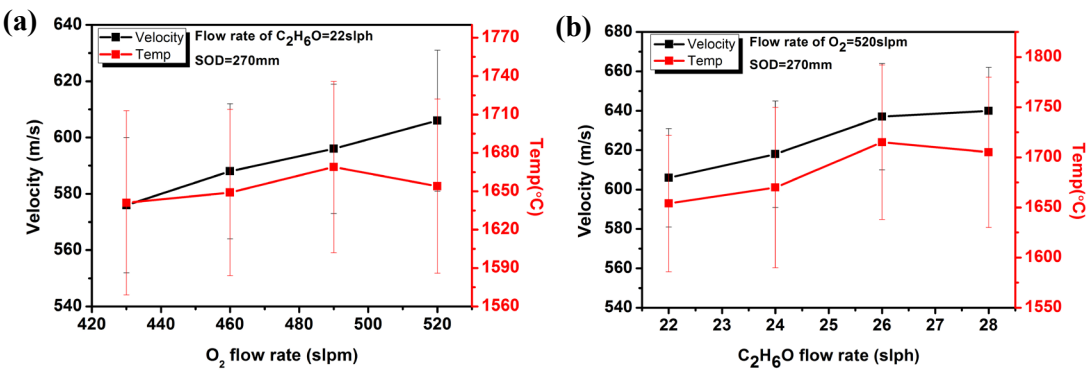

Fig. 3.2 Evolution of particles temperatures and velocities: (a) vs. different O_2 flow rates; (b) vs. different C_2H_6O flow rates.

3.4 Phase composition and microstructure of the coatings

The X-Ray diffraction patterns of the coating powder and those of the HVOF-sprayed WC–10Co4Cr coatings deposited under the different spray parameters are grouped in Fig. 3.3.

It is observed that the diffraction peaks obtained for the seven groups of coatings sprayed with different parameters are almost similar to the peaks of the powder, although all coatings show several low intensity W_2C peaks. There is no significant difference in the phase composition of the seven sets of coatings, which is predominately made by WC and a small amount of W_2C. This result is consistent with other researchers reports on such coatings [11]. The origin of the detected W_2C phase may be attributed to the decarburization of a part of the WC particles which takes place in the hot flame. It is well-known that the formation of W_2C is largely dependent on the heating degree of the parent powder [12, 13]. Although the ethanol-oxygen flames develop lower temperatures than kerosene-oxygen flames, there is still a small extent of decarburization for WC–10Co4Cr coatings.

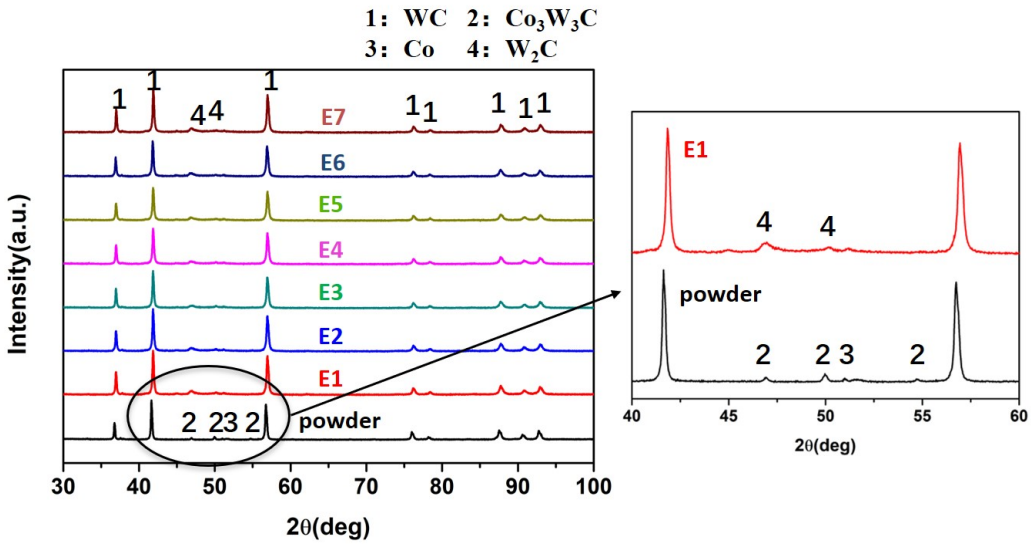

Fig. 3.3 XRD patterns of the WC–10Co–4Cr feedstock powder and the coatings with different spraying parameters.

Fig. 3.4 shows the typical cross-sectional microstructure of the sprayed WC–10Co–4Cr coatings after polishing. There is no significant difference in the microstructures of the different coatings obtained over the range of the spray parameters. Overall, it can be stated that the coating is very dense and well-bonded to the substrate, and both coarse and fine WC grains are uniformly distributed in the coating, as shown in Fig. 3.4 (a) and (b). The higher magnification BSE image gives access to some details of the microstructure of the coating, as shown in Fig. 3.5(a). It is reminded that the typical splat-like microstructures with dark and light contrast

matrix layers correspond to regions of lower and higher average atomic number and density, respectively. The darker areas correspond to the matrix of Co and Cr, and the brighter regions to the carbide particles. The EDX analyses of these two areas are shown in Fig. 3.5(b). Obviously, different local tungsten concentrations are the main reason for the different contrast levels of the matrix. Most of the WC particles are blocky and angular, while in brighter areas, the tungsten carbide particles have a rounder appearance and are often partially or completely enclosed within bright contrast shells of another phase. This may be due to the full melting of the Co and Cr binder phase and the dissolution of some WC in the Co and Cr matrix. Similar morphologies have also been found in many HVOF sprayed WC–10Co–4Cr coatings [14, 15]. Therefore, the shell around the WC particles may contain the W_2C phase that has been identified by XRD.

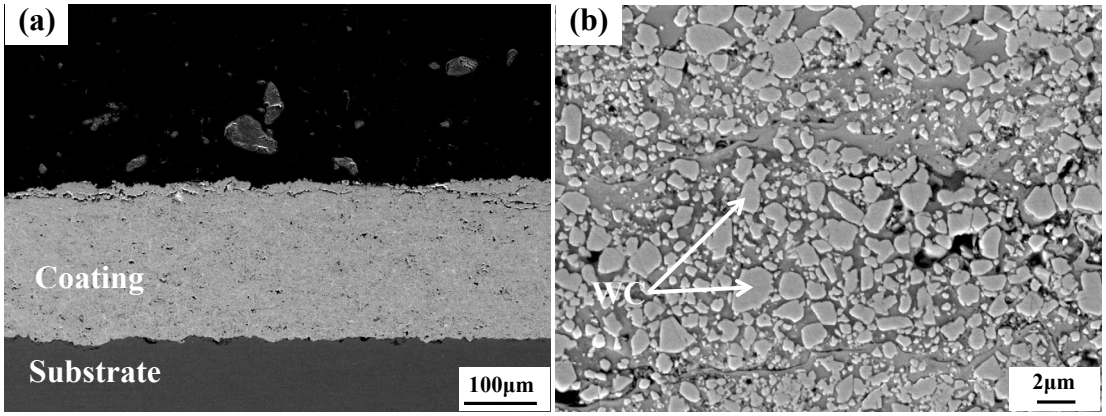

Fig. 3.4 Cross-sectional SEM micrographs of coated samples: (a) overview image; (b) magnified image.

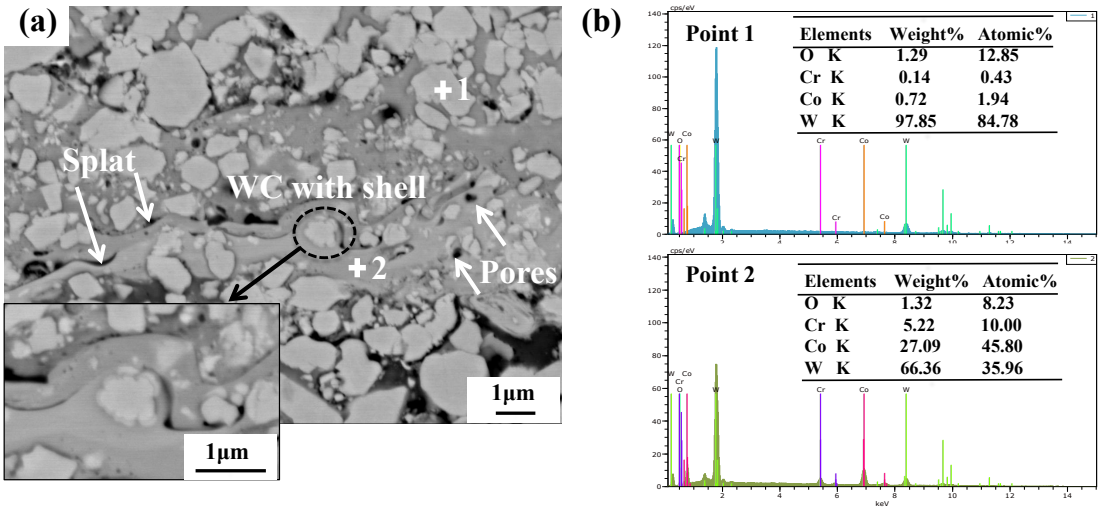

Fig. 3.5 Higher magnification BSE image showing the details of the microstructure of the coating: (a) BSE image; (b) EDS analysis results of point 1 and 2 in the coating.

3.5 Evaluation of the porosity and microhardness

Table 3.1 lists the porosity and microhardness data of the WC–10Co–4Cr coatings obtained with different spraying parameters, as well as their standard deviations. At a constant C_2H_6O level (22 slph), the O_2 flow rate increases from 430 slpm to 520 slpm, and one sees that the porosity of the coatings decreases from 1.47% to 0.90%, as shown in Fig. 3.6(a). When the oxygen flow rate is fixed at 520 slpm, the porosity of the coatings initially increases and then decreases with the increase of the ethanol flow rate (from 22 to 28 slph), as shown in Fig. 3.6(b). The formation of pores is a complex process that involves a series of effects, including the degree of melting in the flame stream, deformations, diffusion, impact, solidification of powder particles and interactions with previously deposited splats. It is well known that the general level of porosity is related to the temperature and velocity of the flying particles during the spraying process. Fig. 3.7(a) shows the following general trend: the higher the temperature, the lower the porosity. On can also deduce from Fig. 3.7(b) that the higher the particle velocity, the lower the porosity, except for the set of parameters E5, which looks to be an outlier. The combination of high temperature and velocity may lead to the melting and the deformation of the flying particles which, upon impact on the previous deposited layers, are likely to fill the

pores and defects of the former layer, resulting in a lower porosity level.

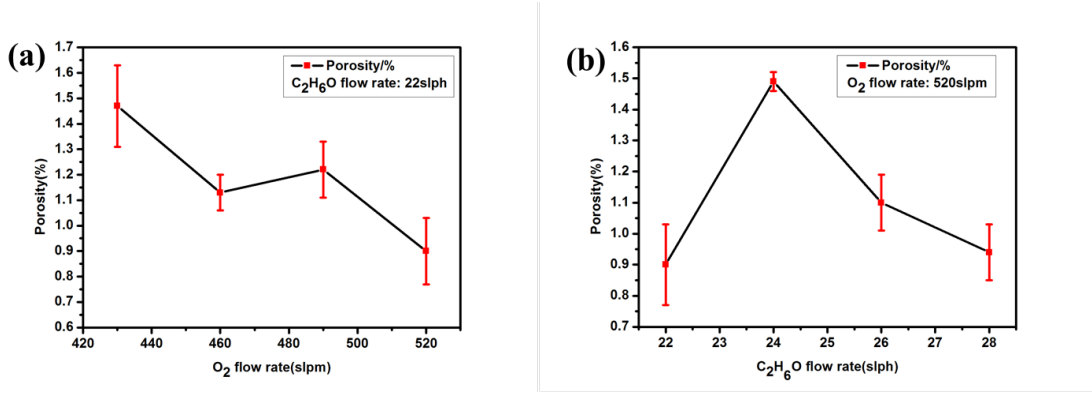

Fig. 3.6 Evolution of the porosity of coatings: (a) vs. different O_2 flow rates; (b) vs. different C_2H_6O flow rates.

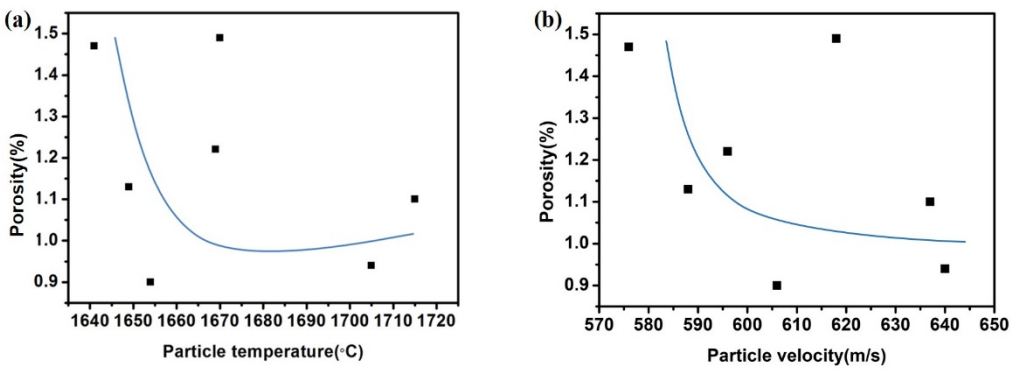

Fig. 3.7 Evolution of the porosity of coatings: (a) vs. particle temperature; (b) vs. particle velocity.

When the ethanol flow rate is kept at 22 slph and the O_2 flow rate gets increased from 430 to 520 slpm, a slight increase in the microhardness of the coating (from 1067.1 to 1220.2) is observed in Fig. 3.8(a). Nevertheless, taking into account the standard deviation, the microhardness of the coatings tends to be stable when the oxygen flow rate is fixed at 520 slpm and the ethanol flow rate gets increased, as shown in Fig. 3.8(b). It seems therefore that the ethanol flow rate has little effect on the microhardness of the coatings at high oxygen flow rates, which may be attributed to invariable characteristics of the flying particles. The influence of the particle temperature and the particle velocity on the coating microhardness can be seen in Fig. 3.9. One observes that a higher particle temperature results in a relatively higher

microhardness (See Fig. 3.9(a)). This may be attributed to the higher particle temperature, which leads to lower porosity and thus higher microhardness. The microhardness of the coatings also follows a similar trend with the particle velocity. As shown in Fig. 3.9(b), a relatively high particle velocity leads to a higher microhardness. In general, the microhardness of coatings measured at 300 gf is related to interlamellar cohesion and the intra-lamellar characteristics (decarburization, phase composition). However, the microhardness may reflect here the change in interlamellar cohesion due to almost the same intra-lamellar characteristics of the seven groups of coatings, as described in section 3.4. Probably, interlamellar cohesion was enhanced through higher particles velocities at higher total gas flow rates.

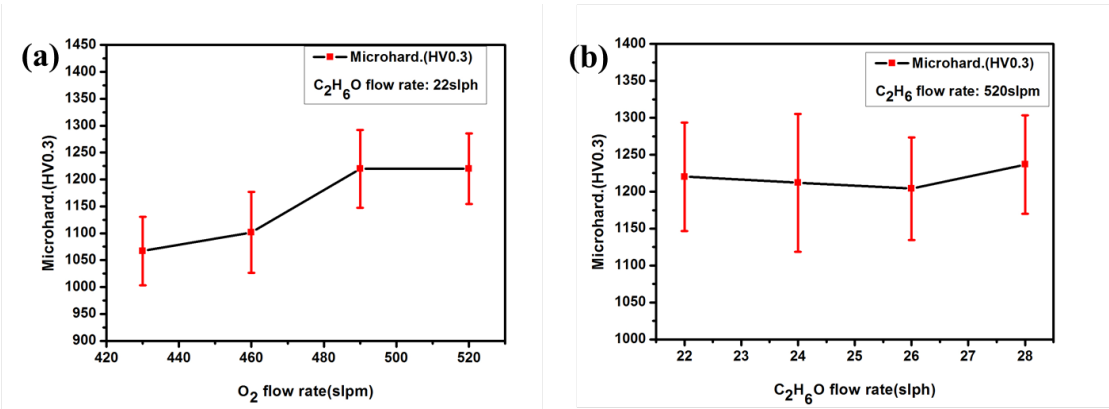

Fig. 3.8 Evolution of the microhardness of the coatings: (a) vs. different O_2 flow rates; (b) vs. different C_2H_6O flow rates.

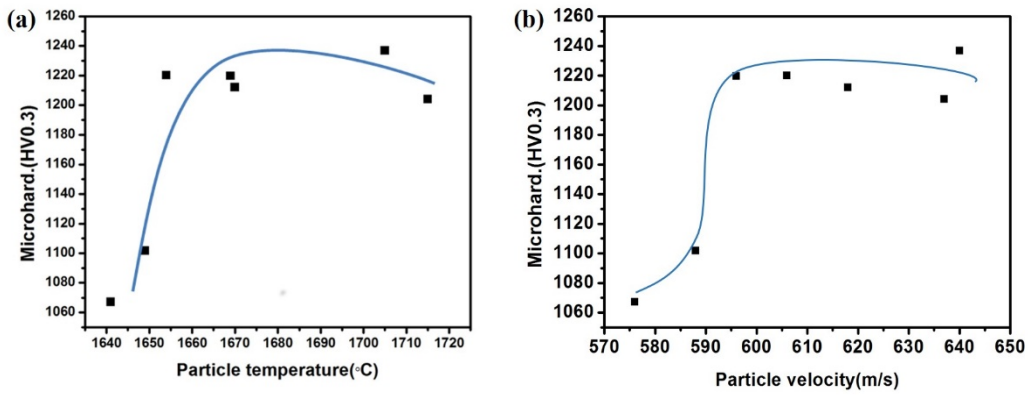

Fig. 3.9 Evolution of the microhardness of the coatings: (a) vs. particle temperature; (b) vs. particle velocity.

3.6 Fracture toughness

In order to have high wear resistance, not only high hardness but also high fracture toughness is required. Fig. 3.10 shows the typical Vickers indent micrographs obtained on the cross sections of the coating layers sprayed with different parameters. Cracks were found in all seven coatings after the indentation tests, but with different lengths. One sees that the cracks mainly propagate into the direction parallel to the interface between the coating and substrate. Cantera et al. [16] observed that, for sintered materials, the fracture toughness was isotropic but, for thermally sprayed materials, the fracture toughness was anisotropic. The fracture toughness perpendicular to the coating/substrate interface is significantly higher than that in the parallel direction. The propagation of the cracks is much easier when it occurs parallel to the coating/substrate interface rather than transversely to it, which may result from the elongated nature of the splats and the residual stress fields present.

From the measurement of the length of the cracks shown in Fig. 3.10, the fracture toughness was determined by the well-established formulation established by Evans and Wilshaw. Similar results to those obtained for the hardness were found and are presented in Table 3.1. When the ethanol flow rate was maintained at 22 slph and the O_2 flow rate increased from 430 slpm to 520 slpm, a significant increase in the fracture toughness of the coating was observed (from 4.94 to 8.15) in Fig. 3.11(a). However, when the oxygen flow rate was kept constant at 520 slpm, the fracture toughness first decreased and then increased with the ethanol flow rate, as shown in Fig. 3.11 (b). Overall, according to these experimental results, it can be inferred that the use of different spraying parameters has a significant effect on the fracture toughness of the coating. WC-Co-Cr deposits are the most common cemented carbide coatings used today; they combine the hard WC particles with the ductile Co and Cr matrix, and the evolution of their fracture toughness is therefore more complicated. It can be seen from the Fig. 3.11 that the fracture toughness of the coatings changes in a way inverse to porosity. The higher the porosity, the lower the fracture toughness. This may be tied with the fact the pores of the coating are preferential sites for crack occurrence and growth.

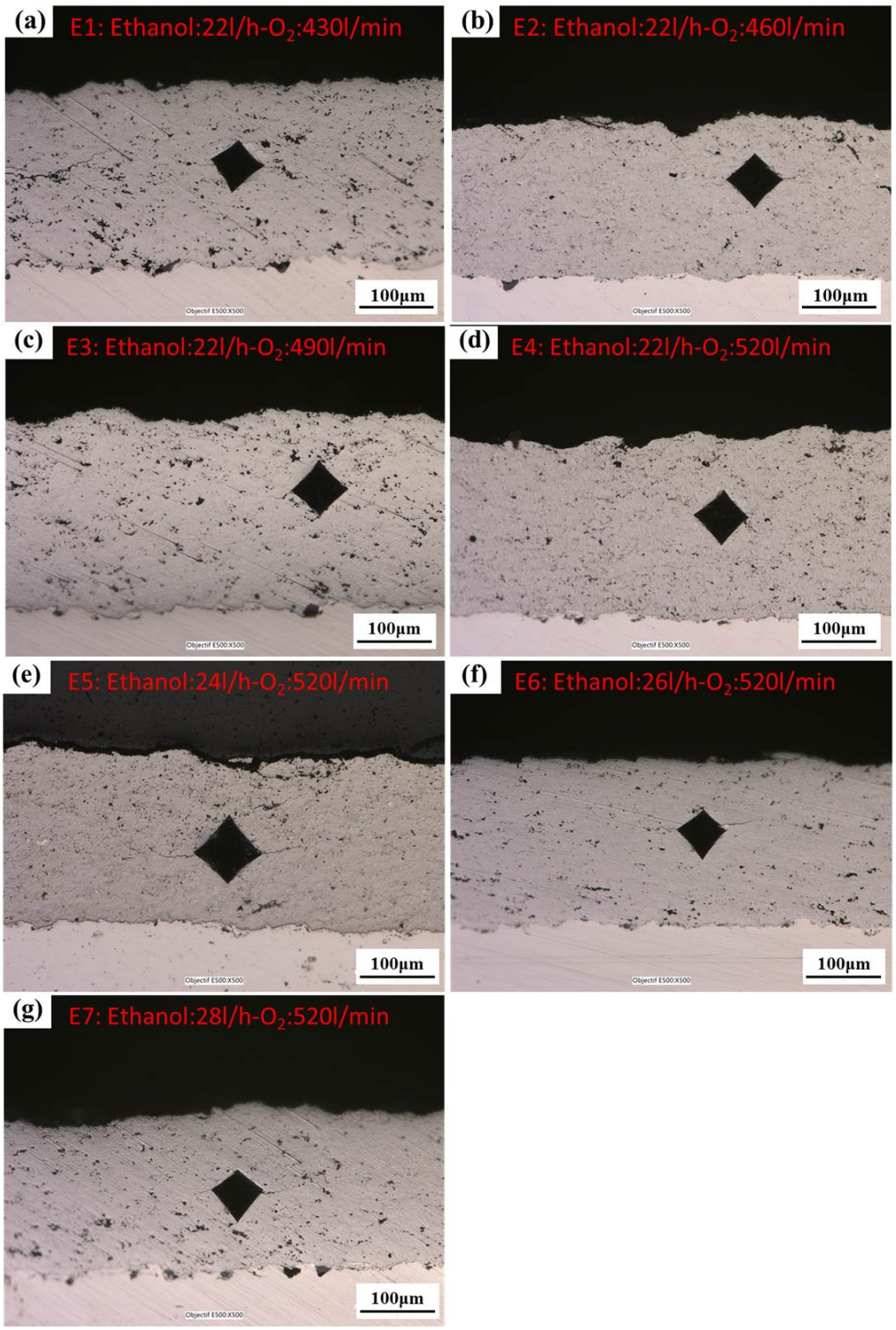

Fig. 3.10 Typical indent micrographs on the cross-sections of coating layers sprayed with different parameters. (a) E1: Ethanol:22l/h-O_2:430l/min; (b) E2: Ethanol:22l/h-O_2:460l/min; (c) E3: Ethanol:22l/h-O_2:490l/min; (d) E4: Ethanol:22l/h-O_2:520l/min; (e) E5: Ethanol:24l/h-O_2:520l/min; (f) E6: Ethanol:26l/h-O_2:520l/min; (g) E7: Ethanol:28l/h-O_2:520l/min.

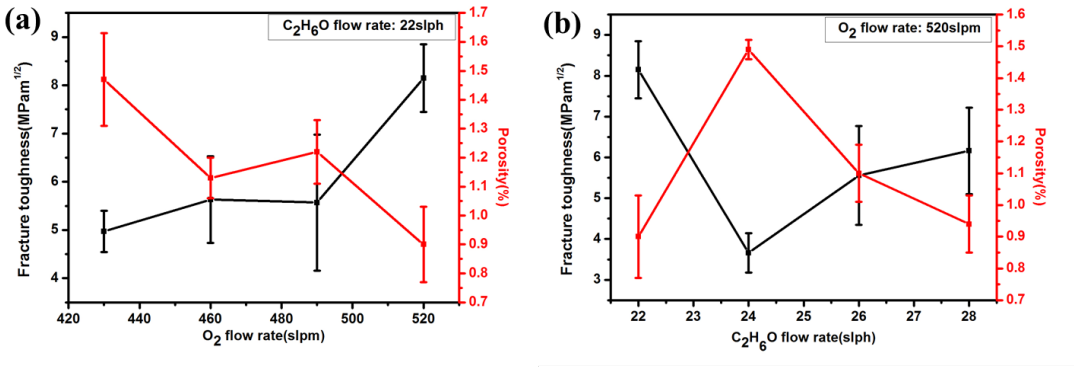

Fig. 3.11 Evolution of the fracture toughness with the porosity of the coatings: (a) vs. different O_2 flow rates; (b) vs. different C_2H_6O flow rates.

3.7 Conclusions

In this chapter, we have investigated the performances of the ethanol fueled HVOF device. To that end, we have applied it to the spraying of a WC-CoCr powder, and we have studied the influence of the spray parameters on (i) the in-flight temperature and velocity determined by on-line particle monitoring, and (ii) the performances of the resulting coatings. The conclusions obtained can be summarized as follows:

1. Compared to kerosene-oxygen and hydrogen-oxygen mixtures, ethanol-oxygen mixtures typically result in lower temperatures of the particles.
2. The oxygen flow rate affects the combustion reaction, but an excess of oxygen will cool the flame and decrease the particle temperature. Furthermore, the increase in total gas flow rate increases the particle velocity, reducing the residence time of the particle into the flame, resulting in a decrease in the particle temperature.
3. The degree of porosity tends to decrease with the increase of the particle temperature and velocity. Our experimental results also indicate that the coating microhardness tends to increase with the particle temperature. The fracture toughness of the coating changes to some extent in the opposite way to the porosity.
4. After cautiously considering the performances of the various coating performances, it is possible to identify the values of the ethanol and oxygen flow rates that generate the best

coating performances; these values are 22 slph for ethanol and 520 slph for oxygen.

References

[1] X. Guo, M.-P. Planche, J. Chen, H. Liao, Relationships between in-flight particle characteristics and properties of HVOF sprayed WC-CoCr coatings, Journal of Materials Processing Technology 214(2) (2014) 456-461.

[2] A.S. Praveen, J. Sarangan, S. Suresh, B. Channabasappa, Optimization and erosion wear response of NiCrSiB/WC–Co HVOF coating using Taguchi method, Ceramics International 42(1) (2016) 1094-1104.

[3] L. Zhao, M. Maurer, F. Fischer, E. Lugscheider, Study of HVOF spraying of WC–CoCr using on-line particle monitoring, Surface and Coatings Technology 185(2-3) (2004) 160-165.

[4] W. Fang, T. Cho, J. Yoon, K. Song, S. Hur, S. Youn, H. Chun, Processing optimization, surface properties and wear behavior of HVOF spraying WC–CrC–Ni coating, Journal of materials processing technology 209(7) (2009) 3561-3567.

[5] Y. Qiao, T.E. Fischer, A. Dent, The effects of fuel chemistry and feedstock powder structure on the mechanical and tribological properties of HVOF thermal-sprayed WC–Co coatings with very fine structures, Surface and Coatings Technology 172(1) (2003) 24-41.

[6] Q. Wang, Z. Chen, L. Li, G. Yang, The parameters optimization and abrasion wear mechanism of liquid fuel HVOF sprayed bimodal WC–12Co coating, Surface and coatings technology 206(8-9) (2012) 2233-2241.

[7] L. Qiao, Y. Wu, S. Hong, J. Cheng, Z. Wei, Influence of the high-velocity oxygen-fuel spray parameters on the porosity and corrosion resistance of iron-based amorphous coatings, Surface and Coatings Technology 366 (2019) 296-302.

[8] J.A. Picas, M. Punset, M.T. Baile, E. Martín, A. Forn, Effect of oxygen/fuel ratio on the in-flight particle parameters and properties of HVOF WC-CoCr coatings, Surface and Coatings Technology 205 (2011) S364-S368.

[9] S. Hong, Y. Wu, B. Wang, Y. Zheng, W. Gao, G. Li, High-velocity oxygen-fuel spray parameter optimization of nanostructured WC–10Co–4Cr coatings and sliding wear behavior of the optimized coating, Materials & Design 55 (2014) 286-291.

[10] K. Murugan, A. Ragupathy, V. Balasubramanian, K. Sridhar, Optimizing HVOF spray process parameters to attain minimum porosity and maximum hardness in WC–10Co–4Cr coatings, Surface and Coatings Technology 247 (2014) 90-102.

[11] T.K. Mishra, A. Kumar, S. Sinha, S. Sharma, Investigation of sliding wear behaviour of HVOF carbide coating, Materials Today: Proceedings 5(9) (2018) 19539-19546.

[12] H. Wang, Y. Li, M. Gee, H. Zhang, X. Liu, X. Song, Sliding wear resistance enhancement by controlling W2C precipitation in HVOF sprayed WC-based cermet coating, Surface and Coatings Technology 387 (2020) 125533.

[13] V. Katranidis, S. Gu, T.R. Reina, E. Alpay, B. Allcock, S. Kamnis, Experimental study of high velocity oxy-fuel sprayed WC-17Co coatings applied on complex geometries. Part B: Influence of kinematic spray parameters on microstructure, phase composition and decarburization of the coatings, Surface and Coatings Technology 328 (2017) 499-512.

[14] N. Ma, L. Guo, Z. Cheng, H. Wu, F. Ye, K. Zhang, Improvement on mechanical properties and wear resistance of HVOF sprayed WC-12Co coatings by optimizing feedstock structure, Applied Surface Science 320 (2014) 364-371.

[15] D. Stewart, P. Shipway, D. McCartney, Microstructural evolution in thermally sprayed WC–Co coatings: comparison between nanocomposite and conventional starting powders, Acta Materialia 48(7) (2000) 1593-1604.

[16] E.L. Cantera, B. Mellor, Fracture toughness and crack morphologies in eroded WC–Co–Cr thermally sprayed coatings, Materials Letters 37(4-5) (1998) 201-210.

Chapter 4 Optimization of the erosion and sliding wear resistance of Cr_3C_2-NiCr coatings prepared via the novel HVOF device

4.1 Introduction

Thermal spray coatings involving hard ceramic particles dispersed in relatively ductile and tough matrices are widely used to enhance erosion resistance [1, 2] and wear resistance in a number of applications [3, 4]. For instance, tungsten carbide based coatings sprayed by HVOF are extensively used to resist abrasion and erosion wear in the automotive and aerospace sectors for engine components, including pistons [5], shock absorber rods [6], gears [7] etc. HVOF-sprayed coatings based on chromium carbide are also frequently used to improve the erosion and wear performance of components involved in paper mills, petrochemical and power generation applications, such as calendar rolls [8], ball valves [9], impellers of pumps [10] and hydraulic turbines [11].

As shown in the previous chapter, the microstructure and the corresponding qualities of the coatings deposited by HVOF processes are greatly influenced not only by the properties of the feedstock powder employed, but also by the spraying parameters. In particular, the oxygen/fuel ratio, that determines the stoichiometric factor of the combustion in the torch, plays a very important role in controlling the temperature of the flame jet, thereby determining the microstructure, the evolution of the phase composition and the resulting mechanical properties of the coating.

In this chapter, the ethanol fueled HVOF process (called “eGun HVOF”) has been again the subject of a study devoted this time to Cr_3C_2–NiCr coatings. The dual objective of this study was (i) to optimize – by using the Taguchi method - the spray parameters (ethanol flow rate, oxygen flow rate, standoff distance, and powder feed rate) to achieve the best resistance against erosion wear of Cr_3C_2–NiCr coatings, and (ii) to determine the influence of different stoichiometry factors on the evolution of the microstructures and properties of the resulting Cr_3C_2–NiCr coatings.

4.2 Optimization and Erosion Behavior of Cr_3C_2-NiCr Coatings

4.2.1 Testing methodology and primary results

Previous studies [12, 13] have indicated that the fuel flow rate, oxygen flow rate, powder feed rate and standoff distance are the important process parameters that determine the performance of the resulting coatings. Based on some preliminary experiments, we thought appropriate to test these parameters at three distinct levels, as shown in Table 4.1. As shown in Table 4.2, a standard Taguchi L9 orthogonal array was used to reduce the number of experiments. The other spray parameters not specified in the Taguchi matrix have been set as follows: the speed of the spray gun in the horizontal direction was 500 mm/s and the step in the vertical direction was 8 mm. The powder carrier gas was nitrogen with a flow rate of 8 l/min. Specimens were cooled during and after spraying with compressed air jets. The thickness of all the coatings was adjusted in the range of 200-300 μm.

Table 4.1 Spray parameters and levels used in this experiment.

Symbol	Process parameter	Range	Level 1	Level 2	Level 3
A	Ethanol flow rate (slph)	24-32	24	28	32
B	Oxygen flow rate (slpm)	420-540	420	480	540
C	Powder feed rate (g/min)	50.7-102.7	50.7	76.7	102.7
D	Standoff distance (mm)	240-300	240	270	300

Table 4.2 Experimental results for erosion wear and corresponding S/N ratio.

Test	C_2H_6O flow rate (A)(slph)	O_2 flow rate (B)(slpm)	Powder feed rate (C)(g/min)	Distance (D)(mm)	Erosion wear loss (g)	S/N ratio
E1	24	420	50.7	240	0.0400	27.9588
E2	24	480	76.7	270	0.0453	26.88763
E3	24	540	102.7	300	0.0508	25.89128
E4	28	420	76.7	300	0.0230	32.76544
E5	28	480	102.7	240	0.0313	30.103
E6	28	540	50.7	270	0.0415	27.63904
E7	32	420	102.7	270	0.0338	29.43452
E8	32	480	50.7	300	0.0345	29.24362
E9	32	540	76.7	240	0.0390	28.17871

The detailed parameter settings of the erosion tests are listed in Table 4.3. For the optimization of the HVOF process parameters, the erosion tests were conducted at a 90° impact angle. Each test was carried out for 10 min. After the test, each sample was removed, cleaned in acetone, dried and weighed to determine the weight loss on an electronic weight balance with an accuracy of 0.0001 g. Three repeats were performed to check the repeatability of the test and the average values were reported. The erosion rate was calculated as the ratio of the coating erosion mass loss (in g) to the mass of erodent particles (in g). Besides, the erosion behavior of the optimized Cr_3C_2–NiCr coatings was also tested at 30°, 60° and 90° impact angles to analyze the erosion mechanism.

Table 4.3 Erosion test conditions of the Cr_3C_2–NiCr coatings.

Erodent material	Alumina
Average erodent size (μm)	250
Erodent velocity (m/s)	Constant
Erodent feed rate (g/min)	150
Impact angle (°)	30,60,90
Test temperature	Room temperature
Nozzle diameter (mm)	9.5
Nozzle to sample distance (mm)	15
Impact time (min)	10

4.2.2 Analysis of the signal-to-noise (S/N) ratio

The experimental results were further converted into signal-to-noise (S/N) ratios in order to reduce the experimental errors in the Taguchi method. In general, the performance criteria can be classified into three categories, namely the nominal-the-better, the higher-the-better, and the lower-the-better. In this study, the lower-the-better performance characteristic has been taken to obtain optimal process conditions since a minimum erosion wear loss is desired. The signal to noise (S/N) ratio(η) is defined as [14, 15]:

$$\eta = -10\, log(MSD) \quad (1)$$

where MSD is the mean square deviation for the erosion wear loss of the coatings. The MSD in this work can be expressed as:

$$MSD = \frac{1}{n}\sum_{i=1}^{n} E_i^2 \quad (2)$$

where n is the number of tests and E_i is the value of the erosion wear loss for the ith test.

Table 4.2 shows the L9 orthogonal array and the associated experimental results in terms of erosion wear losses, along with the S/N ratios which are calculated using Eqs. (1) and (2). It was observed that the E4 experiment generated the highest S/N ratio, namely 32.77 dB, which means that the E4 coating had the lowest erosion wear loss. The influence of each spray parameter is divided into different levels, which is mainly due to the orthogonality of the experimental design. The mean S/N ratio for each level of the different spray parameters and the variation span between the three levels are reported in Table 4.4. The ethanol flow rate shows the largest S/N variation span (3.26dB). Now, according to Taguchis methodology, the larger the S/N ratio variation span, the greater the influence of spray parameters. In view of that, it can be stated from Table 4.4 that the ethanol flow rate has the strongest influence on the erosion wear loss of the coatings. Moreover, the process parameters that affect the wear loss can be ranked in the following order: ethanol flow rate > oxygen flow rate > standoff distance > powder feed rate.

Table 4.4 S/N response for erosion wear

Parameter	Mean S/N ratio			Variation Span	Rank
	Level 1	Level 2	Level 3	Max - Min	
Ethanol flow rate (A)	26.91	30.17	28.95	3.26	1
Oxygen flow rate (B)	30.05	28.74	27.24	2.82	2
Powder feed rate (C)	28.28	29.28	28.48	1.00	4
Standoff distance (D)	28.75	27.99	29.30	1.31	3

Fig. 4.1 shows the mean S/N ratio curves associated with each of the four spray parameters for the erosion wear loss test. As mentioned above, the larger the S/N ratio, the smaller the erosion wear loss of the as-sprayed coatings. One can see that the ethanol flow rate and the oxygen flow rate exhibit greater S/N variation spans. When the ethanol flow rate increases from 24 slph (A1) to 32 slph (A3), the mean S/N ratio initially rises from a very low level to the top of the curve and then goes down slightly, which means that the erosion wear loss of the coating first decreases rapidly and then slightly increases. This may be attributed to the fact that the powder particles will melt better at higher ethanol flow rates, resulting in lower porosity

and higher microhardness of the coatings. However, the variation of the mean S/N ratio for the oxygen flow rate is totally different from that for the ethanol flow rate. The mean S/N ratio decreases continuously when the oxygen flow increases from 420 slpm (B1) to 540 slpm (B3). For higher oxygen flow rates, there is an excess of oxygen that acts as a coolant and shortens the residence time of particles in the flame, thus causing the temperature of the particles to decrease. This will subsequently increase the porosity and reduce the hardness of the coating [16, 17]. It is also observed in Fig. 4.1 that the mean S/N ratio for the powder feed rate increases at first and then decreases when this parameter passes from 50.7g/min (C1) to 102.7g/min (C3). In general, powder particles undergo incomplete melting at higher feed rate, resulting in poorer particle flattening and increased porosity, which in turn leads to poor erosion resistance. However, the case of C1 does not conform to this general rule: this may be due to experimental errors. The mean S/N ratio for the standoff distance decreases at first and then rises with the increase of the standoff distance from 240 mm (D1) to 300 mm (D3). Indeed, as the standoff distance increases, the powder particles have more time to interact with the flame and melt completely, resulting in a lower porosity of the coating. This enhances its erosion wear resistance. Picas et al. [18] actually pointed out that the increase in the standoff distance causes the temperature of the flying particles to increase and the velocity to decrease. Therefore, the better erosion wear resistance obtained at a standoff distance of 300 mm can be attributed to a more suitable set of values of particle velocity and temperature.

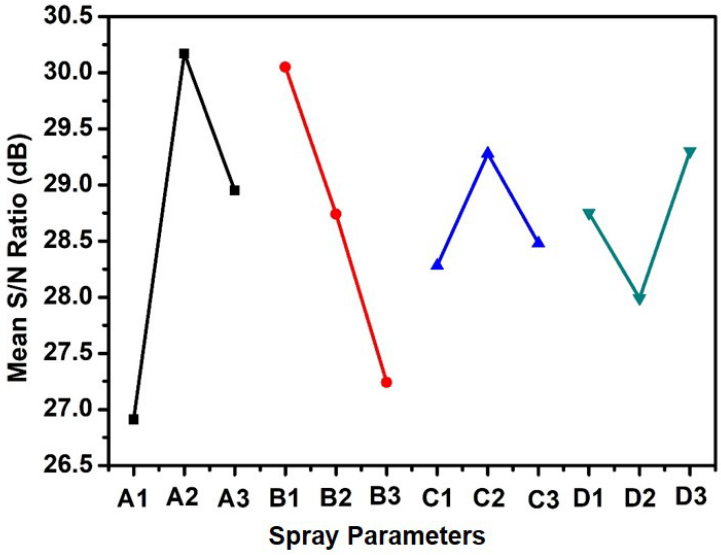

Fig. 4.1 The mean S/N ratio for erosion wear loss.

4.2.3 Analysis of variance (ANOVA)

A statistical analysis of variance (ANOVA) was employed to investigate the impacts of the different spray parameters on the erosion wear resistance. Table 4.5 shows the results of such analysis of variance for the S/N ratios relating to the erosion wear loss. The least influential factor, i.e. the powder feed rate, was categorized as “error”. As shown in Table 4.5, it can be concluded that the ethanol flow rate has the greatest impact on the resistance to erosion wear with a 50.07% contribution, followed by the oxygen flow rate that has a contribution of 36.74%. However, it appears that the standoff distance and the powder feed rate (categorized as “error”) have little effect on the erosion wear loss of the coatings with 8.04% and 5.16% contributions, respectively.

In conclusion, based on the S/N and ANOVA analyses, the spray parameters become optimized when adjusting the ethanol flow rate at level 2, the oxygen flow rate at level 1, the powder feed rate at level 2, and the standoff distance at level 3. To summarize, the optimal spray parameters (denoted as the “OSP”) to prepare the Cr_3C_2–NiCr coatings are 28 slph for the ethanol flow rate, 420 slpm for the oxygen flow rate, 76.7 g/min for the powder feed rate and 300 mm for the standoff distance. In fact, these OSP are the same as the parameters of the

E4 test in the orthogonal experiment. Therefore, Table 4.2 and Table 4.5 are consistent with each other and give the same set of optimized parameters for minimum wear erosion.

Table 4.5 Result of ANOVA analysis for S/N ratios of erosion wear loss.

Process parameter	Degree of freedom(f)	Sum of squares (S)	Variance (V)	F-ratio (F)	Contribution (%)
Ethanol flow rate (A)	2	16.25	8.12	9.71	50.07
Oxygen flow rate (B)	2	11.92	5.96	7.12	36.74
Standoff distance (D)	2	2.61	1.30	1.56	8.04
Powder feed rate (C)	2	1.67	0.84	1.00	5.16

4.2.4 Characterization of the "optimized" coatings

The X-Ray diffraction patterns of the powder and the HVOF-sprayed Cr_3C_2–NiCr coatings deposited using the OSP conditions are grouped in Fig. 4.2. It is reminded that the feedstock powder consisted predominately of NiCr and Cr_3C_2. The as-sprayed coatings were mainly composed of NiCr and Cr_3C_2 phases, which just reflect the powder phase composition, while a small amount of Cr_7C_3 and Cr_2O_3 peaks were also detected. Considering the temperature conditions of HVOF, only the NiCr phase and a small amount of Cr_3C_2 particles were probably melted, and a few new phases (Cr_7C_3 and Cr_2O_3) were formed. This result is consistent with other researchers reports on similar coatings [19].

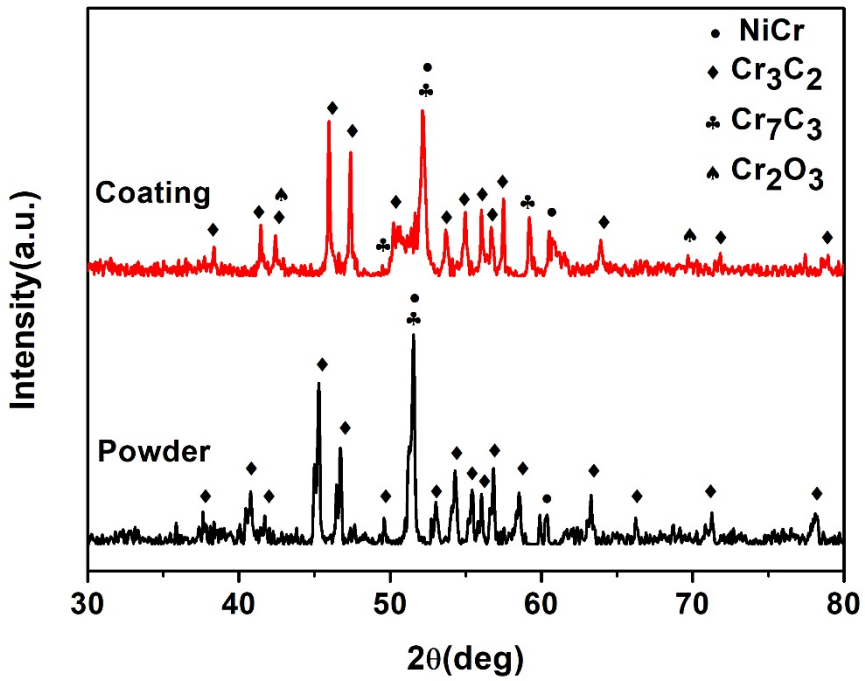

Fig. 4.2 XRD patterns of the Cr_3C_2–NiCr feedstock powder and of the sprayed coating.

Fig. 4.3 shows a low and high magnification of the polished cross-sectional microstructure of the Cr_3C_2–NiCr coating prepared under the OSP, at low and higher magnification. As shown in Fig. 4.3(a), it can be stated that the coating is very dense and well-bonded to the substrate, which is mainly thanks to the high velocity of HVOF thermal spraying. Both coarse and fine Cr_3C_2 grains are uniformly dispersed in the coating as shown in Fig. 4.3(b), and several pores and splat morphologies can be seen, which characterize the typical microstructure of Cr_3C_2–NiCr coatings [20]. A higher magnification picture and the cross-sectional element mappings reveal some details of the coating microstructure, as shown in Fig. 4.4. Microstructures with dark and light contrast can also be observed, corresponding to regions of lower and higher average atomic number and density, respectively. The brighter regions correspond to the matrix of NiCr, while the darker areas correspond to the carbide particles. However, carbides exhibit distinct greyscale contrast levels. In detail, an even darker core and a slightly brighter rim can be distinguished. The EDS analyses of these three areas are shown in Fig. 4.5. The element contents of point 3 indicates that the brightest area is NiCr matrix. Compared with point 1, the

nickel content of point 2 is slightly increased. One might infer that the darkest core is the original unaffected Cr_3C_2, whilst the brighter rim and the even brighter carbides are the result of slight decarburization and/or interaction with nickel. Similar observations were also made on other Cr_3C_2–NiCr coatings, as reported by W. Zhou [21].

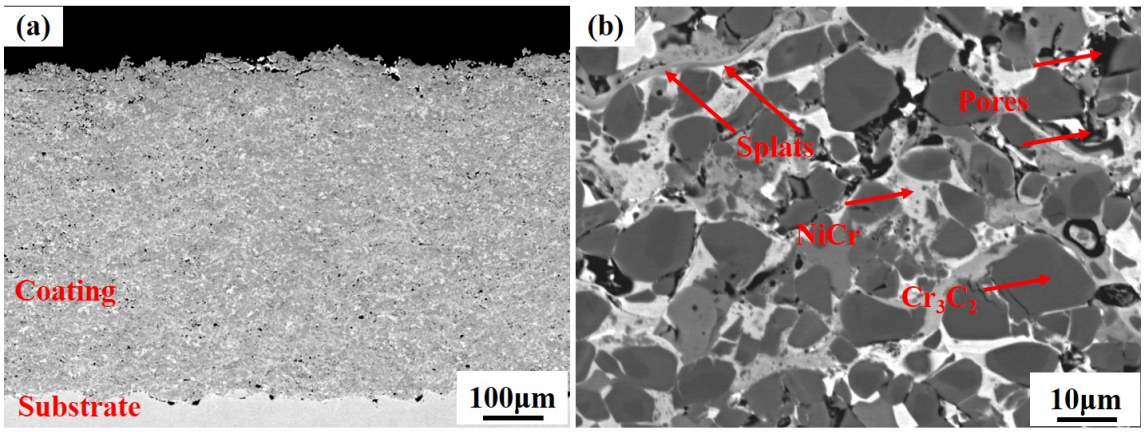

Fig. 4.3 Cross-sectional SEM micrographs of coated samples: (a) overview image; (b) higher magnification image.

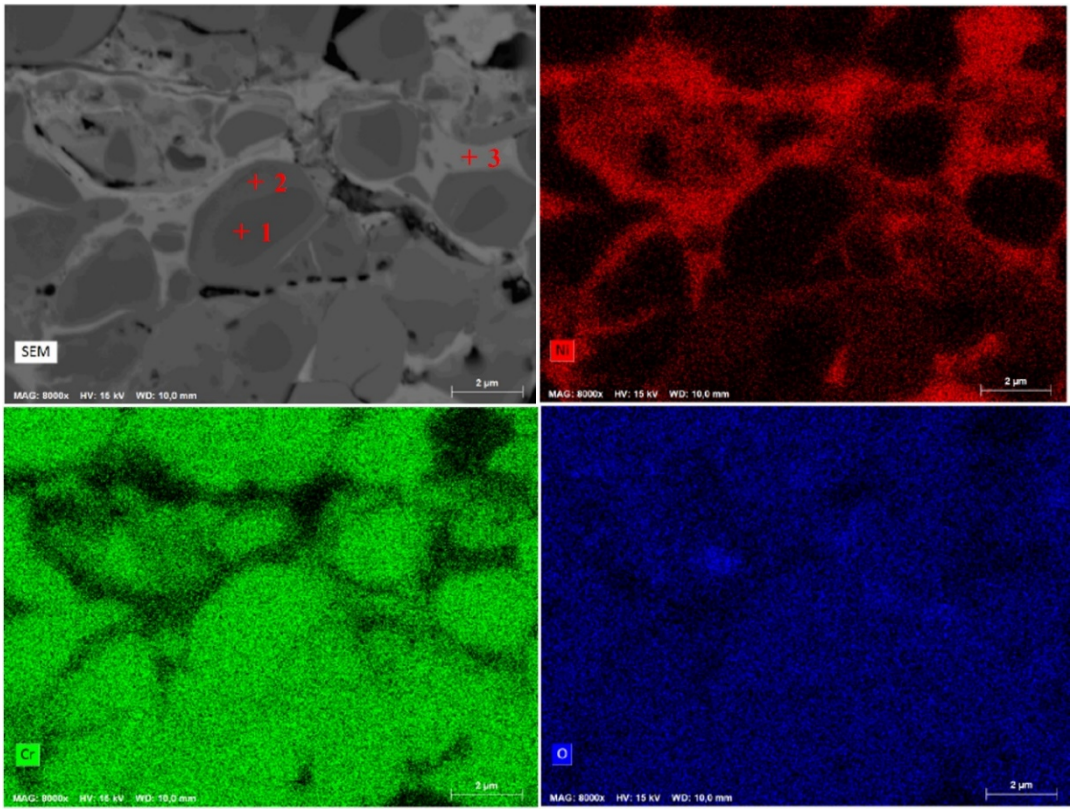

Fig. 4.4 Element mappings of a cross-section of as-sprayed Cr_3C_2-NiCr coating.

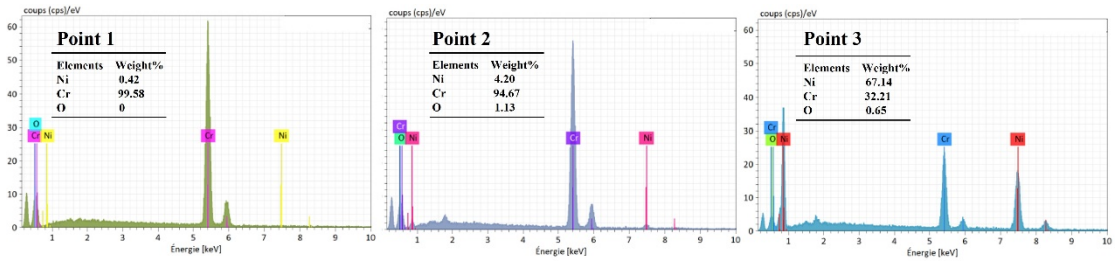

Fig. 4.5 EDS results of points 1, 2 and 3 in Fig. 8.

The optimized coating exhibits an average porosity value of 1.5% (with a standard deviation of 0.1%). The average microhardness value of that coating was found to be 1048 HV0.3 (with a standard deviation of 120 HV0.3). The average value of its fracture toughness was 4.03 MPa.m$^{1/2}$ with a standard deviation of 0.39. The bonding strength of the optimized coating is greater than 68 MPa, as it is the glue that cracked in the test. Furthermore, the performance comparison of Cr_3C_2-25wt.%NiCr coatings prepared by different HVOF processes is listed in Table 4.6. One can see that the porosity, fracture toughness, and bonding strength of the coating prepared with the new eGun HVOF are comparable to those prepared with the conventional HVOF methods; however, the microhardness proves to be much better. This result clearly suggests an interesting potential of the ethanol based HVOF technology within industrial applications and enticed to deepen its study.

Table 4.6 Compared performances of the Cr_3C_2-25wt.%NiCr coatings prepared via different HVOF processes.

Process	Torch	Fuel type	particle size (μm)	Porosity (%)	Microhard. ($HV_{0.3}$)	Fracture toughness ($MPam^{1/2}$)	Bond strength (MPa)	Reference
eGun HVOF	eGun	Ethanol	11-45	1.5±0.1	1048±120	4.03±0.39	> 68	this paper
HVOF	DJH2700	Propane	15-45	2.2±0.4	947±144	-	-	[22]
HVOF	DJH2700	Propane	10-38	1.7±1.0	938±79	-	-	[22]
HVOF	DJH2700	Ethene	15-45	-	950±120	-	-	[23]
HVOF	DJH2700	Propane	15-45	5.3±2.1	797±105	4.06±0.49	-	[24]
HVOF	-	Kerosene	5-40	-	-	-	64.4	[25]
HVOF	JP5000	Kerosene	-	1.88	879	-	62	[26]
HVOF	JP5000	Kerosene	15-45	6.3±3.2	709±88	3.59±0.48	-	[24]
HVOF	K2 (GTV)	Kerosene	15-45	< 1	949±83 ($HV_{0.1}$)	-	-	[20]
HVOF	K2 (GTV)	Kerosene	15-45	4.0±1.7	868±115	4.13±0.40	-	[24]

4.2.5 Erosion mechanism of the optimized coatings

Fig. 4.6 shows the average erosion rate, obtained at 30°, 60° and 90° impact angles, of Cr_3C_2-NiCr coatings prepared via the ethanol fueled HVOF device. Generally speaking, for cermet coatings, the erosion rate of coatings at high impact angles is higher than that at low impact angles. Zhang et al. [19] carried out a multi-angle study of the erosion behavior of HVOF sprayed Cr_3C_2-NiCr coatings and found that the erosion rate was almost proportional to the angle of impact. Our results also conform to their finding. We actually observed that the coatings exhibit the worse erosion resistance at 90° impact angle, with an erosion rate of 1.83×10^{-5} g/g. They exhibit the best erosion resistance at the 30° impact angle, and a medium resistance at 60° impact angle, the corresponding values being 1.03×10^{-5} g/g and 1.23×10^{-5} g/g, respectively.

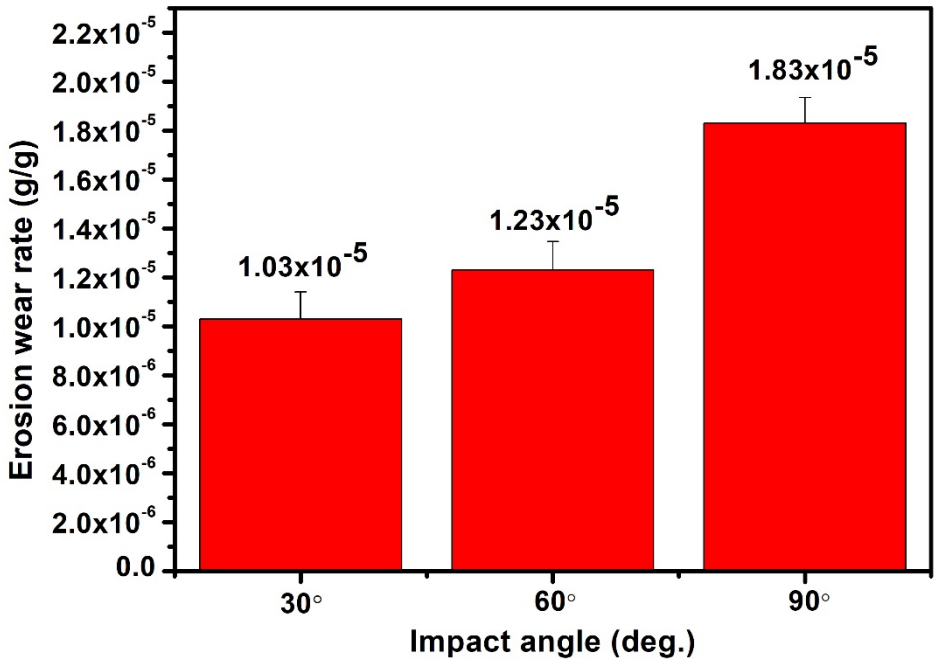

Fig. 4.6 Erosion wear rate of Cr_3C_2-NiCr coatings at different impact angles

Fig. 4.7 shows the SEM morphologies of the erosion scar generated on the "optimized" Cr_3C_2-NiCr coatings at different impact angles. At 30° impact angle, the erosion wear is dominated by micro-cutting and ploughing. Fig. 4.7(a) and (b) depict the respective micro cutting produced by the sliding action of erodent particles. The surface of the coating clearly shows characteristics of cutting burrs due to the micro cutting by small erosion particles, resulting in a large number of lips formed in the soft bound regions of the coating. However, the size and extent of coverage of the surface by cutting and ploughing marks suggest that these damages affect both the matrix and the carbide grains. Many ploughings are formed on the surface of the coating through long-distance cutting, which is caused by the relatively large-size of the erosion particles. The underlying reason is that the coating is mainly removed by the plastic deformation of the matrix through cutting, as well as the micro-cutting of the carbide grains [19].

Fig. 4.7(c) and (d) exhibit the aspect of the eroded surface of the coating at 60° impact angle and tend to indicate that the erosion wear mode is a combination of micro-cutting and

fatigue fracture spalling. With the increase of the impact angle, the number of lips and ploughings decreases, and the flattened area greatly increases. The impact force of the eroded particles can be divided into the horizontal component and the vertical component. As the impact angle increases, the vertical component of the impact becomes predominant in the aggression of the coating. The large ploughings are not easy to form, however the lip formed by micro-cutting can be easily eliminated by subsequent erodent particles to form a flat area. Moreover, some crater features are visible, and a small amount of alumina becomes embedded into the coating surface. A small number of splat fragmentations and cracks are observed in Fig. 4.7(d), revealing the pattern of fatigue fracture on the coating surface. The increase of the impact angle promotes the fatigue fracture and splat spalling of the coating, probably because the strain localization at a higher impact angle accelerates its erosion wear[27].

Fig. 4.7(e) and (f) display SEM images of coatings surfaces eroded at 90° impact angle; they show that the erosion wear is dominated by cracking and fatigue fracture spalling. One can observe many large and deep craters formed by the impact of the erodent particles on the surface of the coating after erosion wear, while the flat area is decreased. In addition, numerous embedded alumina particles and splat fragments are visible on the surface of the coating. A large number of cracks are also observed in Fig. 4.7(f). These indicate that the coating is removed mainly due to the cracking and fatigue fracture spalling at 90° impact angle.

The SEM micrographs of the cross-section of the eroded region of the optimized Cr_3C_2-NiCr coatings at the different impact angles are shown in Fig. 4.8. It can be seen that only rugged ravines are found in Fig. 4.8(a), with no obvious cracks at 30° impact angle. The erosion damage in Fig. 4.8(b) is slightly more severe than that in Fig. 4.8(a). The depth of the ravine is higher, indicating that more impact energy tends to induce a stronger inward erosion of the coating at 60° impact angle. Moreover, one also sees a small number of splat fragmentations and cracks, as visible in Fig. 4.8(b). It can be clearly inferred from the cross-sectional image of the coating that the erosion damage of the coating is the most serious at 90° impact angle. There are obvious indications of subsurface cracks and splat fractures in the cross-sectional view, as shown in Fig. 4.8(c). An enlarged SEM view of Fig. 4.8(c) is shown in Fig. 4.8(d),

which clearly indicates that the cracks propagate across some of the carbide particles, as well as along the interface between the carbide and the matrix in other cases. At 90° impact angle, the vertical component of the impact dominates the erosion of the coating, causing fatigue cracking and peeling of the same. This aspect of the cross-sectional views is consistent with the anti-wear performance of the coating.

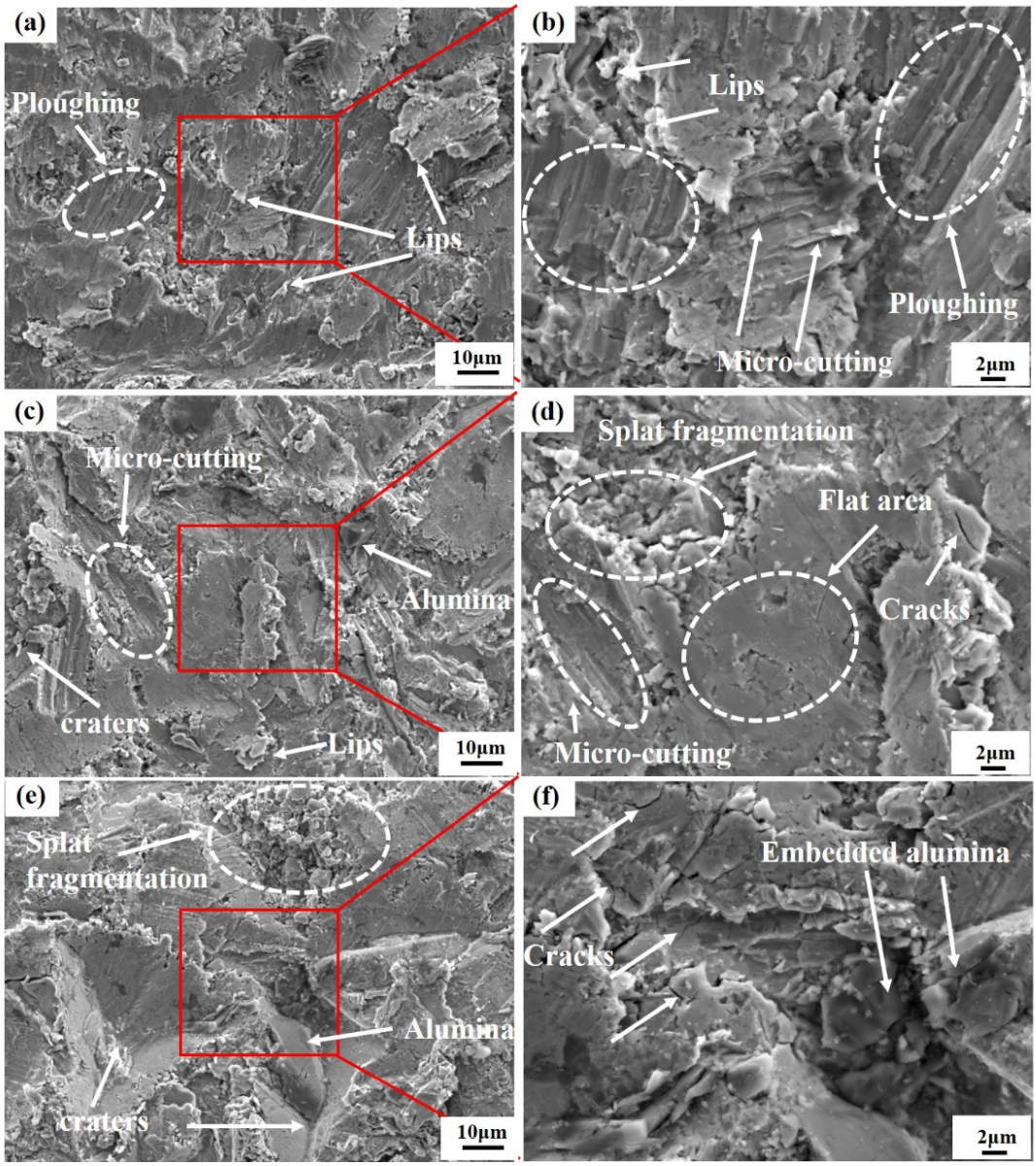

Fig. 4.7 SEM micrographs showing the morphology of the eroded surfaces of Cr_3C_2–NiCr coatings at different impact angles. (a) and (b): 30◦ impact angle; (c) and (d): 60◦ impact angle; (e) and (f): 90◦ impact angle.

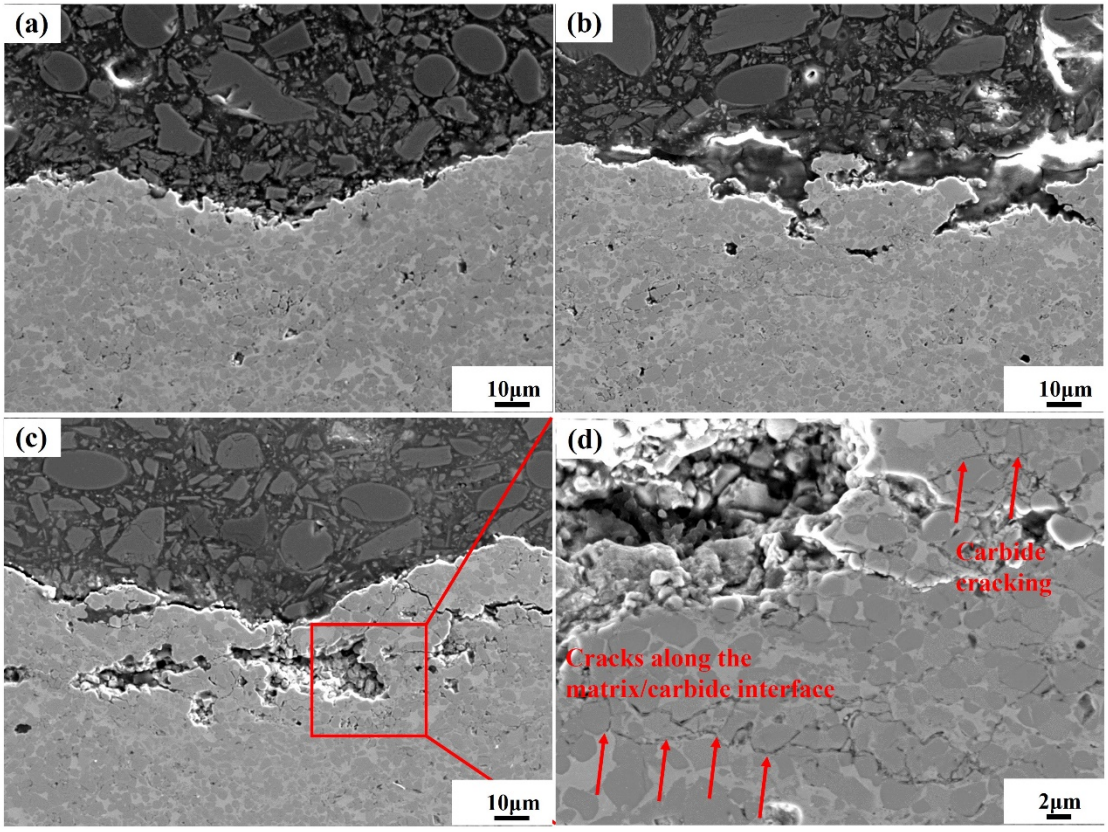

Fig. 4.8 SEM micrographs of the cross-section of the eroded region of Cr_3C_2–NiCr coatings at different impact angles. (a): 30◦ impact angle; (b): 60◦ impact angle; (c) and (d): 90◦ impact angle.

4.3 Effect of oxygen/fuel ratio on the erosion and sliding wear behavior of Cr_3C_2-NiCr Coatings

4.3.1 Preparation conditions of Cr_3C_2-NiCr Coatings with different oxygen/fuel ratio

The spraying conditions kept unchanged over this new series of HVOF experiments that are listed in Table 4.7, while the spraying parameters which have been varied in the study are given in Table 4.8. This set of variable parameters has selected in order to explore diverse fuel/gas flow rates and different stoichiometric factor with the view to evaluating their influence on the coating properties. The detailed conditions of the erosion tests are given in

Table 4.9. Each sample was eroded at an impact angle of 90° for 2 minutes. After testing, the sample was removed, cleaned in acetone, dried, and weighed on an electronic weight balance with an accuracy of 0.0001 g to determine the weight loss. The above erosion test procedure was repeated four times for a total time of 8 min to achieve steady state conditions. The erosion rate (mg/g) was defined as the ratio of the mass loss of the coatings (in mg) to the mass of erodent particles (in g). The eroded surface of the coatings was characterized by SEM to analyze the erosion mechanism.

Table 4.7 The spraying conditions of HVOF for the Cr_3C_2-NiCr coatings.

Gun	eGun
Fuel	ethanol
Carrier gas flow rate (Nitrogen)	8 slpm
Powder feed rate	76.7 g/min
Standoff distance	270 mm
Gun speed	500 mm/s
Offset	8 mm

Table 4.8 The spraying parameters and corresponding properties of the Cr_3C_2–NiCr coatings.

Test	C_2H_6O (slph)	O_2 (slpm)	SF	Porosity (%)	Microhard. ($HV_{0.3}$)	Fracture toughness ($MPam^{1/2}$)
E1	20	480	1.25	3.39±0.46	669.4±40.0	0.33±0.08
E2	24	480	1.04	1.80±0.41	916.1±28.5	1.39±0.36
E3	28	480	0.89	0.68±0.15	1006.6±56.2	2.38±0.64
E4	32	480	0.78	0.76±0.11	1052.7±73.9	2.65±0.63
E5	28	420	0.78	0.34±0.07	993.4±66.4	3.64±0.57
E6	28	540	1.00	2.02±0.60	1031.1±43.5	3.73±0.39
E7	28	600	1.12	1.39±0.29	996.6±73.2	1.80±0.64

Table 4.9 Erosion test conditions.

Erodent material	Alumina
Average erodent size (μm)	250
Erodent velocity (m/s)	Constant
Erodent feed rate (g/min)	150
Impinging angle (°)	90
Test temperature	Room temperature
Nozzle diameter (mm)	9.5
Nozzle to sample distance (mm)	15
Impinging time (min)	8

4.3.2 Phase composition and microstructure of the coatings

Fig. 4.9 gives the XRD patterns of the feedstock powder and as-sprayed coatings deposited using various spray parameters. The phases of the as-received powder are mainly composed of NiCr and Cr_3C_2. There is no significant difference in the XRD results of the seven sets of coatings prepared with different parameters. Therefore, it can be inferred that different oxygen/ethanol ratios have little effect on the phase composition of the Cr_3C_2-NiCr coatings. The coatings consisted predominately of NiCr based matrix and Cr_3C_2 phases, as well as a small amount of Cr_7C_3 and Cr_2O_3. This is consistent with other literature reports for this kind of coating [28]. Bolelli et al. [24] namely reported that HVOF-sprayed Cr_3C_2-NiCr coatings retain the qualitative phase composition of the raw powders, including Ni-based matrix, Cr_3C_2 carbide phase, and minor amounts of the Cr_7C_3 and Cr_2O_3 as well.

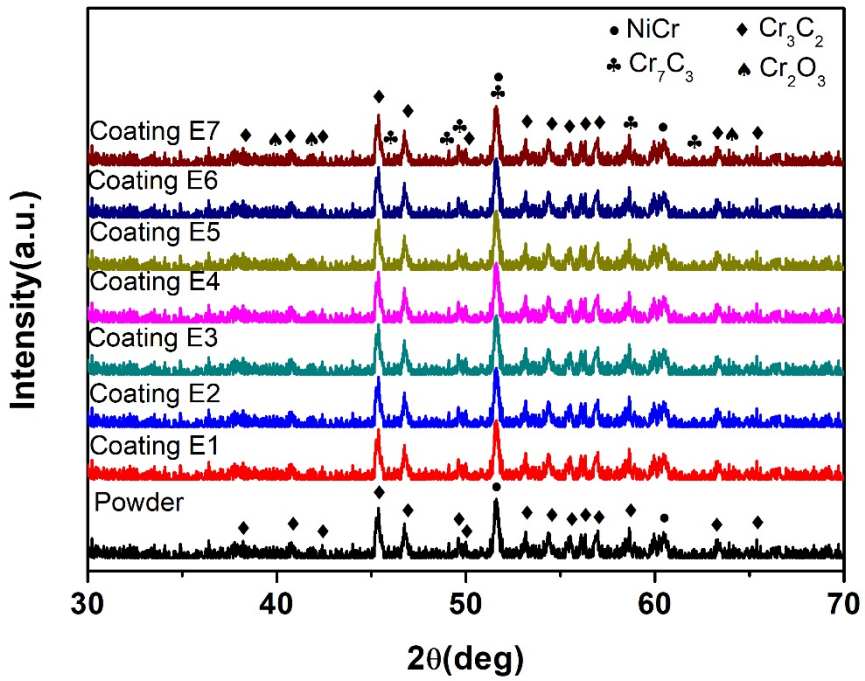

Fig. 4.9 XRD patterns of the Cr_3C_2–NiCr feedstock powder and prepared coatings.

Fig. 4.10 shows the cross-sectional microstructure of Cr_3C_2-NiCr coating after polishing. Although the stoichiometry factor (SF), that is the oxygen/ethanol ratio, has no obvious effect on the phase composition of the coating, it has a significant impact on the microstructure of the coating. In order to compare the microstructure differences of the coatings obtained with different stoichiometry factors, the coatings E1 and E5 were selected for analysis. The two sets of coatings prove to be well bonded with the substrate, while the coarse and fine Cr_3C_2 grains and a small number of pores are evenly distributed in the coating. However, as shown in Fig. 4.10(a) and (c), coating E5 is obviously denser and less porous than coating E1. The higher magnification BSE image shows more clearly some of the differences in the microstructures of the two sets of coatings, as shown in Fig. 4.10(b) and (d). In the two sets of coatings, the dark carbide grains are distributed along the light-colored Ni-based matrix. Many pores and cracks are found in the coating E1, and almost no splat is found. It is worth mentioning that the pore level in the coating E5 is significantly reduced. There are typical splats structures, and almost no detectable cracks are found. Compared with the coating E1, the powder particles

which generated the coating E5 underwent a more extensive melting, resulting in a significantly denser microstructure. This is mainly due to the distinct stoichiometry factors used for the two sets of coatings. The stoichiometry factor of the coating E1 is 1.25, that is, the ethanol is completely burned and there is an excess of oxygen to act as a cooling gas, resulting in a decrease in the temperature of the powder particles and a relatively poor melting state. On the contrary, the stoichiometry factor of coating E5 is 0.78. Theoretically, the ethanol is not completely burned at this condition, but the temperature of the particles may be relatively more suitable for the powder to become more extensively melted this time, thereby leading to a better microstructure. The coating properties obtained with other stoichiometry factors, ranging from 0.78 to 1.25, will be analyzed in detail in the following chapters.

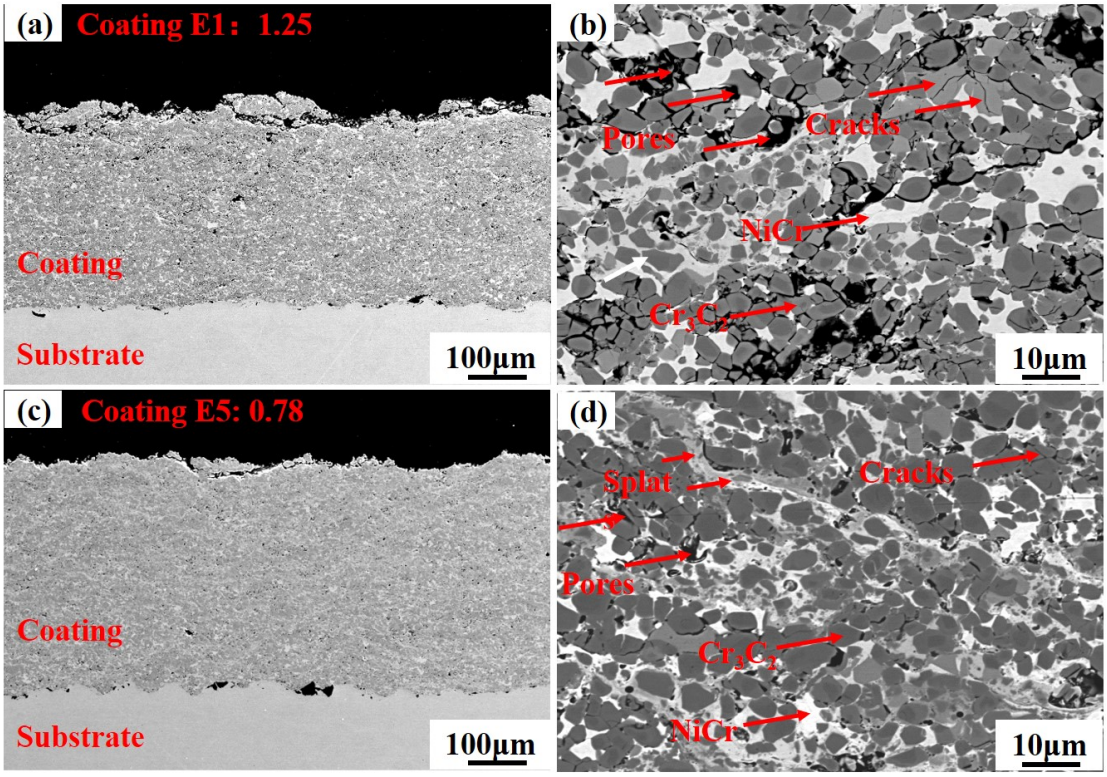

Fig. 4.10 Cross-sectional SEM micrographs and BSE images of the Cr_3C_2-NiCr coating after polishing: (a) and (b): coating E1; (c) and (d): coating E5.

4.3.3 Porosity and microhardness

The porosity and microhardness of Cr_3C_2-NiCr coatings prepared using various spraying

parameters are listed in Table 4.8, as well as their standard deviation. Fig. 4.11 shows the evolution of coating porosity with the oxygen and ethanol flow rates. The ratio of the flow rate of oxygen to that of ethanol determines the stoichiometry factor of the combustion. During the experiments summarized in Fig. 4.11(a), the ethanol flow rate was adjusted at 28 slph while the oxygen flow rate was increased from 420 slpm to 600 slpm. The corresponding stoichiometry factor rose from 0.78 to 1.12. It was then found that the porosity of the coating rose from 0.34% to the maximum value of 2.02%, and then dropped slightly. During the experiments summarized in Fig. 4.11(b), the oxygen flow rate was maintained at 480 slpm and the ethanol flow rate was increased from 20 slph to 32 slph; therefore, the corresponding stoichiometric factor dropped from 1.25 to 0.78. Then the porosity of the coating dropped from 3.39%, a quite high value, down to 0.68%, and then remained virtually stable. Based on the results of Fig. 4.11, one can conclude that the change of the ethanol flow rate has a more significant impact on the porosity of the coating than that of the oxygen flow rate. In addition, when the stoichiometry factor exceeds 1, the porosity of the coating is significantly larger. On the contrary, when the stoichiometry factor is less than 1, the porosity level of the coating remains below 1%. It is known that the porosity level of the coating is related to the temperature and velocity of the in-flight particles during the spraying process. Therefore, the combination of high temperature and high velocity facilitate the melting and deformation of the flying particles, making them able to fill - upon impact - the pores and defects in the previously deposited layer, resulting ultimately in lower porosity levels. When the stoichiometry factor is smaller than 1, the lower porosity of the coating may be attributed to the higher flame temperature, which results in more extensive powder particle melting. When the stoichiometry factor is greater than 1, the excess oxygen lowers the combustion temperature so that the residence time of the powder in the flame becomes shorter, resulting in poorer melting of the powder particles, thereby increasing the porosity of the coating. In addition, when the total flow rate increases, the porosity of the coating also decreases due to the increase in powder velocity [29]. In summary, for Cr_3C_2-NiCr coatings prepared using the ethanol-fueled HVOF spray gun, it can be inferred that when the stoichiometry factor is slightly lower than 1 (at 0.78-

0.89), the velocity and temperature of the flying particles are more appropriate for the complete melting and deformability of the in-flight particles, resulting in a lower coating porosity.

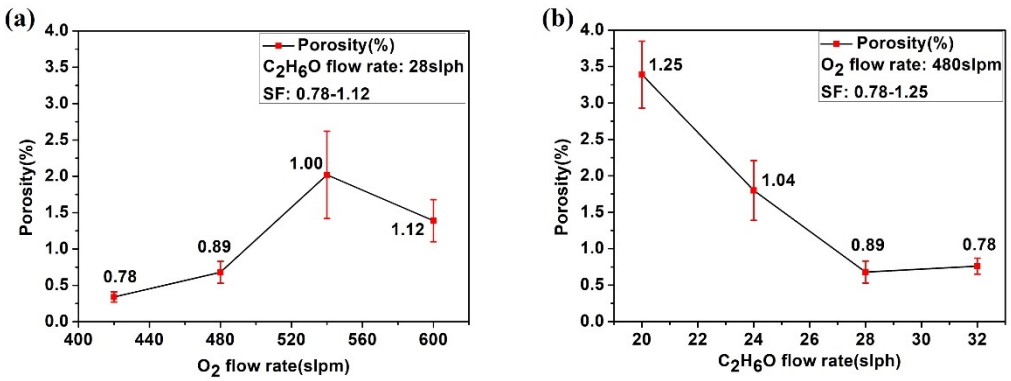

Fig. 4.11 Evolution of the porosity of Cr_3C_2-NiCr coatings: (a) vs. different O_2 flow rates; (b) vs. different C_2H_6O flow rates.

In the experiments summarized in Fig. 4.12(a), the ethanol flow rate was adjusted at 28 slph and the oxygen flow rate gradually was risen from 420 slpm to 600 slpm. In view of the standard deviation, one can say that the microhardness of the Cr_3C_2-NiCr coating did not change significantly under these conditions. Although the stoichiometry factor increased from 0.78 to 1.12 in this case, the impact on the coatings microha rdness was relatively minor. However, a trend could still be observed: as the oxygen flow rate increased from 420 slpm to 540 slpm, the microhardness of the coating slightly increased from 993.4 HV0.3 to 1031.1 HV0.3 (Table 4.8). Moreover, when the stoichiometry factor reached 1, the microhardness reached the maximum, and then decreased slightly with a further increase of the oxygen flow rate. However, when the oxygen flow rate was set at 480 slpm, a significant increase in the microhardness of the coating (from 669.4 HV0.3 to 1052.7 HV0.3) was observed when the ethanol flow rate was risen from 20slph to 32 slph, as illustrated in Fig. 4.12(b). This corresponded to the stoichiometry factor decreasing from 1.25 to 0,78. Obviously, compared with the oxygen flow rate, the ethanol flow rate has a greater impact on the microhardness of the coating. When the ethanol flow rate was adjusted at a higher value, the microhardness of the coating stayed at a high value level. To explain this result, one can mention the fact that the microhardness of the coatings measured at 300 gf is as sensitive to interlayer cohesion as the

intra-lamellar characteristics (decarburization, phase composition). Since the intra-lamellar characteristics of all samples are practically the same, as suggested in section 4.3.2, then the microhardness reflects the change in interlayer cohesion. It is probable that at higher ethanol flow rates, the interlayer cohesion is enhanced due to the higher values of particle temperature and velocity. Excessive oxygen flows reduce the temperature of the particles, resulting in greater porosity, which may result in a decrease of microhardness [29].

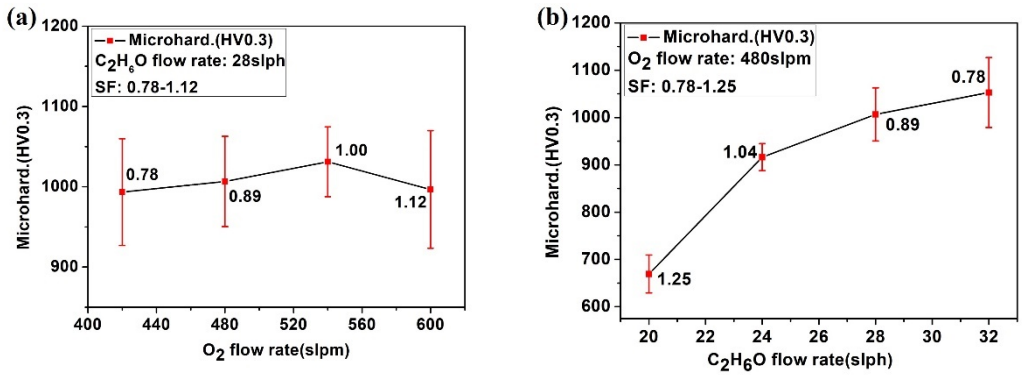

Fig. 4.12 Evolution of the microhardness of Cr_3C_2-NiCr coatings: (a) vs. different O_2 flow rates; (b) vs. different C_2H_6O flow rates.

4.3.4 Fracture toughness

The fracture toughness tests were conducted using the indentation method. The data of fracture toughness obtained for the coatings deposited using different parameters are listed in Table 4.8. Its evolution versus the oxygen and ethanol flow rates is shown in Fig. 4.13. In Fig. 4.13(a), the flow rate of ethanol was fixed at 28 slph, and that of oxygen was increased from 420 slpm to 600 slpm. The fracture toughness first decreased and then increased as the stoichiometry factor increased from 0.78 to 1.00; it again decreased when the stoichiometry factor exceeded 1, as shown in Fig. 4.13(a). When the oxygen flow rate is maintained at 480 slpm and that of ethanol is increased from 20 slph to 32 slph (Fig. 4.13(b)), then the fracture toughness of the coating shows a similar evolution trend to that of the microhardness. This time, the fracture toughness gradually increases from 0.33 $MPam^{1/2}$ to 2.65 $MPam^{1/2}$, as the stoichiometry factor decreases from 1.25 to 0.78, as shown in Fig. 4.13(b).

In summary, when the ethanol flow rate exceeds or equals 28 slph and the stoichiometry factor does not exceed 1, then the fracture toughness remains higher than 2.38 $MPam^{1/2}$, which conforms to the values reported by other researchers [30]. This result is of great interest to optimize the quality of Cr_3C_2-NiCr coatings using the ethanol-fueled HVOF gun.

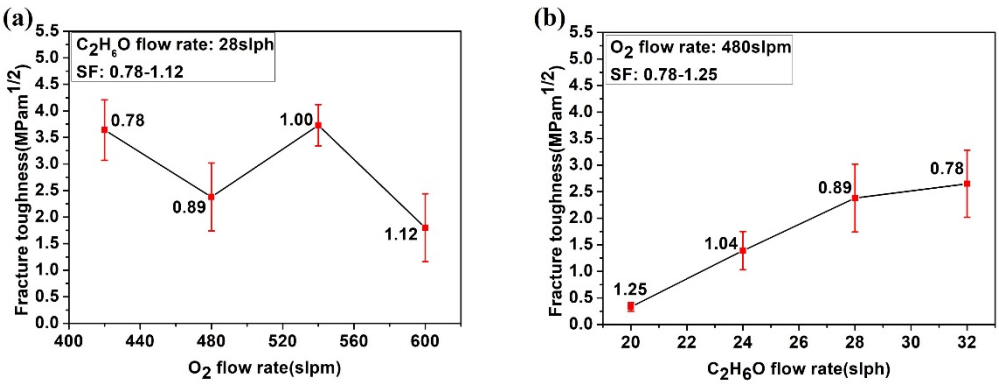

Fig. 4.13 Evolution of the fracture toughness of the Cr_3C_2-NiCr coatings: (a) vs. different O_2 flow rates; (b) vs. different C_2H_6O flow rates.

Typical indent micrographs taken on the cross-sections of the E1 and E5 coatings are shown in Fig. 4.14. One sees that the cracks are mainly generated at the corners of the indent. In addition, the cracks produced on the E1 coating are significantly longer than those on E5, as shown in Fig. 4.14(a) and (c). This is consistent with the evolution of the fracture toughness recorded in Table 4.8. Furthermore, the cracks mainly propagate into the direction parallel to the coating/substrate interface, which corresponds to an anisotropic crack propagation in the coating layers, and results from the elongated nature of the splats and the associated residual stress fields [31]. A close observation of Fig. 4.14(b) and (d) reveals that the cracks present both on the E1 and E5 coatings are propagating along the interface between the matrix and the carbide (see arrows). This is attributed to a limited cohesion between the carbide grains and the surrounding matrix.

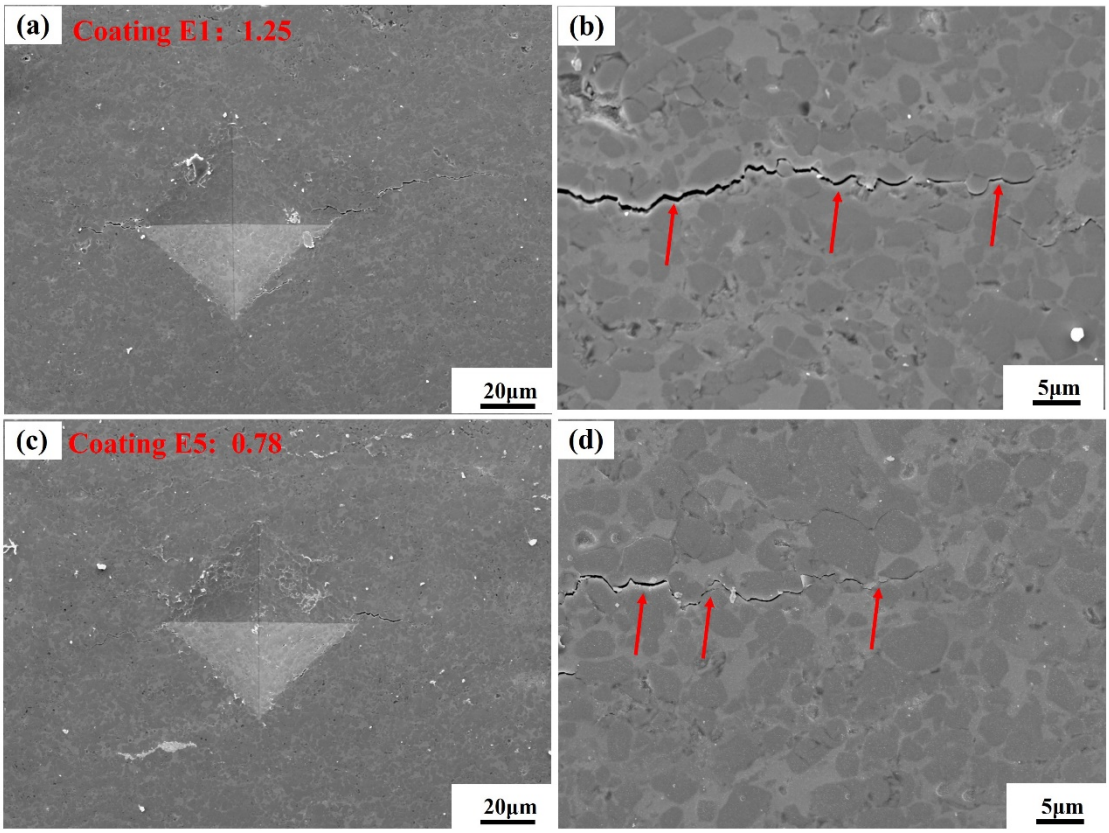

Fig. 4.14 Cross-sectional morphologies and enlarged views of the eroded region of Cr_3C_2–NiCr coatings. (a) and (b): coating E1; (c) and (d): coating E5.

4.3.5 Erosion tests

The erosion tests performed on the Cr_3C_2-NiCr coatings were carried out using solid particles a 90° impact angle and different stoichiometry factors. The results are shown in Fig. 4.15. One sees that the erosion resistance is almost inversely proportional to the stoichiometry factor. The higher the stoichiometry factor, the greater the erosion mass loss of the coating, which means the worse its erosion resistance. Among the seven groups of coatings, the erosion mass loss of the E1 coating (SF=1.25) is significantly higher than that of the other coatings, indicating that the erosion resistance is the lowest. When the stoichiometry factor is less than 1, the erosion of each coating is relatively low, and there is not much difference. In relative terms, the coating E3 and E5 undergo the lowest erosion mass loss, which means they have the best erosion resistance. It can be seen from Fig. 4.16(a) that the erosion wear rate is basically proportional to the porosity of the coating. The lower the porosity, the lower the erosion wear

rate of the coating. Except for coating E6, for which it is likely that the larger standard deviation of the porosity explains its mismatch with the observed trend. On another hand, the erosion wear rate varies in the opposite direction to that of microhardness and fracture toughness of the coating, as shown in Fig. 4.16(b) and (c). Better mechanical properties imply that both the inter- and intra-layer cohesion of the coating are good, resulting in better erosion resistance.

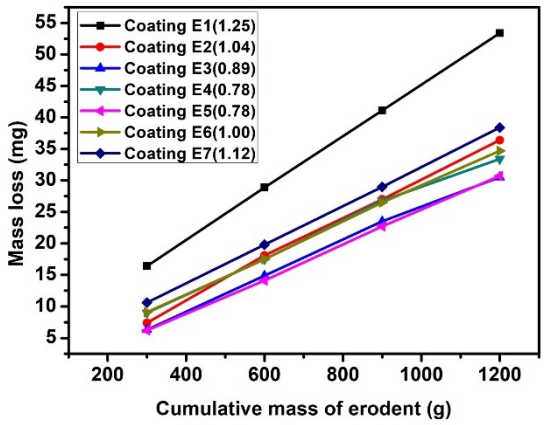

Fig. 4.15. Erosion results in terms of coating mass loss as a function of cumulative mass of erodent

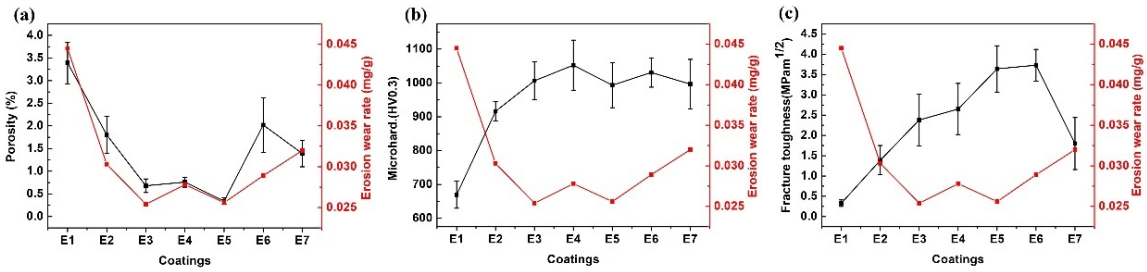

Fig. 4.16. Evolution of the erosion wear rates of the as-sprayed Cr3C2–NiCr coatings: (a) vs. porosity; (a) vs. microhardness; (b) vs. fracture toughness.

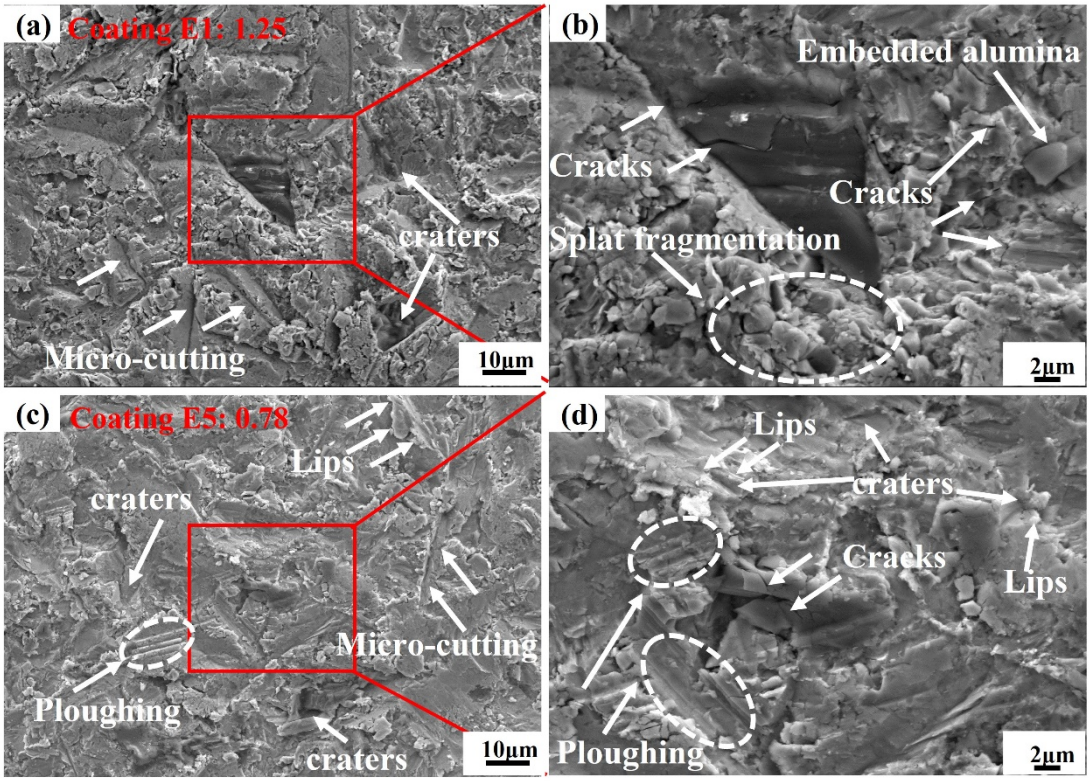

Fig. 4.17. General morphologies and enlarged views of the eroded surfaces of the Cr_3C_2–NiCr coatings. (a) and (b): coating E1; (c) and (d): coating E5.

We decided to examine, for comparison, the morphologies of the eroded surfaces of the E1 and E5 coatings which featured the worst and best erosion resistance, respectively (Fig. 4.15). At an impact angle of 90°, some micro-cuttings and many large and deep crater features were found to be distributed on the eroded surface of the E1 coating in Fig. 4.17(a). In the enlarged image of Fig. 4.17(b), more specific features of the erosion surface morphology are observed. Some erodent particles embedded in the coating are found. Moreover, large areas of splat fragmentation and many micro-cracks were generated with the cumulated stress caused by the impacts. These are basically the characteristics of fatigue fracture, indicating that the erosion mechanism of E1 coating is mainly dominated by fatigue fracture and peeling. At 90° impact angle, the impact energy tends to be perpendicular to the coating. The coating is prone to fatigue fracture and splat spalling on account of its weak hardness and fracture toughness, especially at higher porosity levels. In Fig. 4.17(c), micro-cutting, crater morphology as well as some ploughing and lips features were found in the eroded surface of the E5 coating. However, the craters were obviously smaller in area and shallower in depth. In the partial

enlarged view of Fig. 4.17(d), the surface of the E5 coating obviously has fewer cracks, compared with the E1 coating and the splat fragmentation phenomenon is almost not found. Lips surround the craters, indicating strain localization and ploughing caused by plastic deformation, both of which indicates that the E5 coating has better toughness. A close look at Fig. 12(d) seems to reveal the presence of slightly darker carbide grains in the areas marked as "ploughing". It implies that the carbide grains of the E5 coating are well embedded in the NiCr matrix, so that they can be cut and ploughed together with the matrix without being pulled out. This may be attributed to the high hardness, high fracture toughness and low porosity of the E5 coating.

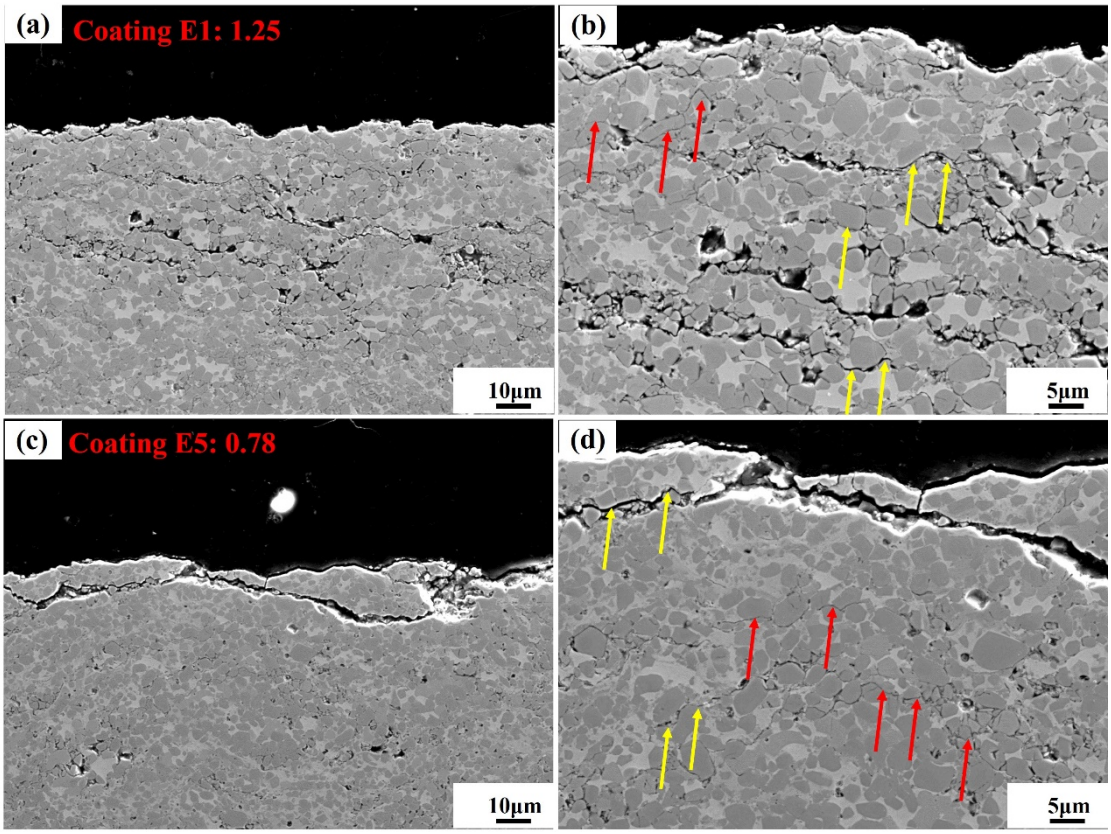

Fig. 4.18. Cross-sectional morphologies and enlarged views of the eroded region of Cr_3C_2–NiCr coatings. (a) and (b): coating E1; (c) and (d): coating E5.
The red arrows indicate the carbides cracking. The yellow arrows indicate that the cracks propagate along the matrix/carbide interface.

Fig. 4.18 shows the morphologies of the cross-section of the E1 and E5 coatings in the eroded area. As shown in Fig. 4.18(a) and (b), one observes a large number of surface cracks, subsurface cracks and splat fragmentations in the E1 coating. In addition, the cracks propagate

deeper into the coating. In Fig. 4.18(b) and (d), the red arrows indicate the phenomenon of carbide cracking, and the yellow arrows show that the crack propagates along the matrix/carbide interface. From the partial enlarged view of Fig.4.18(b), one can infer that the cracks originate from the cracking of carbides and some fragile pores, and then mainly extend horizontally along the matrix/carbide interface. On the one hand, more pores become the origins of the crack, and on the other hand, the pores also promote the propagation of the crack. Compared with the coating E1, the erosion damage of the E5 coating is obviously much smaller. Fewer cracks and splat fragmentations are observed, as shown in Fig.4.18(c). Although a small amount of carbide cracking is also found in the deeper area of the coating, the cracks are mainly generated and propagate on the surface of the coating, as shown in the enlarged view of Fig. Fig.4.18(d). This could be due to the better mechanical properties of the E5 coating with the SF of 0.78.

4.3.6 Coefficient of friction and wear rate

The friction curves of Cr_3C_2–NiCr coatings established at room temperature show an initial running-in stage with increasing friction coefficient followed by a steady-state regime that lasts for the majority of the test duration, as shown in Fig. 4.19. The mean values of friction coefficients of the coatings deposited with various parameters after reaching the steady-state are shown in Fig.4.20. It can be seen that the steady state coefficients of friction are comprised in a relatively narrow range between 0.63 and 0.74, which is comparable with the values commonly reported in the literature for similar coatings evaluated under similar conditions [22]. Such narrow range indicates a small effect of the spray parameters on the steady-state coefficient of friction. The dry sliding wear rates of the Cr_3C_2–NiCr coatings conducted at room temperature are shown in Fig.4.20. The wear rates of the E1 and E2 coatings are 4.69×10^{-6} $mm^3/(N \cdot m)$ and 3.71×10^{-6} $mm^3/(N \cdot m)$, respectively, two values significantly higher than those of other coatings. This is due to the lower microhardness and fracture toughness of the coatings generated with the SF higher than 1. The wear rates of the other five coatings are between 1.73×10^{-6} $mm^3/(N \cdot m)$ and 2.52×10^{-6} $mm^3/(N \cdot m)$, which is also consistent with the values

generally reported in the literature for such coatings tested under similar conditions [32]. Fig. 4.21 reveals that the wear rates of the coatings are almost inversely proportional to the microhardness and fracture toughness of the coatings. The higher the microhardness, the higher is the fracture toughness and the lower is the wear rate. As stated in Section 4.3.3 and 4.3.4, when the stoichiometric factor is slightly lower than one, the coatings microhardness and fracture toughness are higher, thereby resulting in better wear resistance.

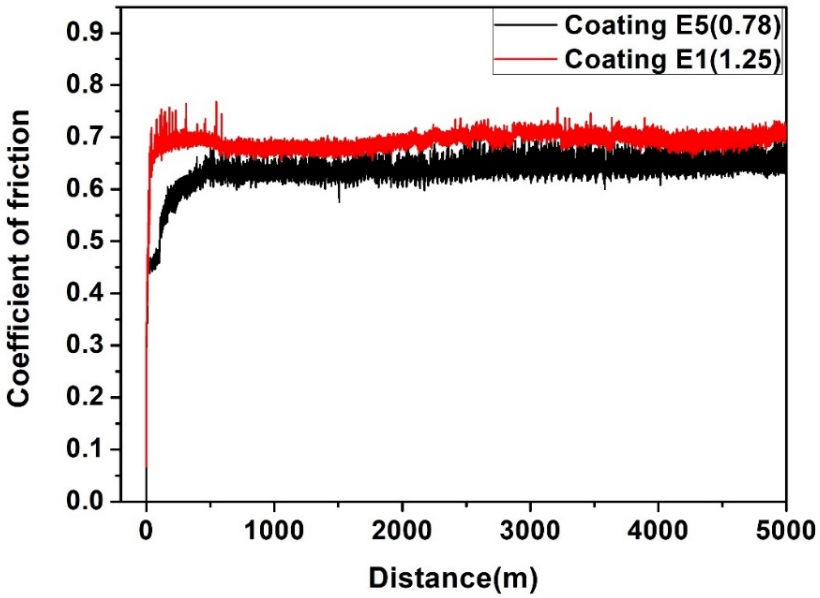

Fig. 4.19. Evolution of the friction coefficient of E1 and E5 coatings.

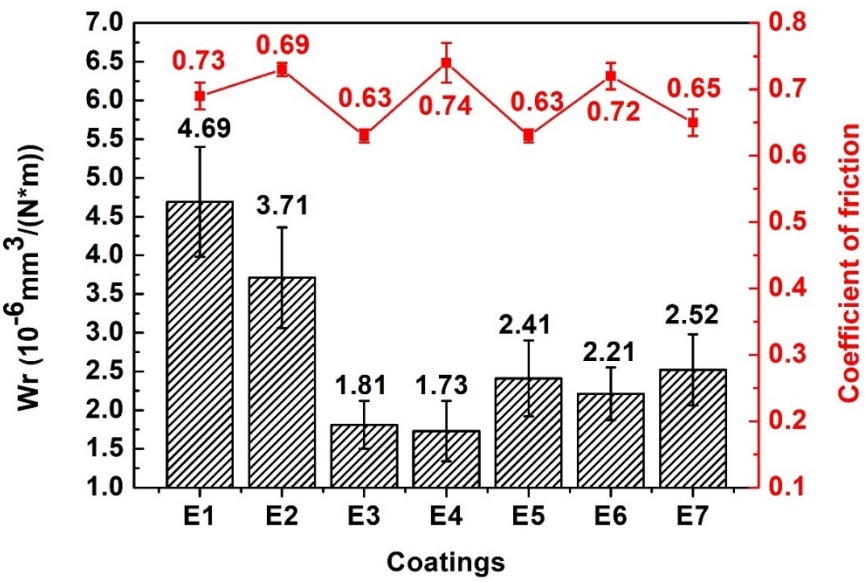

Fig.4.20. The wear rates and coefficients of friction of the as-sprayed Cr_3C_2–NiCr coatings

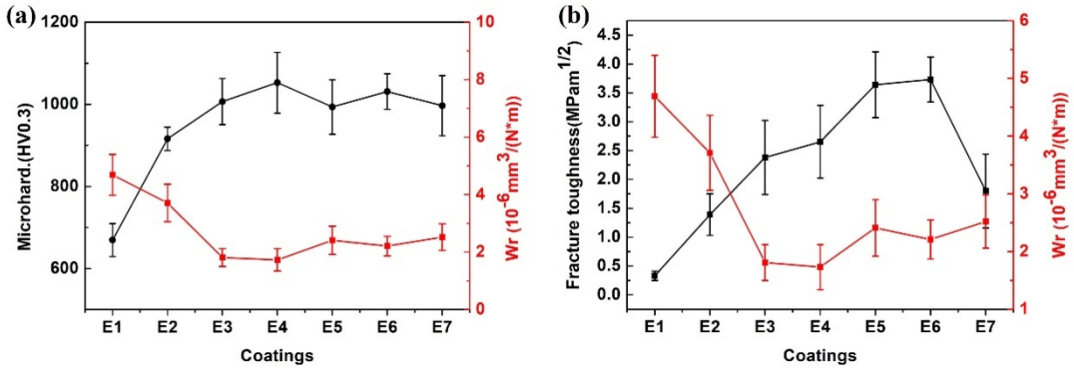

Fig.4.21. Evolution of the wear rates of the as-sprayed Cr_3C_2–NiCr coatings: (a) vs. microhardness; (b) vs. fracture toughness.

4.3.7 Wear mechanism of the coatings

By analyzing the wear scar surfaces of the coatings E1 and E5, it can be concluded that the wear mechanism of Cr_3C_2−NiCr coatings prepared with the ethanol-fueled HVOF device is a combination of i) abrasive grooving, ii) peelings caused by cracking, fragmentation, and pull-out of carbide grains, iii) delamination and tribo-oxidation.

(1) Abrasive grooving can be found on both wear scar surfaces of the coatings E1 and E5; they are created by hard alumina asperities and/or by wear debris particles. They can freely move between the mating bodies or stick to the counter body surface. Grooves marked with arrows in Fig. 4.22(c) and (f) are produced both in the darker and lighter areas, which indicates that they affect both the metal matrix, and the chromium carbide grains. This point is confirmed by the EDX analysis that we performed at the points marked in Fig. 4.22 and that are listed in Table 4.10. The abrasion grooves on the coating E1 are fewer than those on E5, possibly because the surface microhardness of E5 is higher. The coating E1 is more susceptible to extensive wear damage caused by cracking and delamination due to its low microhardness and fracture toughness. In addition, the wear scar width of the coating E1 is significantly larger than that of the coating E5 as shown in Fig. 4.22(a) and (d), which is consistent with the result of the wear rate data set out in Fig.4.20.

(2) Peelings caused by cracking, fragmentation and pull-out of carbide grains are

particularly evident in Fig.4.23. Cracks in Fig. 4.22(c) and (f) can be observed on both the wear scar surfaces of the coatings E1 and E5. The enlarged images of the wear scars cross-sections in Fig.4.23(b) and (d) show a large number of microcracks and long cracks on the surface and in the subsurface of the coating. The red arrows represent the microcracks generated by the internal cracking of the carbide, while the yellow ones indicate the long cracks that extend along the carbide/metal matrix interface. The occurrence and propagation of these cracks can be mainly attributed to the presence of defects in the carbide grains and to their limited cohesion with the surrounding matrix. Moreover, a significant number of carbide fragmentations was also found in Fig.4.23(b) and (d), which is caused by the cyclic stress of the wear test. The conjunction of carbide fragmentations and cracks promotes the local spalling of the splats. This aggressive mode of material removal greatly increases the wear rate of the coating. In addition, the pull-out of single carbide particles in the coating E5 is more intense than that in the coating E1 (see Fig. 4.22(c) and (f)). This may be because the coating E1 is prone to peel off in a relatively large area, so that one cannot easily observe the pull-out of an individual carbide particle. Overall, the wear damage of the coating E5 is slighter than that of the coating E1. In the latter sample, the damages are actually limited to a very shallow depth with moreover less cracking and fragmentation, due to the higher microhardness and fracture toughness of the coating E5.

(3) Delamination and tribo-oxidation are clearly observed in coatings E1 and E5. As shown in Fig. 4.22(b) and (e), the delamination of the coating E1 is obviously more serious. The delamination facies have a morphology that indicates adhesive wear, which probably depends both on the inter- and intra-lamellar cohesion. Fig.4.24(a) and (c) show the surface morphologies of the alumina counter-bodies against coatings E1 and E5, respectively. It is clearly observed that, during the continuous sliding friction process, some fragments of the coating surface are pulled off and displaced, tending to shroud the alumina counterparts. This is confirmed by the element mappings in Fig.4.24(b) and (d), which indicate that the surfaces of the alumina balls are covered by substantial amounts of Cr and Ni. The sliding process between the coating surface and the materials wrapping the counterpart surface results in high

friction. As shown in Fig.4.20, the average friction coefficient of the Cr_3C_2-NiCr coatings reached 0.63-0.74. Bolelli et al. [33] reported that the friction coefficient of the WC-CoCr coatings tested under similar conditions are relatively low, ranging from 0.45 to 0.50. They did not find any adhesion, nor any material transferred to the counterpart in their experimental conditions. High friction means significantly faster heating. Mohanty et al. [34] mentioned that the formation of a continuous oxidation film on Cr_3C_2-NiCr coatings, under similar conditions, which can reduce friction and wear, appears only at a sliding speed of about 1 m/s. In our case, while the rapid heating effect is not enough to produce such continuous oxidation friction film, it is sufficient to oxidize the debris particles and part of the transferred materials. This can be inferred from the presence of clusters of oxides on the coating surface in Fig. 4.22(c) and (f), while the EDX analysis also confirms the presence of a large amount of oxygen in these clusters (Table 4.10). The clusters of oxides generally have a wavy shape which reflects the sliding under the high contact pressure between the surface asperities or loose debris and the alumina counter-bodies. This morphology demonstrates the action of large tangential forces, which induce out-of-plane shear stresses and, as a result, out-of-plane plastic flow [22].

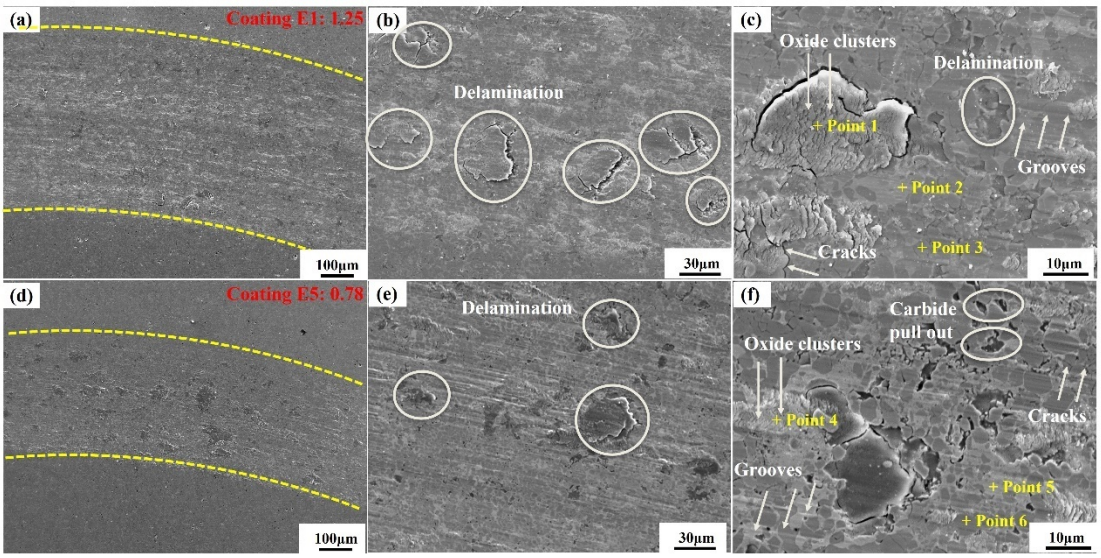

Fig. 4.22. SEM micrographs of the wear scar surfaces of Cr_3C_2−NiCr coatings. (a), (b) and (c): coating E1; (d), (e) and (f): coating E5.

Table 4.10. EDX analysis of the points in Fig. 4.22

Point	Element composition(wt.%)		
	O	Ni	Cr
1	40.50	15.85	43.65
2	0.67	83.54	15.79
3	0	99.23	0.77
4	40.31	16.93	42.76
5	0.39	77.80	21.81
6	0	99.71	0.29

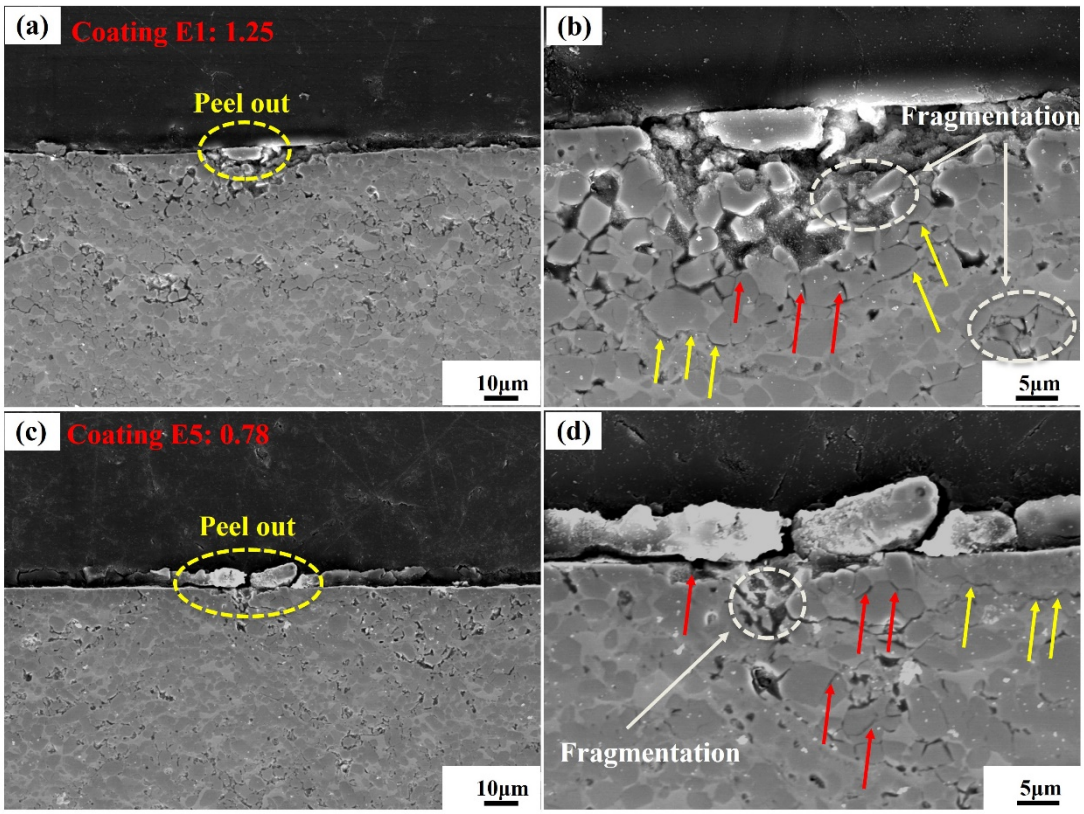

Fig. 4.23. SEM micrographs of the cross sections of the wear scars of Cr_3C_2−NiCr coatings. (a) and (b): coating E1; (c) and (d): coating E5. The red arrows represent the carbides cracking. The yellow ones indicate that the cracks propagate along the matrix/carbide interface.

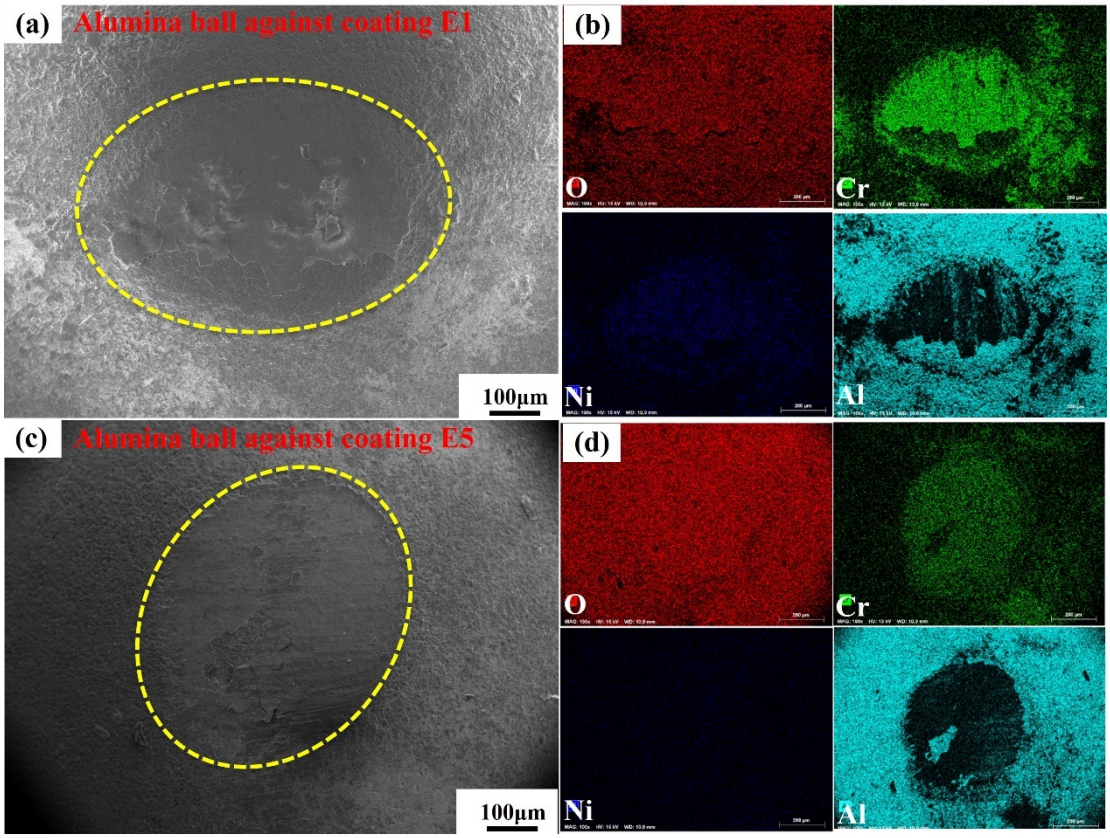

Fig. 4.24. SEM micrographs and element mappings of the wear scars produced on the alumina counter-bodies against Cr_3C_2–NiCr coatings. (a) and (b): vs coating E1; (c) and (d): vs coating E5.

4.4 Conclusions

This chapter has been devoted to studying the mechanical performances of Cr_3C_2–NiCr coatings prepared by the recently developed ethanol-fueled HVOF process. The optimization of the process parameters for Cr_3C_2–NiCr coatings was carried out using the Taguchi method to define the adequate spraying conditions for minimum erosion wear. Investigations were also conducted to determine the effect of different stoichiometric conditions on the evolution of the coating microstructure and the performance of the resulting Cr_3C_2-NiCr coating. The conclusions can be summarized as follows:

1. With the used torch, the optimal spray parameters for minimum erosion wear loss, i.e. for maximum wear resistance, were found to be 28 slph of ethanol flow rate, 420 slpm of oxygen flow rate, 76.7 g/min of powder feed rate and 300 mm of standoff distance. The ranking

of the importance of the spray parameters is as follows: ethanol flow rate > oxygen flow rate > standoff distance > powder feed rate.

2. Through an ANOVA analysis, it was confirmed that the ethanol flow rate has the greatest impact on the erosion wear resistance of the coatings with a contribution rating of about 50 %, followed by the oxygen flow rate with a contribution rating of about 37 %.

3. The coatings deposited under these optimum conditions have an average hardness of 1048 HV0.3 and a porosity of about 1.5 %. Their main constituent phases are NiCr and Cr_3C_2, although small amounts of Cr_7C_3 and Cr_2O_3 are also detected.

4. The erosion tests reveal that the coating exhibits a better resistance to erosion wear at 30° and 60° impact angles, as compared with 90° impact angle.

5. The erosion mechanism involves micro-cutting and ploughing of the matrix and the carbide grains, as well as the cracking of the carbides and fatigue fracture spalling caused by long-distance propagation of cracks along the matrix/carbide interface.

6. Changing the stoichiometric factors of the torch flame has virtually no effect on the phase composition of the Cr_3C_2–NiCr coatings but has a great impact on their microstructure and properties in terms of porosity, microhardness, fracture, erosion resistance and sliding wear resistance.

7. The Cr_3C_2–NiCr coatings with better mechanical properties are obtained with values of the stoichiometry factor below 1 (with an optimum at 0.78). This result contrasts with the values of the stoichiometric factor used in conventional kerosene-fueled HVOF devices, which are generally slightly greater than 1 to obtain a high quality Cr_3C_2–NiCr coating. This point is of great significance for optimizing the parameters of Cr_3C_2–NiCr coatings when using the new ethanol-fueled HVOF process.

8. The sliding wear mechanism of Cr_3C_2–NiCr coatings involves the conjunction of abrasive grooving, peelings induced by cracking, fragmentation, and pull-out of carbide grains, as well as delamination and tribo-oxidation.

References

[1] A. Tiwari, S. Seman, G. Singh, R. Jayaganthan, Nanocrystalline Cermet Coatings for Erosion–Corrosion Protection, Coatings 9(6) (2019) 400.

[2] K.J. Stein, B.S. Schorr, A.R. Marder, Erosion of thermal spray MCr–Cr3C2 cermet coatings, Wear 224(1) (1999) 153-159.

[3] P. Chhabra, M. Kaur, Wear and friction characteristics of atmospheric plasma sprayed Cr3C2–NiCr coatings, Tribology-Materials, Surfaces & Interfaces 14(3) (2020) 177-192.

[4] B. Song, J.W. Murray, R.G. Wellman, Z. Pala, T. Hussain, Dry sliding wear behaviour of HVOF thermal sprayed WC-Co-Cr and WC-CrxCy-Ni coatings, Wear 442 (2020) 203114.

[5] E. Vural, The study of microstructure and mechanical properties of diesel engine piston coated with carbide composites by using HVOF method, Transactions of the Indian Institute of Metals (2020) 1-10.

[6] K. Monaghan, A. Straub, Comparison of seal friction on chrome and HVOF coated rods under conditions of short stroke reciprocating motion, Sealing Technology 2008(11) (2008) 9-14.

[7] D.G. Bhosale, W.S. Rathod, Tribo-behaviour of APS and HVOF sprayed WC–Cr3C2–Ni coatings for gears, Surface Engineering 37(1) (2021) 80-90.

[8] W. Karlsen, Fine-particle erosion and its incidence in pulp-handling components of the paper industry, Tribologia 25(2) (2006) 18-31.

[9] L. Vernhes, D.A. Lee, D. Poirier, D. Li, J.E. Klemberg-Sapieha, HVOF coating case study for power plant process control ball valve application, Journal of thermal spray technology 22(7) (2013) 1184-1192.

[10] R. Llewellyn, S. Yick, K. Dolman, Scouring erosion resistance of metallic materials used in slurry pump service, Wear 256(6) (2004) 592-599.

[11] R. Kumar, M. Kamaraj, S. Seetharamu, T. Pramod, P. Sampathkumaran, Effect of spray particle velocity on cavitation erosion resistance characteristics of HVOF and HVAF processed 86WC-10Co4Cr hydro turbine coatings, Journal of Thermal Spray Technology 25(6) (2016) 1217-1230.

[12] H. Wang, Y. Li, M. Gee, H. Zhang, X. Liu, X. Song, Sliding wear resistance enhancement by

controlling W2C precipitation in HVOF sprayed WC-based cermet coating, Surface and Coatings Technology 387 (2020) 125533.

[13] A.S. Praveen, J. Sarangan, S. Suresh, B. Channabasappa, Optimization and erosion wear response of NiCrSiB/WC–Co HVOF coating using Taguchi method, Ceramics International 42(1) (2016) 1094-1104.

[14] M. Nalbant, H. Gökkaya, G. Sur, Application of Taguchi method in the optimization of cutting parameters for surface roughness in turning, Materials & design 28(4) (2007) 1379-1385.

[15] X. Bie, J. Lu, Y. Wang, L. Gong, Q. Ma, Z. Ye, Optimization of parameters for deposition of Ga-doped ZnO films by DC reactive magnetron sputtering using Taguchi method, Applied surface science 257(14) (2011) 6125-6128.

[16] J.A. Picas, M. Punset, M. Teresa Baile, E. Martín, A. Forn, Tribological evaluation of HVOF thermal-spray coatings as a hard chrome replacement, Surface and interface analysis 43(10) (2011) 1346-1353.

[17] J.A. Picas, M. Punset, M.T. Baile, E. Martín, A. Forn, Properties of WC-CoCr Based Coatings Deposited by Different HVOF Thermal Spray Processes, Plasma Processes and Polymers 6(S1) (2009) S948-S953.

[18] J.A. Picas, M. Punset, M.T. Baile, E. Martín, A. Forn, Effect of oxygen/fuel ratio on the in-flight particle parameters and properties of HVOF WC-CoCr coatings, Surface and Coatings Technology 205 (2011) S364-S368.

[19] X. Zhang, F. Li, Y. Li, Q. Lu, Z. Li, H. Lu, X. Ran, X. Qi, Comparison on multi-angle erosion behavior and mechanism of Cr3C2-NiCr coatings sprayed by SPS and HVOF, Surface and Coatings Technology 403 (2020) 126366.

[20] K. Bobzin, L. Zhao, M. Öte, T. Königstein, M. Steeger, Impact wear of an HVOF-sprayed Cr3C2-NiCr coating, International Journal of Refractory Metals and Hard Materials 70 (2018) 191-196.

[21] W. Zhou, K. Zhou, C. Deng, K. Zeng, Y. Li, Hot corrosion behavior of HVOF-sprayed Cr3C2-WC-NiCoCrMo coating, Ceramics International 43(12) (2017) 9390-9400.

[22] V. Matikainen, G. Bolelli, H. Koivuluoto, P. Sassatelli, L. Lusvarghi, P. Vuoristo, Sliding wear behaviour of HVOF and HVAF sprayed Cr3C2-based coatings, Wear 388 (2017) 57-71.

[23] L. Janka, J. Norpoth, R. Trache, L.-M. Berger, Influence of heat treatment on the abrasive wear resistance of a Cr3C2NiCr coating deposited by an ethene-fuelled HVOF spray process, Surface and Coatings Technology 291 (2016) 444-451.

[24] G. Bolelli, L.-M. Berger, T. Börner, H. Koivuluoto, V. Matikainen, L. Lusvarghi, C. Lyphout, N. Markocsan, P. Nylén, P. Sassatelli, Sliding and abrasive wear behaviour of HVOF-and HVAF-sprayed Cr3C2–NiCr hardmetal coatings, Wear 358 (2016) 32-50.

[25] W.-c. Zhang, L.-b. Liu, M.-t. Zhang, G.-x. Huang, J.-s. Liang, L. Xian, L.-g. Zhang, Comparison between WC–10Co–4Cr and Cr3C2–25NiCr coatings sprayed on H13 steel by HVOF, Transactions of nonferrous metals society of china 25(11) (2015) 3700-3707.

[26] L. Lin, G.-L. Li, H.-D. Wang, J.-J. Kang, Z.-L. Xu, H.-J. Wang, Structure and wear behavior of NiCr–Cr3C2 coatings sprayed by supersonic plasma spraying and high velocity oxy-fuel technologies, Applied Surface Science 356 (2015) 383-390.

[27] M. Mathapati, M. Doddamani, M. Ramesh, High-Temperature Erosive Behavior of Plasma Sprayed Cr 3 C 2-NiCr/Cenosphere Coating, Journal of Materials Engineering and Performance 27(4) (2018) 1592-1600.

[28] J. Guilemany, N. Espallargas, P. Suegama, A.V. Benedetti, Comparative study of Cr3C2–NiCr coatings obtained by HVOF and hard chromium coatings, Corrosion science 48(10) (2006) 2998-3013.

[29] S. Liu, H. Wu, S. Xie, M.-P. Planche, D. Rivolet, M. Moliere, H. Liao, Novel liquid fuel HVOF torches fueled with ethanol: relationships between in-flight particle characteristics and properties of WC-10Co-4Cr coatings, Surface and Coatings Technology 408 (2021) 126805.

[30] A.L. Robertson, K.W. White, Microscale fracture mechanisms of a Cr3C2-NiCr HVOF coating, Materials Science and Engineering: A 688 (2017) 62-69.

[31] E.L. Cantera, B. Mellor, Fracture toughness and crack morphologies in eroded WC–Co–Cr thermally sprayed coatings, Materials Letters 37(4-5) (1998) 201-210.

[32] V. Matikainen, G. Bolelli, H. Koivuluoto, P. Sassatelli, L. Lusvarghi, P.J.W. Vuoristo, Sliding wear behaviour of HVOF and HVAF sprayed Cr3C2-based coatings, 388 (2017) 57-71.

[33] G. Bolelli, L.-M. Berger, T. Börner, H. Koivuluoto, L. Lusvarghi, C. Lyphout, N. Markocsan, V. Matikainen, P. Nylén, P. Sassatelli, Tribology of HVOF-and HVAF-sprayed WC–10Co4Cr hardmetal

coatings: A comparative assessment, Surface and Coatings Technology 265 (2015) 125-144.

[34] M. Mohanty, R. Smith, M. De Bonte, J.-P. Celis, E. Lugscheider, Sliding wear behavior of thermally sprayed 75/25 Cr3C2/NiCr wear resistant coatings, Wear 198(1-2) (1996) 251-266.

Chapter 5 Evolution of the torch: Switching from HVOF to HVOAF

5.1 Introduction

In recent years, Ni/Co-based alloys and coatings have been widely employed for marine power systems and the other engineering components due to their excellent mechanical properties and corrosion resistance [1, 2]. MCrAlY coatings (M = Ni, Co or NiCo) are usually employed as common top/bond layers to protect the parts from deterioration. The doping with rare metals, such as Ta, Hf and Re, is known to improve the oxidation resistance and corrosion resistance of the coating [3, 4]. The NiCoCrAlYTa coatings mainly contain FCC-structure γ-Ni matrix phase, ordered FCC-structure γ′-Ni_3Al and BCC-structure β-NiAl precipitates [5]. γ-Ni has a larger solid solubility, and Co and Cr atoms can dissolve into the matrix phase to reduce the propagation of dislocations thanks to a solution strengthening effect [6]. The intermetallic compound of β-NiAl displays higher strength and lower plasticity than the γ′-Ni_3Al phase. The latter is the main strengthening phase of the coating, which presents good plasticity and usually coexists with γ-Ni phase [7]. In addition, most of the elements of the alloy can contribute to the formation of a passive film on the surface to block the corrosion of the metal [8], especially the element Cr and Ta. Hence, the alloy offers a balanced combination of mechanical properties and corrosion resistance which makes it suitable for applications requiring a high resistance to corrosive and wear.

In this chapter, a new HVOAF system was devised and constructed starting from the original eGun HVOF system, by introducing a secondary combustion chamber to inject compressed air. NiCoCrAlYTa coatings were deposited on stainless steel substrates both using the eGun HVOF and the eGun HVOAF devices. The aim of this study is to investigate the influence of different compressed air flow rate on the evolution of microstructures and properties of NiCoCrAlYTa coatings deposited with the original and the modified torch. We also compared the microstructures and the relevant properties of the coatings prepared by eGun HVOAF and the HVOF. It is expected that this research will provide a valuable guidance for understanding the characteristics and applications of the new HVOAF technology.

5.2 Calculation of the combustion temperature of ethanol in the combustion chamber

One of the benefits of ethanol as a fuel is that it can be diluted to reduce the flame temperature. Therefore, it is possible not only to add gas to the spray gun of the HVOF torch, but also to add water to the ethanol, in order to increase the particle speed and reduce the particle temperature. Since the root objective is to reduce the flame temperature, this section is devoted to the calculation of the combustion temperature of ethanol in the combustion chamber, with and without (i) the addition of air and/or (ii) the incorporation of water in ethanol. The calculation is based on the equation of the enthalpy balance. The combustion temperature is not adiabatic because some heat is extracted from the eGun flame by the cooling water circuit; however, the amount of this heat extraction can be easily quantified from the flow rate, the inlet and outlet temperatures of the flow rate of the cooling water.

The composition of the "original ethanol" (i.e. the ethanol as procured) is: 93% ethanol + 1.5% 2 - butanone + 1.5% Isopropanol + 4% H_2O (by weight). This mass-based composition corresponds to the molar composition defined by the following coefficients: "e" (for ethanol), "b" (for butanone), "i" (for i-propanol) and "h" (for H_2O); these coefficients are used as the stoichiometric coefficient of the combustion equation (Eq. (1) below). In some of our experiments, we have diluted the original ethanol by adding some pure water in it. Consequently, the ethanol which is actually injected results different from the "original ethanol" in terms of its hydration degree: therefore, it will be distinctively called "the ethanol fuel". The amount of water, when added, is defined by the stoichiometric coefficient "w" in Eq (1). The molar composition of the air is denoted as ($1\ O_2 + n\ N_2$), where the coefficient "n" equals 3.76 and corresponds to the normal air composition (i.e.: 21% O_2 – 79% N_2). The excess of oxygen in the combustion is defined by the coefficient "λ" which is precisely called the "air excess coefficient". The value $\lambda = 1$ corresponds to the stoichiometric combustion, for which the amount of combustion air used is just necessary and sufficient to completely oxidize the fuel into CO_2 and H_2O. The molar amount of nitrogen which is potentially mixed with the

combustion air to reduce the flame temperature and including also the nitrogen used as the powder injection vector, is noted " n' " and must not be confused with "n". The number of moles of fuel burned per minute is noted "N_{fuel}".

Assuming the ethanol fuel is completely burned, the combustion process is summarized by equation (1). The thermal energy generated by the combustion of the fuel minus the energy taken away by the cooling water is the energy used to heat the combustion products from the ambient temperature to the final temperature. The combustion temperature is calculated according to equation (2) that expressed the conservation of energy.

$$(eC_2H_6O + i\,C_3H_8 + b\,C_4H_8O + h\,H_2O) + w\,H_2O + o\,\lambda\,(O_2 + n\,N_2) + n'N_2$$
$$\longrightarrow c\,CO_2 + (h' + w)\,H_2O + (o * \lambda * n + n')\,N_2 + o\,(\lambda - 1)\,O_2 \qquad (1)$$

$$LHV(fuel) - w\,Lv(H_2O) - \frac{m_{H_2O}Cp_{H_2O}\Delta T_{H_2O}}{N_{fuel}} = \int_{To}^{Tc}\sum niCpidT$$
$$= \int_{0}^{Tc}\sum niCpidT - \int_{0}^{To}\sum niCpidT \qquad (2)$$

where LHV(fuel) is for the "Low Heating Value" of the fuel; Lv(H_2O) is for the latent vaporization heat of water, i.e. the fraction of the heating value required to heat vaporize water; Tc is the combustion temperature and To is the room temperature (25°C). On has to note that the LHV(fuel) data includes the latent heat of vaporization of ethanol.

The main parameters that influence the combustion temperature of the ethanol fuel are therefore:

- w: the molar amount of water potentially added to the original ethanol

- λ: the "air excess coefficient" which characterizes the excess of air used to perform the combustion

- n': the molar of nitrogen potentially added to the combustion air (plus the nitrogen used as powder vector); to simplify the calculation, this value is initially taken equal to 0.

The ranges of these parameters we have explored in our experiments, are shown in Table 5.1 below. The notation "5% H_2O" means that 100 g of the "ethanol fuel" contain 5 g of pure water.

Table 5.1 The variation range of some coefficients in the equation

w	λ	n
0.121(5%H2O)	1	0
0.243(10%H2O)	1.25	0
0.364(15%H2O)	1.5	0
0.486(20%H2O)	1.75	0
0.607(25%H2O)	2	0

The calculation leads to the following obvious trends that are illustrated in Fig. 5.1:

- As the added air increases, the temperature of the chamber is considerably reduced.

- Similarly, as the amount of water added to the original ethanol increases, the temperature of the chamber also decreases.

These data indicate that adding either air to the combustion chamber or water to the ethanol has a powerful reduction effect on the temperature of the combustion chamber, which in turn will significantly affects the in-flight behavior (temperature, speed) of the flying particles and, ultimately, the structure and mechanical properties of the resulting coatings. It has been observed that adding air allows a stronger reduction of the temperature without causing a major degradation of the quality of combustion. This result is very important as it stresses the interest of a HVOAF device. Consequently, our study will focus on the effect of injecting variable amounts of secondary air in our novel ethanol fueled HVOAF device.

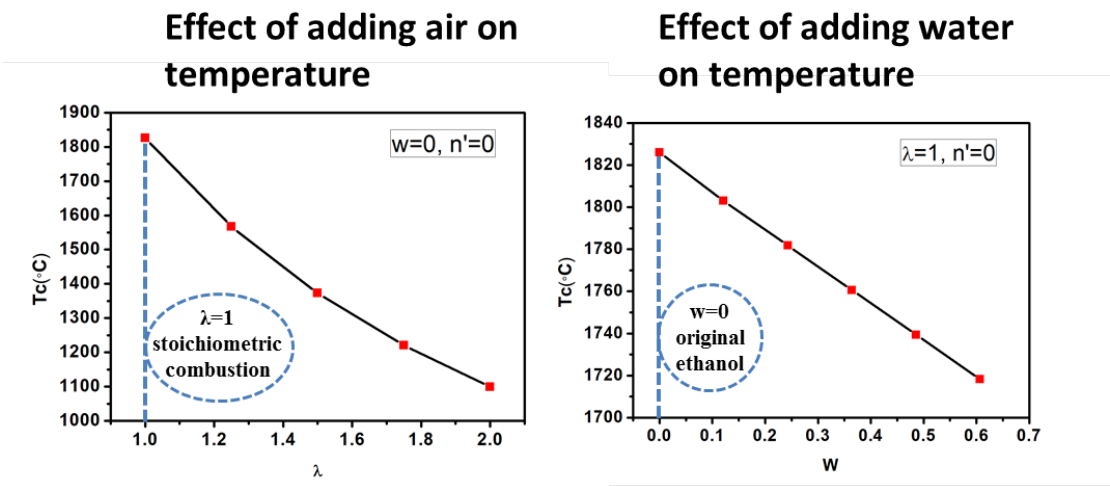

Fig. 5.1 The effect of adding air and water on temperature

5.3 Design of the modified torch: "Convert HVOF to HVOAF"

HVOF is a thermal spray system utilizing the combustion of gases, such as hydrogen, propane or a liquid fuel such as kerosene. This process creates a very high velocity which is used to propel the particles at near supersonic speeds before impacting onto the substrate. One of the fundamental rules of spraying is that the higher the combustion pressure, the greater the gas velocity, and the higher the particle velocity, which generally leads to higher coating quality. Even though this process results in relatively low particle oxidation, it is highly desirable to decrease the flame temperature and increase the velocity to obtain coatings with still higher quality.

This is the reason why this part of our work was intended to transform the initial eGun HVOF torch to an eGun HVOAF one. In fact, our original idea was to use compressed air instead of oxygen to lower the flame temperature and increase the velocity. Some attempts were carried out to add compressed air directly to the oxygen inlet of the initial eGun HVOF torch. However, our tests showed that the flame became extremely unstable and extinguished easily due to that direct introduction. Therefore, a modification of the internal design of the initial torch appeared necessary. The "gun renovation plan" consisted in adding a "second-stage" combustion chamber in series with the first-stage combustion chamber. The design schematic is shown in Fig. 5.2. After ethanol is stably burned with oxygen in the first-stage combustion chamber, the combustion products are subsequently mixed with some added compressed air in the second-stage combustion chamber, from which they are propelled into the barrel, before leaving the torch. The detailed schematic of the modified torch is shown in Fig. 5.3. After a number of experimental adjustments, compressed air was successfully introduced into the spray gun, which showed the feasibility of the planned transformation, giving rise to a new "eGun HVOAF device".

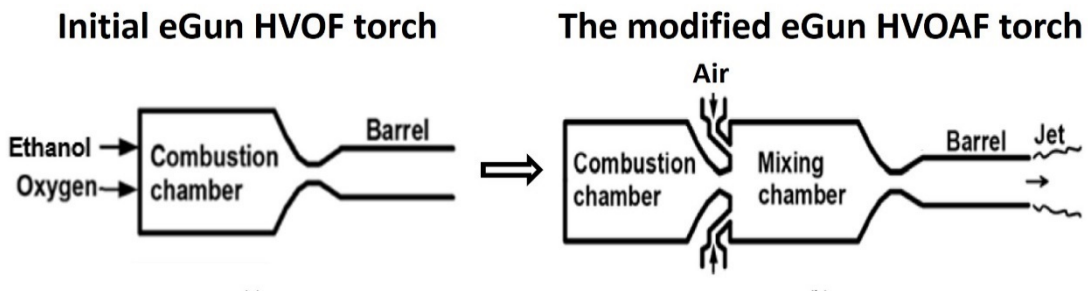

Fig. 5.2 The design schematic of the torch

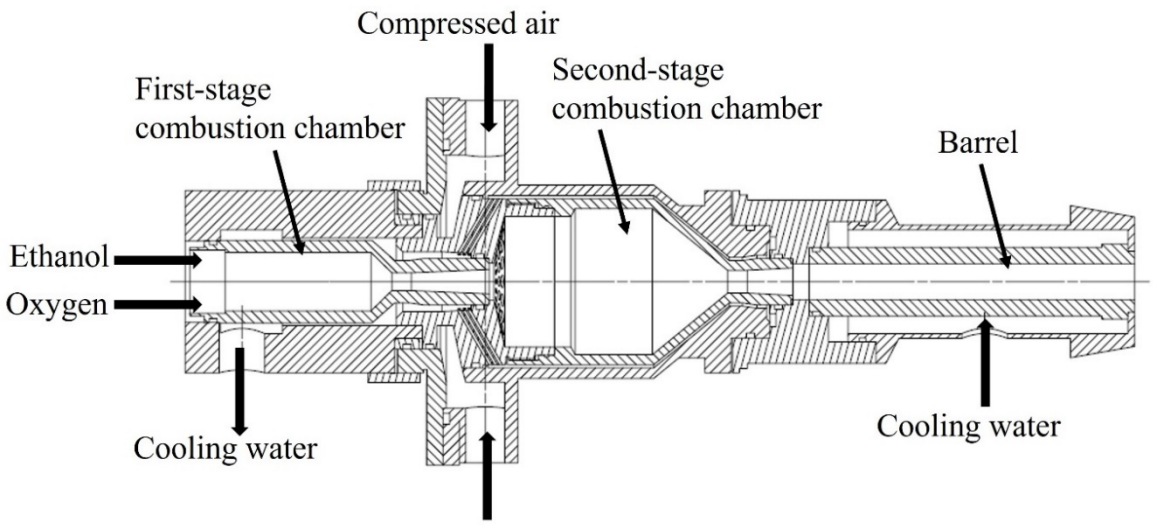

Fig. 5.3 The schematic of the modified eGun HVOAF torch

5.4 Performance of the HVOAF torch: Microstructure and properties of NiCoCrAlYTa coatings

5.4.1 Preparation conditions of NiCoCrAlYTa coatings

NiCoCrAlYTa coatings were prepared using the ethanol-fueled HVOAF device obtained as set out above. At first, a study was undertaken to optimize the parameters of this new process for depositing NiCoCrAlYTa coatings. Then, investigations were conducted to determine the influence of different flow rates of compressed air on the evolution of the microstructures and the properties of the resulting NiCoCrAlYTa coatings. Some preliminary experiments led to select the set of spraying parameters shown in Table 5.2. In order to focus on the influence of the standoff distance and compressed air flow rate on the properties of the coatings, the ethanol

flow rate, oxygen flow rate and powder feeding rate were kept constant. We defined three levels of standoff distance, respectively 200, 250, and 300 mm; The air flow rate was also assigned three levels, respectively, 200, 400, and 600 slpm. The coating numbers obtained in the corresponding experiments are E1 to E9. The coating E10, deposited using the original eGun HVOF process was intended as a reference. The parameters for depositing coating E10 have been the result of preliminary optimization, after which the coating E10 has been compared with NiCoCrAlYTa coatings prepared by the HVOAF process.

Table 5.2 Spraying parameters and corresponding properties of NiCoCrAlYTa coatings

Test	C_2H_6O (slph)	O_2 (slpm)	air (slpm)	Distance (mm)	Feed rate (g/min)	Porosity (%)	Microhard. ($HV_{0.3}$)
E1	24	400	200	200	68	0.15±0.02	539±15
E2	24	400	200	250	68	0.23±0.02	433±23
E3	24	400	200	300	68	1.84±0.16	363±15
E4	24	400	400	200	68	0.05±0.008	549±17
E5	24	400	400	250	68	0.16±0.02	466±16
E6	24	400	400	300	68	0.38±0.03	409±8
E7	24	400	600	200	68	0.78±0.10	579±32
E8	24	400	600	250	68	1.50±0.17	494±22
E9	24	400	600	300	68	2.44±0.57	450±26
E10	24	480	0	270	68	0.17±0.02	482±28

5.4.2 Optimization of the standoff distance and compressed air flow rate

The results in terms of coating porosity obtained under different standoff distances and air flow rates are shown in Fig. 5.4. It can be found that with the same air flow rates, the porosity of the coatings increases significantly as the standoff distance increases. When the standoff distance is 200 mm, the porosity of the coating associated with the three levels of air flow rate stays at low values, all the values being lower than 1%. However, when the standoff distance is fixed and the air flow rate is increased from 200 slpm to 600 slpm, the porosity of the coating first decreases and then increases significantly. From these results, it seems that a lower porosity of the coating is obtained when the air flow is 400 slpm.

The evolution of the coating microhardness under different standoff distances and air flow rates is shown in Fig. 5.5. The microhardness of the coatings decreases when increasing the

standoff distance, when the air flow rate is kept constant. When the standoff distance is adjusted and kept at 200 mm, the microhardness of the coatings is higher than 500 HV0.3. When the standoff distance is fixed, the microhardness of the coatings also increases to a certain extent with the air flow (from 200 slpm to 600 slpm).

Therefore, it appears that the coating has a lower porosity and a higher microhardness with a standoff distance of 200 mm. In order to investigate the impact of the air flow rate on the structure and performance of NiCoCrAlYTa coatings, and compare them to those of coatings obtained with the original eGun HVOF process, the subsequent part of our work has focused on the microstructure and properties of the coatings E10, E1, E4, and E7. E10 is the coating obtained without air addition, marked as “coating-no air”. E1 is that with an air flow rate of 200 slpm, marked as “coating-air 200”. E4 is that with an air flow rate of 400 slpm, marked as “coating-air 400”. Finally, E7 is that with an air flow rate of 600 slpm, marked as “coating-air 600”.

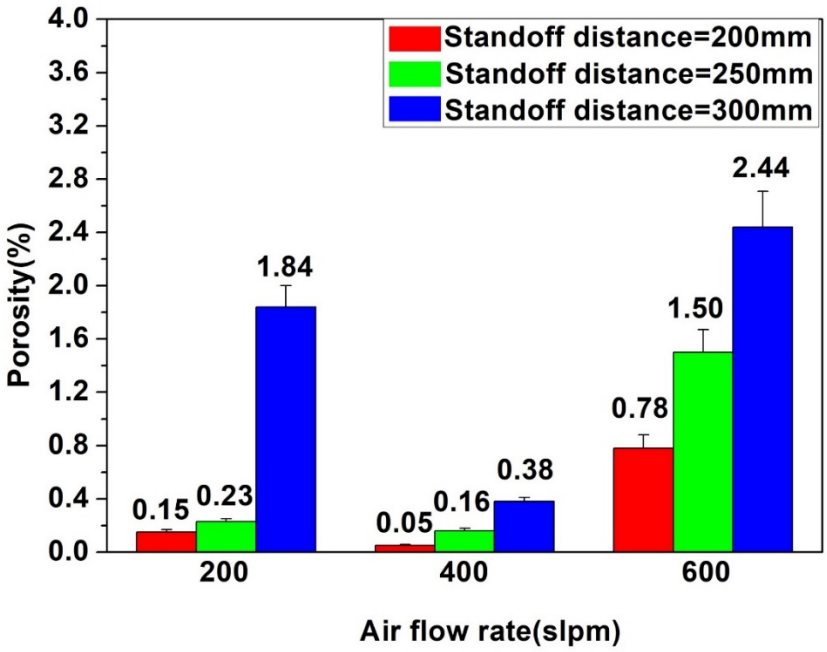

Fig. 5.4 Porosity of coatings vs standoff distance and air flow rate

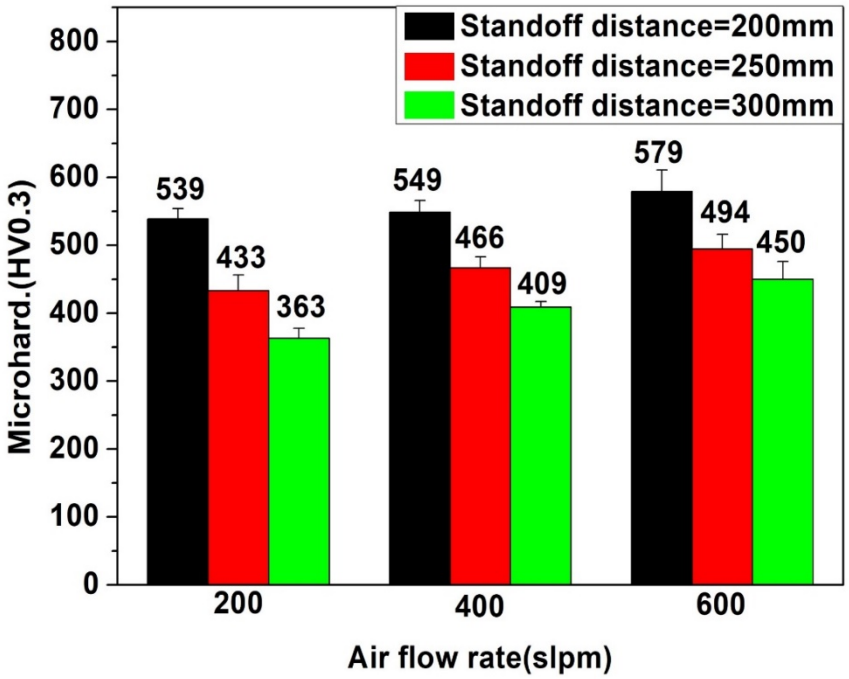

Fig. 5.5 Microhardness of the coatings vs standoff distance and air flow rate

5.4.3 Phase composition and microstructure of the NiCoCrAlYTa coatings

The XRD pattern of the as-received NiCoCrAlYTa powder is shown in Fig. 2.6 in Chapter 2. It is mainly composed of γ-Ni, β-NiAl and γ′-Ni_3Al phases, which have a good crystallinity. The XRD patterns of the sprayed NiCoCrAlYTa coatings with different air flow rates are shown in Fig. 5.6. One sees that the as-sprayed NiCoCrAlYTa coatings exhibit a phase composition similar to that of the as-received powders. This indicates that the powder remains stable during the deposition process. Nonetheless, the diffraction peaks of the four NiCoCrAlYTa coatings at 2θ angles of 53°, 60°, and 90 °are obviously broader and weaker compared to the powder. This may be attributed to the severe plastic deformations and the large temperature difference which occur when the powder particles impact on the substrate at a high speed. As a result, some grains in the coating are insufficiently grown, resulting in the formation of microcrystals or incomplete crystals. In addition, it is known that parts of the crystal lattice of the grains in the splats are disordered due to greater impact [9, 10].

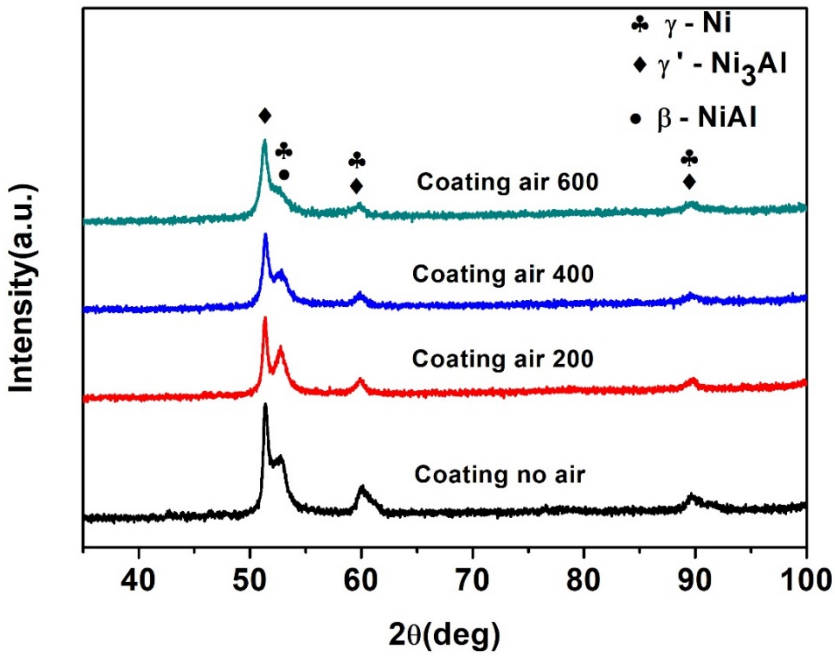

Fig. 5.6 XRD patterns of the as-sprayed NiCoCrAlYTa coatings

5.4.4 Microstructures

Fig. 5.7 displays the top surface morphologies of the sprayed NiCoCrAlYTa coatings with different air flow rates. It reveals that large-area splats spread out with each other on the surface of the coating-no air, as shown in Fig. 5.7(a). It implies that the NiCoCrAlYTa powder has been completely melted and well deposited on the 304 stainless steel substrates under the spraying conditions used. In the enlarged Fig. 5.7(b), it can be found that there a large number of fine particles lie around the splats generated by the splashing of the molten powders. Fig. 5.7(c) and (d), indicate that a portion of the molten powder and splashed fine particles are also present on the surface of the coating-air 200. At the same time, unmelted and semi-melted powders were also observed. This is because the increase up to 200 slpm of the air flow leads to an important decrease in the flame temperature, which results in a poorer powder melting. In Fig. 5.7(e), it is difficult to find a large area of molten powder on the surface of the coating-air 400. On the contrary, there are more unmelted and semi-melted powders. Some flat powders are also observed in Fig. 5.7(f). Moreover, the surface morphology of the coating-air 600 is

similar to that of coating-air 400, as shown in Fig. 5.7(g) and (h). Due to the large increase in air flow, the flame temperature is greatly reduced, resulting in a poor melting effect. The presence of some flat powders is due to the larger airflow increasing the particle velocity, combined with a certain particle temperature, resulting in greater plastic deformation when it impacts the substrate.

The elemental compositions of the top surface of the feedstock powder and NiCoCrAlYTa coatings were analyzed by EDS, and the results are listed in Table 5.3. The actual chemical composition of the as-received powder is 44.09 wt% Ni, 23.39 wt% Co, 21.21 wt% Cr, 6.77 wt% Al, 0.50 wt% Y, 4.05 wt% Ta, which is almost equivalent to its theoretical value of Ni-23Co-20Cr-8.5Al-4Ta-0.6Y. Furthermore, some oxygen is identified in the sprayed coating-no air, and the content of Ni, Co, and Cr is slightly reduced, while the other element proportions are identical to those of the NiCoCrAlYTa powders. The reason is that the powder particles are partially oxidized during the HVOF spraying process. Paradoxically, the other three coatings prepared with additions of air have substantially lower oxygen content, implying relatively less oxidation during HVOAF spraying process. This is due to the fact that the addition of air flow reduces the temperature of the flame and increases the velocity of the particles, resulting in a shorter stay in the flame during the spraying process.

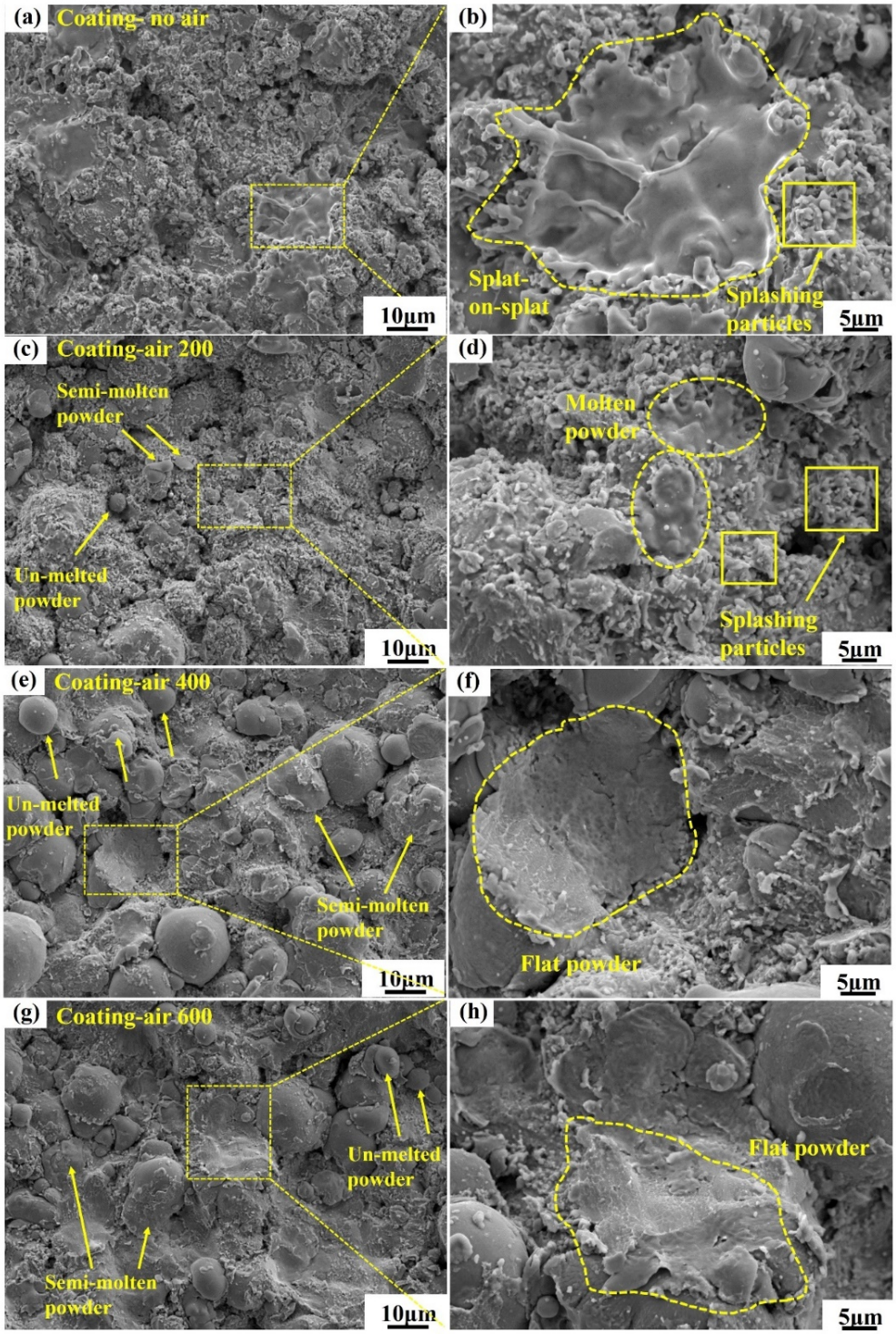

Fig. 5.7 SEM images of the top surface of the as-sprayed NiCoCrAlYTa coatings. (a) and (b): coating-no air; (c) and (d): coating-air 200; (e) and (f): coating-air 400; (g) and (h): coating-air 600

Table 5.3 Elemental compositions of the top surface of the as-received powder and NiCoCrAlYTa coatings

Samples	Element composition/wt%							
	Ni	Co	Cr	Al	Y	Ta	O	C
As-received powder	44.09 ±0.33	23.39 ±0.21	21.21 ±0.34	6.77 ±0.15	0.50 ±0.47	4.05 ±0.51	-	-
Coating-no air	37.60 ±0.21	20.79 ±0.93	17.64 ±0.10	6.99 ±0.18	0.43 ±0.19	4.26 ±0.62	6.37 ±0.07	-
Coating-air 200	40.64 ±0.16	22.30 ±0.09	19.05 ±0.06	6.75 ±0.45	0.41 ±0.09	4.89 ±0.33	2.60 ±0.29	-
Coating-air 400	41.01 ±1.46	21.13 ±0.02	19.25 ±0.06	6.32 ±0.25	0.35 ±0.02	5.87 ±1.51	2.19 ±0.08	-
Coating-air 600	39.36 ±0.82	20.75 ±0.32	18.73 ±0.37	6.43 ±0.42	0.43 ±0.00	4.98 ±1.82	1.91 ±0.18	-

Fig. 5.8 exhibits some SEM micrographs of the cross-section of the NiCoCrAlYTa coatings. All four coatings prepared with different air flow rates are dense and uniform. The sprayed “coating-no air” has a distinct layered structure that is typical of HVOF deposited coatings. This is attributed to the fact that the coating is gradually deposited by the close stack of splats. The high magnification image in Fig. 5.8(b) shows that it has a typical splat-on-splat structure with a small number of pores, as well as some darker strip-shaped areas. No such layered structures and darker strip-shaped areas were found in the other three coatings prepared with varying amounts of air. Unmelted powder, semi-melted powder and a small number of pores were observed in the cross-sectional view of the coating-air 200, as shown in Fig. 5.8(d). In addition, it can be seen in Fig. 5.8(f) and (h) that some flat particles, a few pores, and a few micro-cracks appeared in the cross-sectional view of the coating-air 400 and coating-air 600. These features are consistent with the surface morphologies of the coatings in Fig. 5.7.

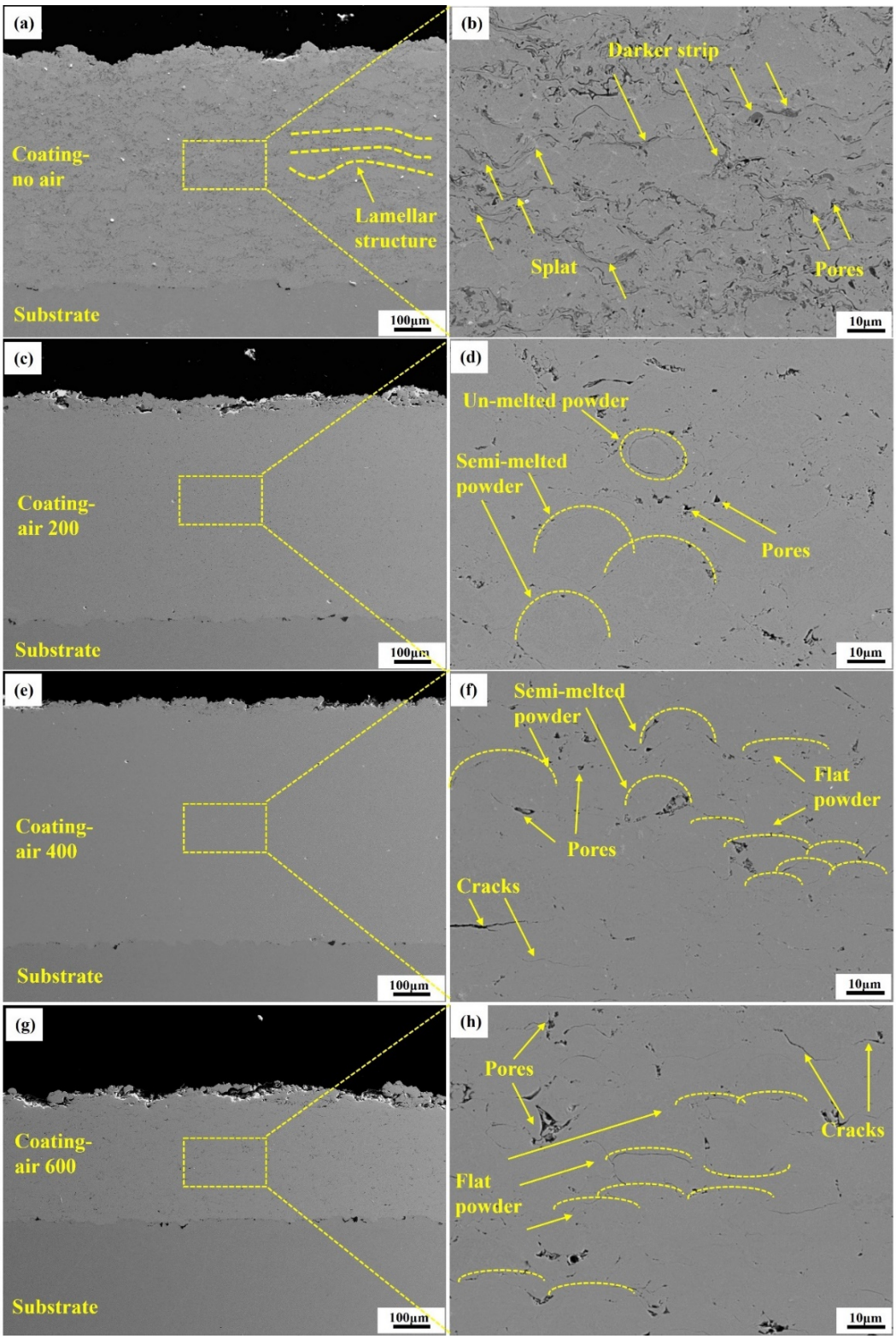

Fig. 5.8 SEM images of cross-section of the as-sprayed NiCoCrAlYTa coatings. (a) and (b): coating-no air; (c) and (d): coating-air 200; (e) and (f): coating-air 400; (g) and (h): coating-air 600

Fig. 5.9 presents the HRSEM image and element mappings of a cross-section of the coating-no air, as well as the EDS analyses of some points that are marked in Fig. 5.9 (a). The microstructure contains precipitates and matrix phases, as shown in Fig. 5.9(a). Furthermore, the results of the element mapping in Fig. 5.9(b) show that the majority of the elements, i.e. Ni, Co, and Cr, are evenly distributed, but Al is partially concentrated in the dark area dominated by precipitates, where the oxygen content is also higher. The EDS analysis in Fig. 1.6(c), (d) and (e) confirm that the point 3 has a relatively high oxygen content, contrary to points 1 and 2 that contain much less oxygen. This implies that the aluminum-rich area of the coating is slightly oxidized during the deposition process, resulting in a small amount of aluminum oxide. This is due to the oxidizing conditions which prevail in the HVOF process and the high affinity of aluminum for oxygen. In addition, the oxidized zones are primarily distributed at the boundaries of the splats. This is consistent with the microstructure characteristics of other HVOF sprayed NiCoCrAlYTa coatings, as reported by Hao et al. [11].

Fig. 5.10 shows the HRSEM image and element mappings of a cross-section of the coating-air 400, and the EDS results of some points marked in Fig. 5.10(a). It can be found that there are no obvious precipitates in Fig. 5.10(a). All elements displayed in Fig. 5.10(b), including Al and O are uniformly distributed in the coating, and are not significantly concentrated in some areas. The EDS spectra taken at the 3 points show that the oxygen contents are extremely low, which also confirms that there is basically no oxidation process. Again, this is because the increase in air flow greatly reduces the flame temperature, thereby greatly reducing the oxidation of flying particles, due to the combination of low temperature and high HVOF spraying speed.

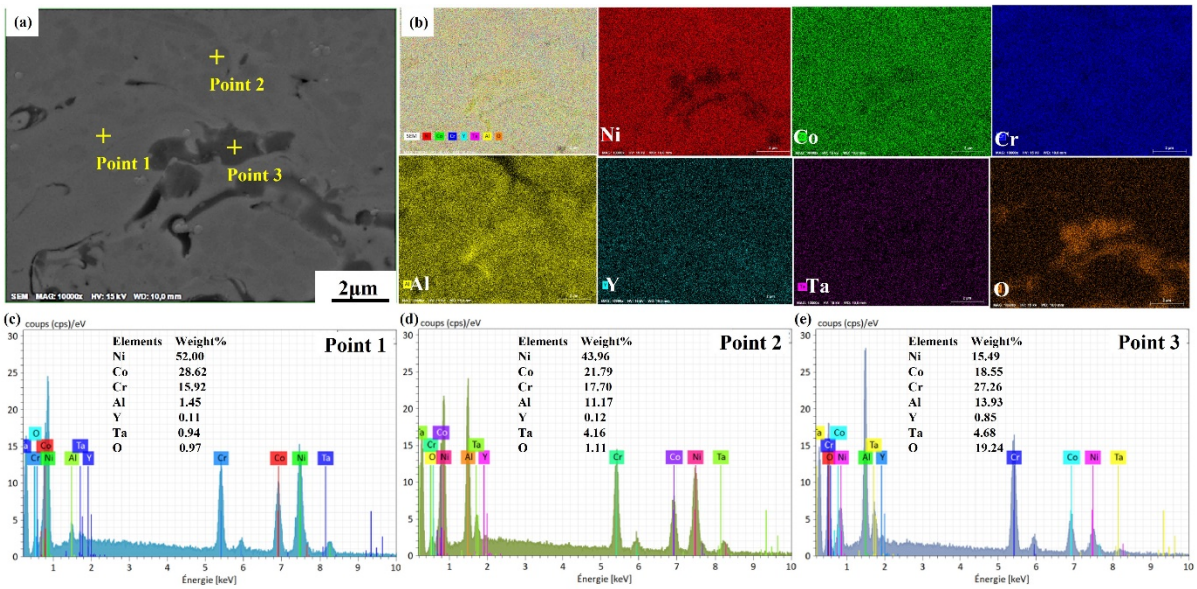

Fig. 5.9 SEM micrographs (a), and element mappings (b) of cross-section of the coating-no air; and EDS results of point 1 (c), point 2 (d), and point 3 (e) in the areas of Fig. 5.9 (a).

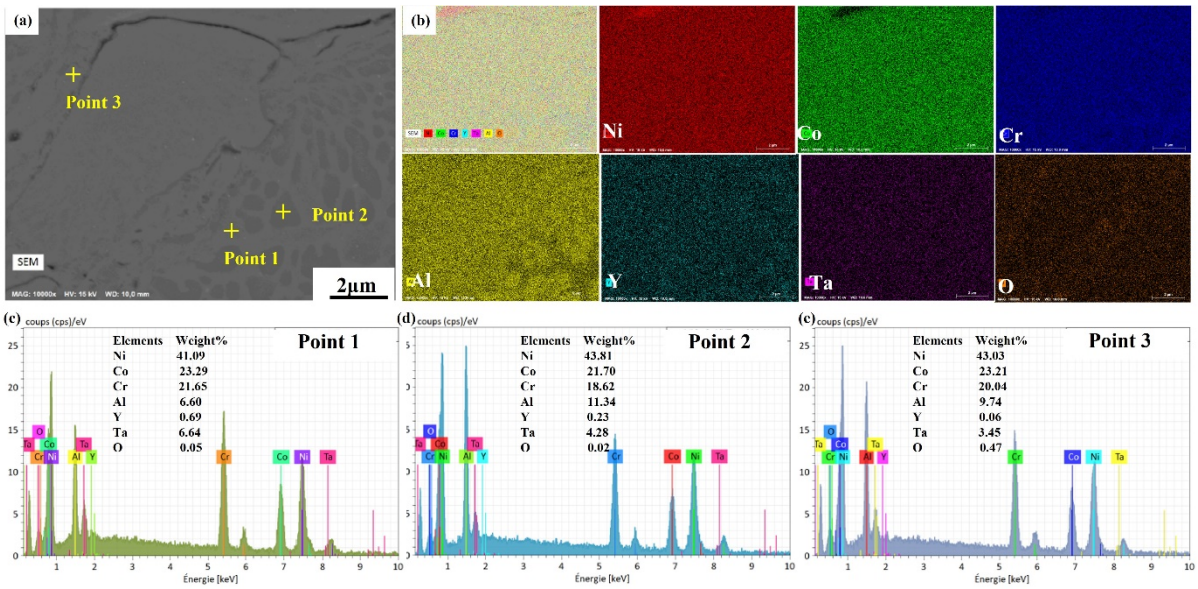

Fig. 5.10 SEM micrographs (a), and element mappings (b) of cross-section of the coating-air 400; and EDS results of point 1 (c), point 2 (d), and point 3 (e) in the areas of Fig. 2.10 (a).

5.4.5 Roughness and porosity

The roughness and porosity data of the NiCoCrAlYTa coatings obtained with various air flow rates are gathered in Fig. 5.11, as well as their standard deviation. As shown in Fig. 5.11(a),

the values of the surface roughness of the four coatings are distributed between 4.7-6.5. When the air flow rate increases, it also gradually increases due to the poorer melting of the powder particle. Furthermore, the porosity levels of the four coatings are all below 1% in Fig. 5.11(b), indicating that all coatings are dense. This may be due to the favorable particle temperature and particle velocity of the eGun HVOF and eGun HVOAF processes. When the air flow rate increases from 200 slpm to 600 slpm, the porosity of the coating decreases slightly, and then increases significantly to 0.78%. This is due to the fact that an increase in air flow speeds up the particle but also reduces their temperature. Only a proper range of air flow can favor the low porosity levels.

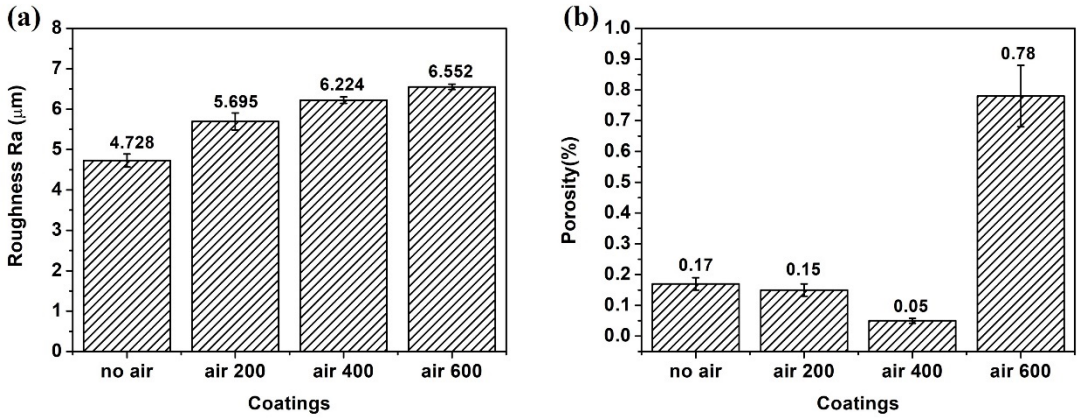

Fig. 5.11 The roughness (a) and porosity (b) of as-sprayed NiCoCrAlYTa coatings

5.4.6 Bonding strength

Fig. 5.12 gathers the results of the bonding strength tests of the of NiCoCrAlYTa coatings prepared with different air flow rates. All the tensile tests carried out on the coating-no air fractured at the position of the used glue. Therefore, the bonding strength of coating-no air is greater than 68MPa, which is the nominal strength value of the glue. In contrast, the fractures of the other three coatings all occurred inside the coating during the tensile tests. The bonding strength of the coating-air 200 is 67.7MPa, which is lower than that of the coating-no air. Those of the coating-air 400 and coating-air 600 are 53.5 and 51.5 MPa, respectively. Overall, although the bonding strength significantly decreases when increasing the air flow, the values stay at a fairly good level. Generally speaking, the greater the plastic deformation of the flying

powder particles when they hit the substrate, the higher the cohesive strength between the splats and consequently the higher the bonding strength of the resulting coating. The temperature and velocity of the flying particles together affect their plastic deformation as they impact on the substrate. On the one hand, increasing the air flow enhances the velocity of the particles i.e. their kinetic energy, which intensifies the plastic deformations when impacting the substrates. On the other hand, it lowers their temperature, which leads to less deformable particles at the impacts, so the coatings bonding strength decrease s slightly. This result indicates that the effect of the increase in particle speed produced by a higher air flow is insufficient to compensate for the poorer melting of the particles.

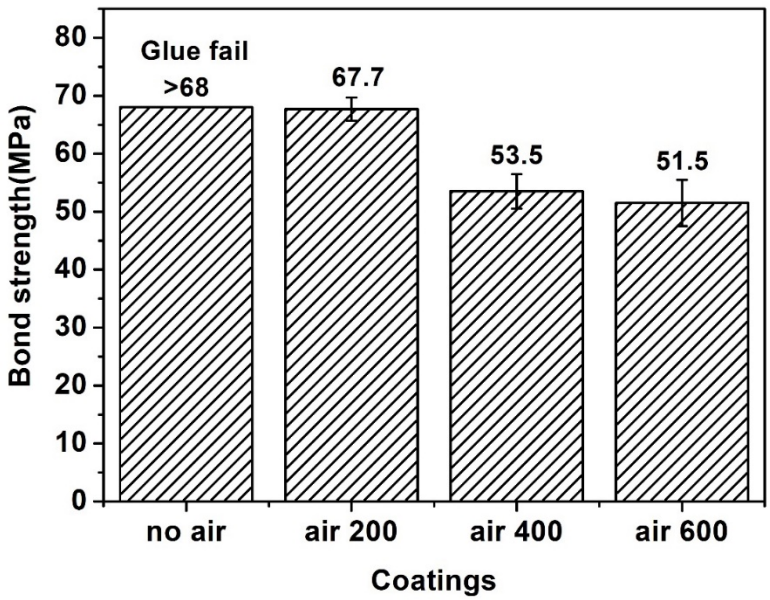

Fig. 5.12 The bonding strength of the four as-sprayed NiCoCrAlYTa coatings

5.4.7 Microhardness and nano-microhardness

Fig. 5.13 shows the microhardness, nano-hardness (HIT) and elastic modulus (EIT) measured on cross-sections of the as-sprayed NiCoCrAlYTa coatings prepared while varying the air flow rate. It can be seen in Fig. 5.13(a) that the coating-no air has the lowest microhardness of 482 HV0.3. As the air flow rate increases, the microhardness of the coating gradually increases, from 482 HV0.3 to 579 HV0.3. Moreover, its nano-hardness follows a

similar evolution (Fig. 5.13(b)). It increases from 5.74GPa to 6.45GPa, when the air flow passes from 0 to 600 slpm. However, the elastic modulus exhibits a different trend. The coating-no air and coating-air 200 have elastic modulus of 238.1GPa and 231.2GPa, respectively. As indicated also in Fig. 5.13(b), the elastic modulus of coating-air 400 is the highest, at 244.7GPa, while that of coating-air 600 is the lowest, at 219.5GPa. It has been reported that the higher the hardness and elastic modulus, the better is the anti-wear property of materials [12]. Therefore, the increase in air flow rate is likely to be beneficial for the wear resistance of NiCoCrAlYTa coatings.

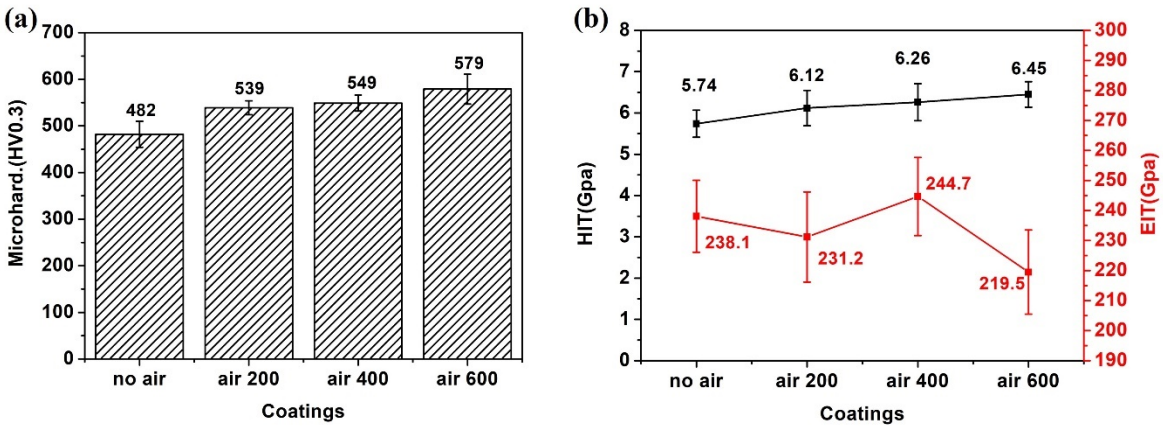

Fig. 5.13 The microhardness (a) and porosity (b) of the as-sprayed NiCoCrAlYTa coatings

5.4.8 Sliding wear tests of NiCoCrAlYTa coatings

The sliding wear tests of the as-sprayed NiCoCrAlYTa coatings against Al_2O_3 balls were conducted at room temperature. Fig. 5.14 shows the curves of the friction coefficient in function of the sliding distance. One observes that the friction coefficients of the four coatings become virtually stable after the run-in period at the beginning of the test. Fig. 5.15 displays the wear rate and average coefficients of friction of the four NiCoCrAlYTa coatings. The latter range from 0.58 to 0.66, which is consistent with the results of NiCoCrAlYTa coatings tested under similar conditions, as reported by Hao et al.[10, 13]. Moreover, the average friction coefficient of the coating-no air equals 0.58, which is slightly lower than that of the other three coatings prepared with air addition. This may be related to the increase in the roughness of the coating surface when using additional air. In addition, the wear rate of as-prepared coating

decays from $6.41\times10^{-4}mm^3\ N^{-1}m^{-1}$ to $3.03\times10^{-4}mm^3\ N^{-1}m^{-1}$ when the air flow rate rises from 0 up to 600 slpm. Hao et al. [13] studied the tribological behavior of the HVOF-sprayed NiCoCrAlYTa coatings and found that a wear rate of about $5.45\times10^{-4}mm^3\ N^{-1}m^{-1}$ under similar conditions, which fits well with the results of our investigations. As mentioned before, the wear rate of the coating is closely related both to its hardness (including micro-hardness and nano-hardness) and its elastic modulus. Higher coating hardness and elastic modulus help reduce the wear rate. As the air flow rate increases, both the micro- and nano-hardness of the coating increase. Although the elastic modulus of the coating-air 600 is slightly lower than that of the other three ones, its highest micro-hardness and nano-hardness result in the lowest wear rate.

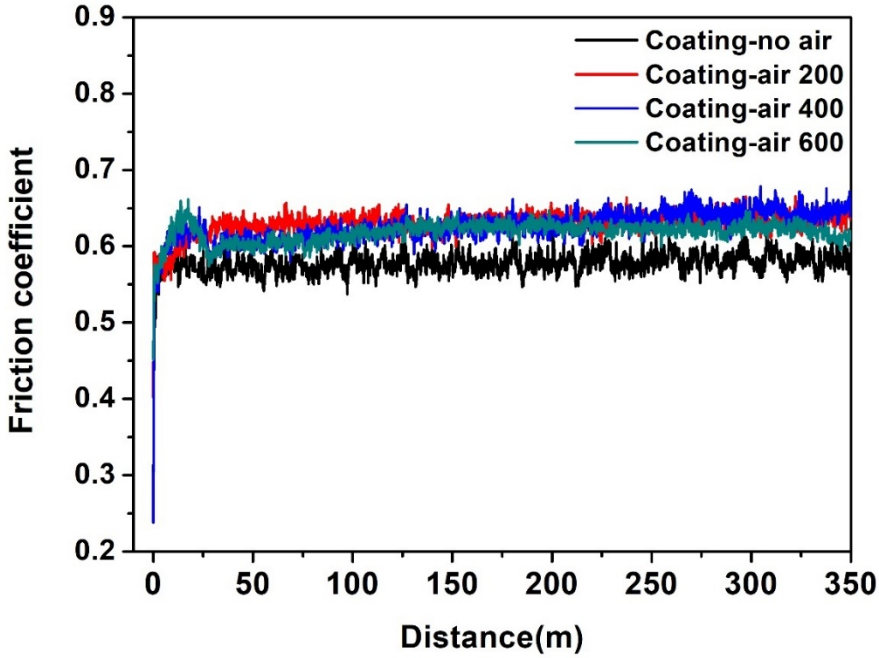

Fig. 5.14 Friction coefficient-distance curves of the as-sprayed NiCoCrAlYTa coatings

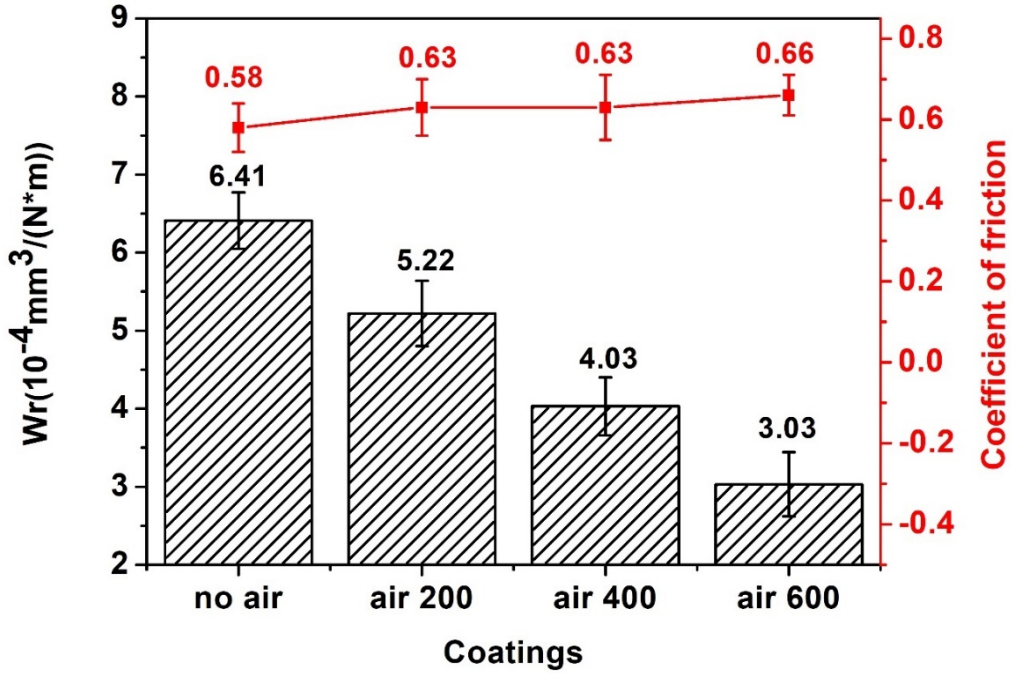

Fig. 5.15 The wear rates and average coefficients of friction of the as-sprayed NiCoCrAlYTa coatings

Fig. 5.16 presents the SEM images and 2D topographies of the wear tracks of the as-deposited NiCoCrAlYTa coatings. As indicated in Fig. 5.16(a-1), there are many parallel furrows in the wear track of the coating-no air, which is attributed to the hard abrasive particles formed during the friction process. Fig. 5.16(a-2) shows that traces of adhesive wear are also found on the coating-no air. It implies that the sprayed coating-no air experienced not only severe abrasive wear, but also adhesive wear. This phenomenon was also found by Hao et al. [13]. This interaction leads to a large increase in wear loss during the sliding friction process. As shown in Fig. 5.16(a-3), the wear track of the coating-no air is the widest and deepest, and the cross-sectional area of the wear scar is also the largest. As the air flow rate increases, the furrows of the coating wear scars gradually become less numerous and shallower, as shown in Fig. 5.16(b-1), (c-1) and (d-1). On the contrary, the signs of adhesive wear increase significantly. On the one hand, the addition of air increases the microhardness and nano-hardness of the coating, resulting in fewer furrows during the sliding wear. On the other hand, it lowers the

flame temperature, resulting in less oxidization of the coating, and thus adhesive wear is more likely to occur, becoming the predominant effect in these conditions. Some EDS analyses have been performed on some spots of each coating, which show adhesive and non-adhesive wear. These spots are marked in Fig. 5.16(a-2), (b-2), (c-2) and (d-2). The analyses results are gathered in Table 5.4; they confirm that the areas having experienced adhesive wear contains more oxygen than the other ones, implying that some oxides were formed in this area. This is because the wear debris generated during the repeated sliding of the coating surface underwent tribochemical reactions and generated oxides with a contribution of frictional stress and frictional heat.

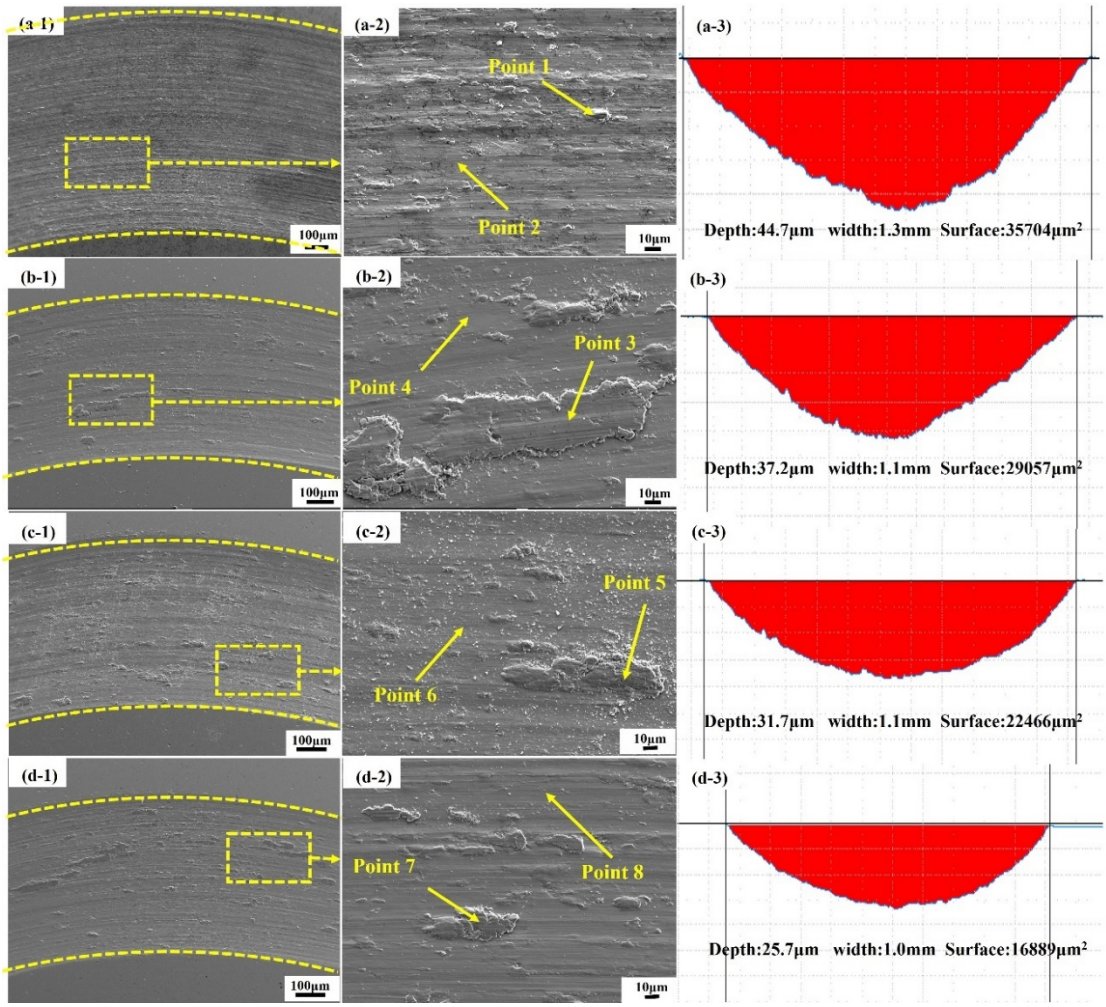

Fig. 5.16 The SEM images and 2D topographies of wear traces of (a-1), (a-2), and (a-3): coating-no air; (b-1), (b-2), and (b-3): coating-air 200; (c-1), (c-2), and (c-3): coating-air 400; (d-1), (d-2), and (d-3): coating-air 600

Table 5.4 EDS analysis of the points in Fig. 5.16

Point	Element composition(wt.%)						
	Ni	Co	Cr	Al	Y	Ta	O
1	30.23	17.64	21.25	11.67	0.71	5.71	12.79
2	42.44	23.94	18.74	9.58	0.58	3.7	1.01
3	33.31	19.28	17.99	10.44	0.74	4.46	13.78
4	40.81	22.99	19.63	10.09	0.2	5.01	1.28
5	38.34	20.41	18.42	8.61	0.25	5.03	8.94
6	41.56	23.09	19.77	8.25	1.25	5.44	0.63
7	35.31	18.87	16.78	7.98	0.16	3.02	17.67
8	40.53	23.06	21.83	7.46	0.87	5.72	0.51

The SEM images of the wear scars detected on the alumina ball counterparts corresponding to the four NiCoCrAlYTa coatings are illustrated in Fig. 5.17. It can be found that the wear scar morphologies of these alumina balls and the friction activity of the four NiCoCrAlYTa coatings are well correlated. The alumina balls matched with the coating-no air and coating-air 200 are subjected to more severe wear, as visible in Fig. 5.17(a) and (b). The alumina balls used with the coating-air 400 and coating-air 600 suffer lighter wear as shown in Fig. 5.17(c) and (d). This is in line with the anti-wear performance of the four NiCoCrAlYTa coatings. The wear morphology of the surface of the alumina balls results both from (i) the material transfers between the coating surface and the alumina counterpart during the sliding wear and (ii) the wear of the oxide formed on the wear surface of the coating due to the tribochemical reactions.

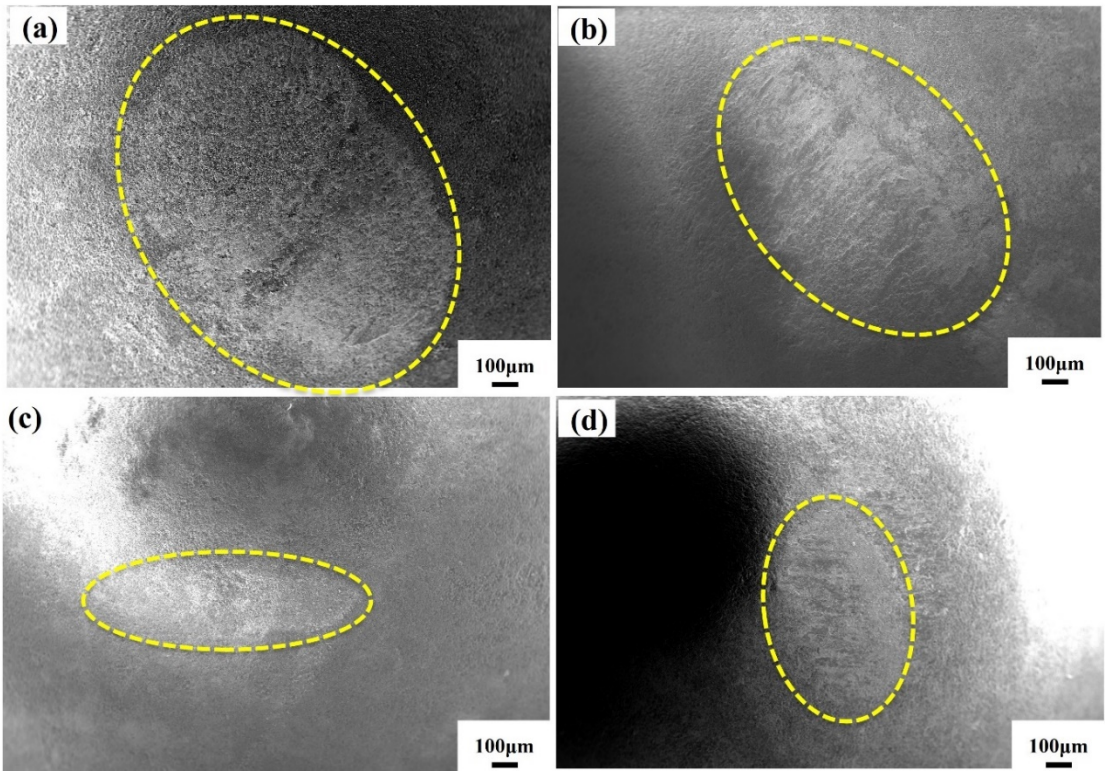

Fig. 5.17 SEM morphologies of some worn surfaces of the Al_2O_3 balls corresponding to (a) coating-no air; (b) coating-air 200; (c) coating-air 400; (d) coating-air 600

5.4.9 Electrochemical testing

The Tafel curves of the four NiCoCrAlYTa coating obtained in 0.1 M HCl solutions are reported in Fig. 5.18. The corrosion potential (Ecorr) and the corrosion current density (icorr) deduced using the Tafel extrapolation method are given in Table 2. Ecorr represents the corrosion susceptibility of the material from a thermodynamic standpoint: a higher Ecorr value indicates a lower corrosion tendency. Fig. 5.18 shows that the corrosion potential of the four coatings is almost the same, which means that their tendency to corrode is similar from the perspective of corrosion thermodynamics. In turn, the density of the corrosion current is a direct criterion for evaluating the corrosion resistance because its value is proportional to the corrosion rate of the tested sample. The values of icorr of the four coatings are quite similar: 3.39E-5 A/cm^2, 2.78E-5 A/cm^2, 2.34E-5 A/cm^2 and 1.16E-5 A/cm^2, respectively, as shown in Table 5.5. Despite this similarity of the icorr values, there exists a certain trend. As the air flow increases, the corrosion current density slightly and gradually decreases. This could be due to

the fact that the increased air flow reduces to some extent the degree of oxidation of the coating, making it more protective.

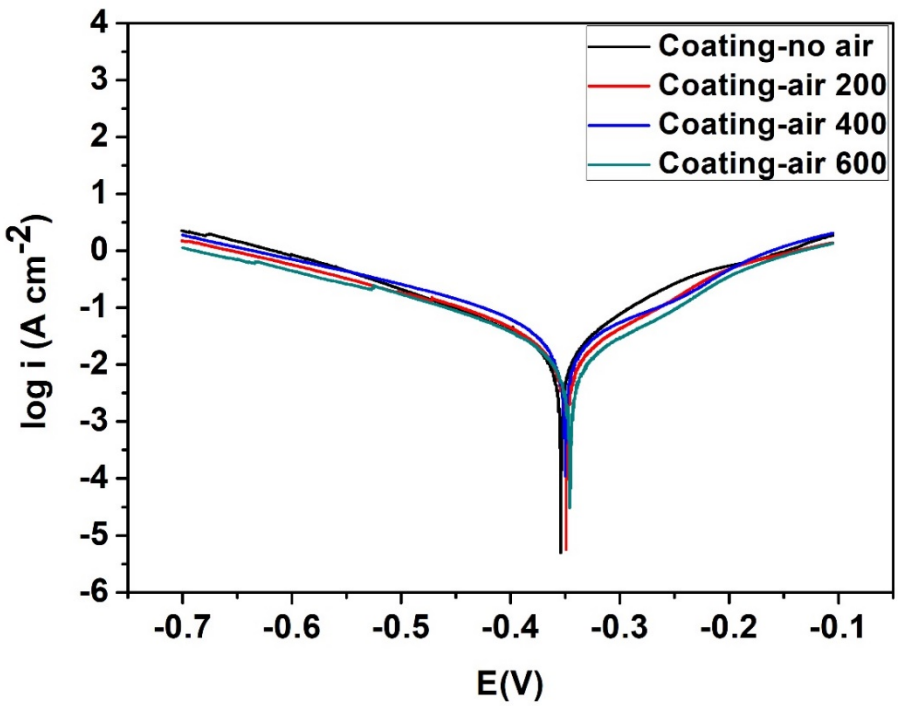

Fig. 5.18 Tafel curves of NiCoCrAlYTa coating in 0.1 M HCl solution

Table 5.5 Results from Tafel polarization of NiCoCrAlYTa coating in 0.1 M HCl solution

Samples	E_{corr} (V, vs.SCE)	i_{corr} (A/cm^2)
Coating-no air	-0.368	3.39E-5
Coating-air 200	-0.347	2.78E-5
Coating-air 400	-0.343	2.34E-5
Coating-air 600	-0.341	1.16E-5

5.5 Conclusions

The purpose of this part of our research work was to create a novel ethanol-fueled HVOAF device and carry out an extensive characterization of its performances. To that end, NiCoCrAlYTa coatings were prepared using this new HVOAF technique. Investigations were

conducted to determine the effect of different compressed air flow rates on the evolution of the microstructure and properties of the resulting NiCoCrAlYTa coatings. The following conclusions can be drawn based on the current results.

1. A prototype of such an ethanol-fueled HVOAF spraying device has been successfully devised and constructed in the laboratory, enabling the addition of a large range of air flows downstream of the primary combustion chamber.
2. This device has been applied to fabricating NiCoCrAlYTa coatings on stainless steel substrates using variable flows of additional air.
3. Changing the flow rate of additional air has virtually no effect on the phase composition of the coatings but has, in contrast, substantial effects on their microstructures and properties, in terms of hardness, bonding strength, and sliding wear resistance.
4. The addition of compressed air tends to diminish the coatings bonding strength, which keeps however at satisfactorily elevated values.
5. The injection of compressed air contributes to increase the hardness of the coating and dramatically improves the coatings sliding wear resistance.
6. Adding compressed air also seems to reduce the degree of oxidation of the coatings, which helps improve their corrosion resistances.
7. The coupling of abrasive and adhesive wear is the primary wear mechanism, as it is common for NiCoCrAlYTa coatings.

References

[1] G. El-Awadi, S. Abdel-Samad, E.S. Elshazly, Hot corrosion behavior of Ni based Inconel 617 and Inconel 738 superalloys, Applied surface science 378 (2016) 224-230.

[2] X. Peng, S. Jiang, J. Gong, X. Sun, C. Sun, Preparation and hot corrosion behavior of a NiCrAlY+ AlNiY composite coating, Journal of Materials Science & Technology 32(6) (2016) 587-592.

[3] Y. Han, B. Zhang, X. Gu, X. Qiang, Y. Chu, X. Li, HRTEM and nanoindentation analysis of NiCoCrAlHfYSi and NiCoCrAlTaY coatings produced by AC-HVAF and APS, Surface and Coatings Technology 368 (2019) 202-214.

[4] L. Yang, Z. Zou, Z. Kou, Y. Chen, G. Zhao, X. Zhao, F. Guo, P. Xiao, High temperature stress and its influence on surface rumpling in NiCoCrAlY bond coat, Acta Materialia 139 (2017) 122-137.

[5] M. Ansari, R. Shoja-Razavi, M. Barekat, H.C. Man, High-temperature oxidation behavior of laser-aided additively manufactured NiCrAlY coating, Corrosion Science 118 (2017) 168-177.

[6] J. Pereira, J. Zambrano, C.R.M. Afonso, V. Amigó, Microstructure and mechanical properties of NiCoCrAlYTa alloy processed by press and sintering route, Materials Characterization 101 (2015) 159-165.

[7] Y. Ma, A. Ardell, Coarsening of γ (Ni–Al solid solution) precipitates in a γ′(Ni3Al) matrix; a striking contrast in behavior from normal γ/γ′ alloys, Scripta materialia 52(12) (2005) 1335-1340.

[8] S. Zhu, J. Cheng, Z. Qiao, Y. Tian, J. Yang, High temperature lubricating behavior of NiAl matrix composites with addition of CuO, Journal of Tribology 138(3) (2016) 031607.

[9] Y. Han, H. Chen, D. Gao, G. Yang, B. Liu, Y. Chu, J. Fan, Y. Gao, Microstructural evolution of NiCoCrAlHfYSi and NiCoCrAlTaY coatings deposited by AC-HVAF and APS, Journal of Thermal Spray Technology 26(8) (2017) 1758-1775.

[10] E. Hao, Y. An, X. Zhao, H. Zhou, J. Chen, NiCoCrAlYTa coatings on nickel-base superalloy substrate: Deposition by high velocity oxy-fuel spraying as well as investigation of mechanical properties and wear resistance in relation to heat-treatment duration, Applied Surface Science 462 (2018) 194-206.

[11] E. Hao, X. Liu, Y. An, H. Zhou, F. Yan, The coupling effect of immersion corrosion and cavitation

erosion of NiCoCrAlYTa coatings in artificial seawater, Corrosion Science 169 (2020) 108635.

[12] W. Deng, S. Li, G. Hou, X. Liu, X. Zhao, Y. An, H. Zhou, J. Chen, Comparative study on wear behavior of plasma sprayed Al2O3 coatings sliding against different counterparts, Ceramics International 43(9) (2017) 6976-6986.

[13] E. Hao, X. Zhao, Y. An, W. Deng, H. Zhou, J. Chen, The effect of pre-oxidation on microstructure, mechanical properties and high-temperature tribological behaviors of HVOF-sprayed NiCoCrAlYTa coating, Applied Surface Science 489 (2019) 187-197.

Chapter 6 Conclusions and Perspectives

6.1 Conclusions

The study carried out during this thesis has been dedicated to the "eGun", a recently developed ethanol fueled HVOF device and to a conversion of the same into an HVOAF prototype. Two powders, consisting in WC-10Co4Cr and Cr_3C_2–NiCr, were sprayed using at first the eGun HVOF version of the device, in order to investigate the performances of this new spraying technology. Furthermore, an eGun HVOAF version was created in the laboratory with the aim of enabling the introduction of additional air downstream of the combustion chamber, whereby modifying the in-flight characteristics of the particles, namely their residence time, speed and temperature. The effects induced by this modification were extensively evaluated by testing the performances of a number of NiCoCrAlYTa coatings prepared with this HVOAF version.

The results of the work have been set out in three parts.

The first part reports the performances of WC-10Co4Cr coatings deposited on a 304 stainless steel substrate via the eGun HVOF torch. We have investigated the effect of the oxygen/fuel ratio on the velocity and temperature of the in-flight particles, as well as the properties of the resulting coatings. Compared to "conventional" kerosene-oxygen and hydrogen-oxygen flames, the ethanol-oxygen flames lead to lower particle temperatures. The ethanol flow rate has a higher impact on the velocity and temperature of the particles than the oxygen one. The oxygen/ethanol ratio affects the characteristics of the flame. Oxygen in excess tends to cool the flame and decrease the particle temperature. Increasing the total gas flow raises the velocity of the in-flight particles, reducing their residence time in the flame as well as their temperature. Our results show that (i) the level of porosity of the coating gets reduced when the particle temperature and velocity increase, (ii) the microhardness increases with the particle temperature and (iii) the fracture toughness changes - to some extent - in the reverse sense of the porosity. To minimize porosity and maximize both microhardness and fracture toughness of WC-10Co4Cr coatings, the optimum set of flame conditions is made by a C_2H_6O flow rate of 22 slph and an O_2 flow rate of 520 slpm, leading to a molar oxygen/fuel ratio of

approximately 1.22.

In the second part of our work, Cr_3C_2–NiCr coatings were deposited on 304 stainless steel substrates using also the eGun HVOF torch. The main constituent phases of the coatings are NiCr and Cr_3C_2, while small amounts of Cr_7C_3 and Cr_2O_3 are also detected. The Taguchi method was used to optimize the process parameters for obtaining the lowest erosion wear loss. The optimal set of spray parameters proved to be 28 slph of ethanol, 420 slpm of oxygen, 76.7 g/min for the powder feed rate and 300 mm for the standoff distance. The ranking of the importance of the spray parameters is as follows: ethanol flow rate > oxygen flow rate > standoff distance > powder feed rate. An ANOVA analysis enabled confirming that the ethanol flow rate has the greatest impact on the erosion wear resistance of the coatings with a contribution of about 50 %, followed by the oxygen flow rate (37 %). The coatings deposited under these optimal conditions have an average hardness of 1048 HV0.3 and a porosity of about 1.5 %. These coatings display levels of porosity, fracture toughness, and bonding strength comparable to those prepared via conventional HVOF systems such as DJH2700, JP5000, and K2. However, interestingly, the microhardness proves much better. The erosion wear of the "optimized coating" was tested at 30°, 60° and 90° impact angles. It turned out that the erosion rate rises with the impact angle. The erosion mechanism involves processes of micro-cutting and ploughing of the matrix and the carbide grains, as well as the cracking of the carbides and some fatigue fracture spalling along the long-distance propagation of the matrix/carbide interface. Testing was also conducted to determine the effect of the combustion stoichiometry on the microstructures of the coatings, in correlation with their functional properties. The results reveal that the stoichiometric factor has little effect on the phase composition of the Cr_3C_2–NiCr coatings but have a great impact on their microstructure and properties in terms of porosity, microhardness, fracture, erosion resistance and sliding wear resistance. Cr_3C_2–NiCr coatings with better mechanical properties are obtained with values of the stoichiometric factor lower than 1 (at about 0.78). Note worthily, as far as kerosene-fueled HVOF devices are concerned, the stoichiometric factor of is generally set slightly below 1 to obtain good quality Cr_3C_2–NiCr coatings. The best performances in terms of sliding wear resistance of the Cr_3C_2–

NiCr coatings were also achieved with a stoichiometric factor lower than 1. The sliding wear mechanism involves the conjunction of abrasive grooving, peelings induced by cracking, fragmentation, and pull-out of carbide grains, as well as delamination and tribo-oxidation.

Finally, In the third part of the thesis, the eGun HVOF system has been converted to an eGun HVOAF one. To that end, it was decided to add a second chamber to the eGun torch in order to be able to inject compressed air into the stream of the in-flight particles. Such an ethanol fueled HVOAF prototype was successfully developed and applied to depositing NiCoCrAlYTa coatings on stainless steel substrates. Investigations were carried out to determine the effect of different compressed air flow rates on the evolution of the microstructures and properties of the resulting NiCoCrAlYTa coatings. The results show a substantial effect of this parameter on their microstructures and functional properties, in terms of hardness, bonding strength, and sliding wear resistance, while little effect on the phase composition of the coating was observed. Although the addition of compressed air diminishes the coatings bond ing strength, this property nevertheless stays at a fairly elevated level. The injection of compressed air contributes to increase the hardness of the coating and dramatically improves its resistance to sliding wear. The coupling of abrasive and adhesive wear is the primary wear mechanism of the HVOAF-sprayed NiCoCrAlYTa coatings. Besides, adding compressed air helps reduce the degree of oxidation of the coating which occurs during the spraying process, whereby slightly improving the corrosion resistance of the coating.

Overall, the conversion to an ethanol fueled HVOAF device brings more operational flexibility, as it enables a customization of the coatings by generating different properties, through a proper control of the flow rate of compressed air.

6.2 Perspectives

In view of further developments of the ethanol fueled HVOF and HVOAF systems, it would be valuable to undertake some additional works in the following directions:

1. While the erosion and sliding wear properties of HVOF-sprayed WC10Co4Cr and Cr_3C_2-NiCr coatings were the primary focus of the present research, their corrosion and

abrasive wear performances, and other properties can be studied to better characterize the full application potential of these coatings.

2. While our working scope has been limited to WC10Co4Cr and Cr_3C_2-NiCr coatings, it would also be interesting to use the ethanol fueled HVOF device to prepare and investigate other types of coatings as an enlargement of the capabilities of this new fabrication route. For example, one could investigate metal coatings such as NiCrBSi, stellite, 316, etc., as well as other cermet or polymer-based coatings.

3. A valuable benefit of ethanol as a fuel mainly resides in the lower environmental impact of its combustion as compared to fossil fuels, provided however it has a biogenic origin. It can also be blended with water, providing a quite simple way to lower the temperature and increase the flame speed, although to a less extent than does the injection of compressed air. This immediate advantage of ethanol fuel torches can also be beneficially studied and exploited.

4. The eGun HVOAF system can also be subject to further improvements. For instance, the geometry of the second-stage combustion chamber of the torch could be optimized to allow more compressed air to be added, thereby increasing still particle velocity, and reducing particle temperature more significantly. The geometry of the torch nozzle can also be revisited to increase particle velocity.

5. Regarding the NiCoCrAlYTa coatings sprayed via ethanol based HVOAF devices, the corrosion performance can be further studied by e.g. exploring the effect of still higher compressed air flows on their performance and by investigating the prevailing corrosion mechanisms. Similar developments can be devoted to their resistance to high-temperature oxidation while taking as reference the performance obtained with the HVOF counterpart.

6. The particle velocity and temperature measurement using eGun HVOAF system is not easy, especially the measurement of particle temperature under different air flow rates. This issue should be revisited to help understand the control window of the eGun HVOAF process. Then combined with the control window of the novel HVOAF process, other suitable materials and potential applications can be further explored.

Abstract

The high velocity oxy-fuel (HVOF) spray has become a process of choice for producing high performance cermet or alloy coatings. Common HVOF thermal spray systems classically use the combustion of gases, such as hydrogen, propane or a liquid fuel such as kerosene. However, there is currently a limited amount of literature on the use of ethanol as a fuel within HVOF processes and the performances of the resulting coatings are not well documented. Ethanol benefits from environmentally friendly features and is less polluting compared to conventional fossil liquid fuels (i.e. kerosene) as its combustion generates less nitrogen oxides and soot particles. In this work, we decide to investigate such an ethanol-fueled HVOF device (called "eGun HVOF"), with the aim to define the merits and limitations of that technology. In view of the limited literature available, it appeared to be of great interest to study the optimization of the spraying parameters of that new spraying process and thoroughly evaluate the performances of the corresponding coatings. In addition, as a specific development brought to this technology, we managed some design modifications of the eGun device in view of improving the quality of the coatings.

At first, commercial WC-10Co-4Cr powder was sprayed using the eGun HVOF process. Investigations were carried out to determine the influence of different oxygen/fuel ratios on the evolution of the velocity and temperature of in-flight particles in correlation with the properties of the resulting coatings. The variation of the ethanol flow rate appeared to have a greater influence on the velocity and temperature of the particles than that of oxygen. We elaborate detailed correlations between particle parameters and coating properties to deduce spray parameters providing the best performing coatings.

Next, we used the eGun to prepare Cr_3C_2–25wt.%NiCr coatings on a 304 stainless steel substrate. The Taguchi method was employed to adjust the spray parameters providing the best erosion resistance at 90° impact angle. We obtained then the optimal spray parameters (OSP) for minimum erosion wear. We also compared the performances of various Cr_3C_2-25wt.%NiCr

coatings prepared by different HVOF processes. This showed that the porosity, fracture toughness, and bonding strength of the coatings prepared with the new eGun HVOF are comparable to those obtained with the conventional HVOF devices (DJH2700, JP5000, K2). Interestingly, the microhardness proved much better. The erosion wear testing of the "optimized coating" was conducted at 30°, 60° and 90° impact angle. It turned out that the erosion rate rises with the increase of the impact angle. The erosion mechanism involves micro-cutting and ploughing of the matrix and the carbide grains, as well as cracking of the carbides and fatigue fracture spalling caused by long-distance propagation of cracks along the matrix/carbide interface. In addition, we performed investigations to determine the influence of different stoichiometric conditions, defined as the oxygen/ethanol ratio, on the coating microstructure and in relation with the resulting coating properties. The results show that the Cr_3C_2–NiCr coatings are denser and of better quality (higher hardness, lower porosity, higher fracture toughness and higher erosion resistance) when the stoichiometry factor is lower than 1 (with an optimum at about 0.78).

In the last part of the thesis, we conducted some developments intended to further improve the capabilities of the eGun, which we used this time as an HVOAF system (i.e. with air added as a milder oxidizer). To be able to feed the eGun torch with compressed air, it was decided to design and install a second-stage combustion chamber. NiCoCrAlYTa coatings were prepared using this modified, ethanol-fueled HVOAF device. Investigations were conducted to determine the influence of different flow rates of compressed air on the microstructures and the properties of the resulting NiCoCrAlYTa coatings. The results reveal that the addition of compressed air contributes to reduce the degree of oxidation of the coating and dramatically improves its resistance to sliding wear. We elaborated a detailed correlation between the compressed air flow rate and the coating properties to identify the conditions securing the best performing coatings.

Keywords: HVOF; ethanol; oxygen/fuel ratios; erosion resistance; HVOAF; NiCoCrAlYTa; oxidation; sliding wear resistance

Résumé

La projection oxy-combustible à grande vitesse (HVOF) est devenue un procédé de choix pour produire des revêtements de cermet ou dalliage à haute performance. Les systèmes de projection thermique HVOF courants utilisent classiquement la combustion de gaz, tels que lhydrog ène, le propane ou un combustible liquide tel que le kérosène. Cependant, il existe actuellement une quantité limitée de littérature sur lutilisation de léthanol comme carburant dans les procédés HVOF et les performances des revêtements résultants ne sont pas bien documentées. Léthanol bénéficie de caractéristiques respectueuses de lenvironnement et est moins polluant par rapport aux combustibles liquides fossiles conventionnels (cest -à-dire le kérosène) car sa combustion génère moins doxydes dazote et de particules de suie. Dans ce travail, nous décidons détudier un tel dispositif HVOF alimenté à léthanol (appelé "eGun HVOF"), dans le but de définir les mérites et les limites de cette technologie. Au vu de la littérature limitée disponible, il est apparu dun grand intérêt détudier loptimisation des paramètres de projection de ce nouveau procédé de projection et dévaluer en profondeur les performances des revêtements correspondants. De plus, en tant que développement spécifique apporté à cette technologie, nous avons géré certaines modifications de conception du dispositif eGun en vue daméliorer la qualité des revêtements.

Au début, la poudre commerciale de WC-10Co-4Cr a été projecté en utilisant le procédé eGun HVOF. Des investigations ont été menées pour déterminer linfluence de différents rapports oxygène/carburant sur lévolution de la vitesse et de la température des particules en vol en corrélation avec les propriétés des revêtements résultants. La variation du débit déthanol semble avoir une plus grande influence sur la vitesse et la température des particules que celle de loxygène. Nous élaborons des corrélations détaillées entre les paramètres des particules et les propriétés du revêtement pour en déduire les paramètres de projection fournissant les revêtements les plus performants.

Ensuite, nous avons utilisé leGun pour préparer des revêtements Cr_3C_2–25wt.% NiCr sur un substrat en acier inoxydable 304. La méthode Taguchi a été utilisée pour ajuster les

paramètres de projection offrant la meilleure résistance à lérosion à un angle dimpact de 90°. Nous avons alors obtenu les paramètres de projection optimaux (OSP) pour une usure par érosion minimale. Nous avons également comparé les performances de divers revêtements Cr_3C_2-25wt.%NiCr préparés par différents procédés HVOF. Cela a montré que la porosité, la ténacité à la rupture et la force de liaison des revêtements préparés avec le nouveau eGun HVOF sont comparables à celles obtenues avec les dispositifs HVOF conventionnels (DJH2700, JP5000, K2). Fait intéressant, la microdureté sest avérée bien meilleure. Les tests dusure par érosion du “ revêtement optimisé ” ont été effectués à des angles dimpact de 30 °, 60 ° et 90 °. Il sest avéré que le taux dérosion augmente avec laugmentatio n de langle dimpact. Le mécanisme dérosion implique la micro -découpe et le labour de la matrice et des grains de carbure, ainsi que la fissuration des carbures et lécaillage par rupture de fatigue provoqué par la propagation à longue distance des fissures le long de linterface matrice/carbure. De plus, nous avons effectué des recherches pour déterminer linfluence de différentes conditions stoechiométriques, définies comme le rapport oxygène/éthanol, sur la microstructure du revêtement et en relation avec les propriétés du revêtement résultant. Les résultats montrent que les revêtements Cr_3C_2-NiCr sont plus denses et de meilleure qualité (dureté plus élevée, porosité plus faible, ténacité à la rupture plus élevée et résistance à lérosion plus élevée) lorsque le facteur de stoechiométrie est inférieur à 1 (avec un optimum à environ 0,78).

Dans la dernière partie de la thèse, nous avons mené quelques développements destinés à améliorer encore les capacités de leGun, que nous avons utilisé cette fois comm e un système HVOAF (cest -à-dire avec de lair ajouté comme oxydant plus doux). Pour pouvoir alimenter la torche eGun en air comprimé, il a été décidé de concevoir et dinstaller une chambre de combustion de deuxième étage. Les revêtements NiCoCrAlYTa ont été préparés à laide de cet appareil HVOAF modifié alimenté à léthanol. Des investigations ont été menées pour déterminer linfluence de différents débits dair comprimé sur les microstructures et les propriétés des revêtements NiCoCrAlYTa résultants. Les résultats révèlent que lajout dair comprimé contribue à réduire le degré doxydation du revêtement et améliore considérablement

sa résistance à lusure par glissement. Nous avons élaboré une corrélation détaillée entre le débit dair comprimé et les pr opriétés du revêtement pour identifier les conditions garantissant les revêtements les plus performants.

Mots clés: HVOF; éthanol; rapports oxygène/carburant; résistance à lérosion; HVOAF; NiCoCrAlYTa; oxydation; résistance à lusure par glissement